

Low-mass X-ray binary studies with XMM–Newton

Dissertation

der Mathematisch-Naturwissenschaftlichen Fakultät
der Eberhard Karls Universität Tübingen
zur Erlangung des Grades eines
Doktors der Naturwissenschaften
(Dr. rer. nat.)

vorgelegt von
Benjamin Nicolas Mück
aus Tübingen

Tübingen
2014

Tag der mündlichen Qualifikation:

24.07.2014

Dekan:

Prof. Dr. Wolfgang Rosenstiel

1. Berichterstatter:

Prof. Dr. Andrea Santangelo

2. Berichterstatter:

Prof. Dr. Klaus Werner

ABSTRACT

The work presented in this thesis addresses both observational and instrumentation aspects to the study of low-mass X-ray binaries.

The analysis of the low-mass X-ray binary system 4U 1735–44, observed by the X-ray satellites *BeppoSAX* and *XMM-Newton*, is discussed. For the first time, the broad-band spectrum of the source was investigated which could be modeled by an absorbed combination of a disk blackbody and Comptonization components. The primary focus of the study is set on the fluorescence iron K_α line spectral feature. This line is an important issue since, in the community, it is still debated whether such an iron line can be affected by the relativistic effects which occurs close to a compact object. These effects would result in a broad and asymmetric shape of the line. However, there are also discussions that the shape of the line can be distorted by the occurrence of pile-up and only seems to be relativistic. In this work it is shown that for 4U 1735–44, the line can be modeled either with a broad Gaussian line or with a relativistic line for which the production site is not close to the neutron star. However, even if pile-up effects are carefully taken into account, no distortion of the line due to pile-up was found. The results obtained by the fit of the broad-band spectrum and the detailed study of the iron line led to the suggestion of a possible geometry of the source, which is a combination of the competitive Western and Eastern models.

The second part of the thesis is explicitly focussed on the systematic effects caused by pile-up and their impact on the iron K_α line. Especially, the Timing Mode of the EPIC-PN camera aboard *XMM-Newton* was investigated, since the results obtained by this instrument were doubted by Ng et al. (2010). Therefore, a variety of simulations were performed using the SIXTE simulation package. It was found, as expected, that pile-up hardens the spectrum of a low-mass X-ray binary. However, no distortion of the iron line due to pile-up was found. Moreover, it is shown in this thesis that relativistic lines reported in literature are robust against pile-up and that their relativistic origin can be proven.

Finally, the problem of background extraction for the Timing Mode of the EPIC-PN is discussed. In this readout mode no region on the CCD can be defined

from which an uncontaminated background spectrum can be extracted. It is shown that the use of blank field observations is a meaningful option to provide a template from which a suitable background spectrum can be extracted from for a given observation. This method will be a profitable task for further studies of especially weak and highly obscured sources observed in Timing Mode.

ZUSAMMENFASSUNG

In dieser Doktorarbeit werden verschiedene Aspekte beleuchtet, die eine wichtige Rolle bei der Untersuchung von Röntgenquellen und insbesondere von Röntgendoppelsternen spielen.

Zuerst wird die Analyse des Röntgendoppelsterns 4U 1735–44 präsentiert, wobei die Beobachtungen mit den Röntgensatelliten *BeppoSAX* und *XMM-Newton* durchgeführt wurden. Zum ersten Mal wurde für diese Quelle ein Breitbandspektrum untersucht, das mit Hilfe einer Kombination zweier Modelle charakterisiert werden kann. Diese Modelle beinhalten zu einem die Strahlung einer Akkretions-scheibe, die einem Schwarzkörper sehr ähnlich ist, sowie einer Komponente, die ihren Ursprung in Comptonisierung hat. Das Hauptaugenmerk wird hierbei auf die K_α Fluoreszenzlinie des Eisens gelegt. Es ist noch nicht abschließend geklärt ob eine solche Linie durch die relativistischen Effekte, die in der Nähe eines Neutronensterns auftreten, verbreitert sein kann oder nicht. Ein weiterer Diskussionspunkt ist, dass das Auftreten von Pile-up möglicherweise die Form der Linie verändert und sie somit nur den Anschein erweckt relativistisch verbreitert zu sein. In dieser Arbeit wird gezeigt, dass die Linie im Spektrum von 4U 1735–44 sowohl durch eine Gauss-Funktion als auch durch ein relativistisches Modell charakterisiert werden kann. Die Ergebnisse des relativistischen Modells deuten allerdings auf einen Entstehungsort der Linie hin, der nicht in der unmittelbaren Nähe des Neutronensterns liegt. Desweiteren wurde, unter Berücksichtigung von Pile-up, keine Veränderung der Linie beobachtet. Als eine mögliche Geometrie der Quelle wird eine Kombination aus dem *Western* und dem konkurrierenden *Eastern* Modell vorgeschlagen.

Der zweite Teil der Arbeit befasst sich mit einer tiefergehenden Untersuchung der Effekte, die durch Pile-up verursacht werden, sowie deren Einfluss auf die Eisen K_α -Linie. Insbesondere wurde der Timing Mode der EPIC-PN Kamera von *XMM-Newton* untersucht, da die auf diesem Instrument beruhenden Ergebnisse von Ng et al. (2010) angezweifelt wurden. Auf Grund dessen wurde eine Vielzahl von Simulationen mit Hilfe des SIXTE Simulationspakets durchgeführt. Die Simulationen zeigten, wie erwartet, dass Pile-up das Spektrum eines Röntgendoppelsterns härter und somit flacher macht. Allerdings konnte auch bei den Simulationen keine

Veränderung der Linie, die durch Pile-up verursacht wurde, beobachtet werden. Darüber hinaus wird in dieser Arbeit das Auftreten von relativistisch verbreiterten Linien, auch unter Berücksichtigung des Einflusses von Pile-up, bestätigt.

Der letzte Teil der Arbeit betrachtet das Problem des Hintergrundspektrums von EPIC-PN Beobachtungen, die im Timing Mode durchgeführt werden. In diesem Auslesemodus ist es nicht möglich einen Bereich zu definieren, der frei von jeglichen Quellphotonen ist und aus dem somit kein reines Hintergrundspektrum gewonnen werden kann. Es wird gezeigt, dass die Nutzung von *Blank Field* Beobachtungen eine vielversprechende Methode ist, um eine Vorlage zu erstellen, aus der man ein geeignetes Hintergrundspektrum für eine gegebene Beobachtung erhalten kann.

CONTENTS

Abstract	3
Zusammenfassung	5
1 X-ray Astronomy	15
1.1 Evolution of detection techniques	15
1.1.1 The first steps	15
1.1.2 Focusing optics	16
1.1.3 Detection Techniques	17
1.1.4 Outlook to Future Missions	20
1.2 <i>BeppoSAX</i>	21
1.2.1 LECS	22
1.2.2 MECS	22
1.2.3 HPGSPC	23
1.2.4 PDS	23
1.2.5 Background of NFIs	23
1.3 <i>XMM-Newton</i>	24
1.3.1 Optics	24
1.3.2 EPIC-MOS	24
1.3.3 EPIC-PN	24
1.4 Outline of the thesis	30
2 Sources of X-rays	31
2.1 Production of X-rays	31
2.1.1 Blackbody radiation	31
2.1.2 Compton scattering	33
2.1.3 Comptonization	35
2.1.4 Fluorescence	36
2.2 X-ray Binaries	37

2.2.1	Accretion	37
2.2.2	Formation	39
2.3	Properties of X-ray binaries	41
2.3.1	Spectral properties	41
2.3.2	Timing properties	44
3	Data analysis of 4U 1735–44	47
3.1	Introduction of the source 4U 1735–44	47
3.2	Details of the applied source models	48
3.2.1	Absorption	48
3.2.2	Blackbody	49
3.2.3	Comptonization	50
3.2.4	Reflection	50
3.2.5	Line	50
3.3	Analysis of <i>BeppoSAX</i> data	51
3.3.1	Data extraction and selection	51
3.3.2	Timing analysis	52
3.3.3	Spectral analysis	53
3.4	Analysis of <i>XMM-Newton</i> data	56
3.4.1	Data extraction and selection	56
3.4.2	Timing analysis	59
3.4.3	Spectral analysis	60
3.5	Discussion	62
4	Pile-up Simulations	65
4.1	Motivation	65
4.2	Simulation of pile-up for the EPIC-PN	67
4.2.1	The SIXTE simulation package	68
4.2.2	Simulation Inputs	71
4.3	Results of generic simulations	74
4.3.1	Continuum	77
4.3.2	Narrow Line - Sim 1	78
4.3.3	Normal Line - Sim 2	80
4.3.4	Broad Line - Sim 3	80
4.3.5	Relativistic Line - Sim 4	81
4.4	Results of specific observations	81
4.4.1	Serpens X-1	83
4.4.2	4U 1705–44	84
4.4.3	4U 1636–36	86
4.5	Conclusions	88

5	Background for Timing Mode	105
5.1	Motivation and Goal	105
5.2	Sources of background	107
5.2.1	Photons	107
5.2.2	Internal background	108
5.3	Blank Field Inspection	109
5.3.1	The Blank Field Observation Sample	109
5.3.2	Sample Characteristics	110
5.3.3	Background properties	113
5.3.4	Normalization of the blank field	118
5.4	Testing	118
5.4.1	Single Blank Field	119
5.4.2	Merged Blank Field Event List	121
5.4.3	Time-dependent Merged Blank Field Event List	121
5.4.4	Apply different background spectra	123
5.5	Conclusions and Outlook	123
6	Summary and Outlook	127
6.1	Summary and Conclusions	127
6.2	Outlook	128
	Bibliography	130
	Acknowledgements	137
	Curriculum vitae	139

LIST OF FIGURES

1.1	Absorption curve of electro-magnetic radiation in atmosphere	16
1.2	Schematic view of a Wolter Type-I telescope	17
1.3	Illustration of <i>EXOSAT</i> -GSPC	18
1.4	Illustration of a CCD	19
1.5	Illustration of <i>BeppoSAX</i>	22
1.6	Mirror module and PSF of the EPIC-PN telescope	25
1.7	Valid pattern types for EPIC-PN	26
1.8	Operating modes of the EPIC-PN	28
1.9	Setup of the EPIC-PN Timing Mode	29
2.1	Blackbody spectra for different temperatures	32
2.2	Compton scattering	33
2.3	Comptonized spectrum	35
2.4	Transitions in Iron	36
2.5	Roche-lobe overflow	38
2.6	Illustration of a relativistic line profile	42
2.7	Illustration of the Western and Eastern model	43
2.8	Geometry of a low mass X-ray binary	44
2.9	Color-color diagrams of an <i>atoll</i> and a <i>Z-source</i>	46
3.1	<i>BeppoSAX</i> and <i>RXTE</i> ASM light curves of 4U 1735–44	52
3.2	Color-color diagram of the <i>BeppoSAX</i> observations	53
3.3	<i>BeppoSAX</i> spectra and residuals of the continuum fit	54
3.4	<i>BeppoSAX</i> unfolded spectra and residuals	55
3.5	<i>BeppoSAX</i> spectra from different parts of the color-color diagram	57
3.6	<i>XMM-Newton</i> epatplots of different extraction regions	58
3.7	<i>XMM-Newton</i> and <i>RXTE</i> ASM light curves of 4U 1735–44	59
3.8	<i>XMM-Newton</i> color-color diagram	60
3.9	EPIC-PN spectra of different extraction regions	62
3.10	Possible geometry of 4U 1735–44	63

4.1	Illustration of pile-up in a CCD	66
4.2	Illustration of the simulation setup	68
4.3	PSFs at different energies and PI over RawX plot	71
4.4	EPATPLOT of the charge cloud adjustment	72
4.5	Residuals of a continuum simulation	75
4.6	Epatplot for continuum simulation	76
4.7	Residuals of simulations with a narrow and a normal Gaussian line	79
4.8	Residuals of simulations with a broad Gaussian and a relativistic line	82
4.9	Cackett epatplot and fixed spectra	83
4.10	Line profiles depending on model	85
4.11	di Salvo epatplot and fixed spectra	86
4.12	Pandel epatplot and fixed spectra	87
5.1	Images and <i>RawX</i> profile of EPIC-PN observations	106
5.2	Cosmic diffuse X-ray emission and internal background	108
5.3	Blank fields in galactic coordinates	111
5.4	Plot of the PI energy over the raw X coordinate	112
5.5	MOS images and PN spectrum with simulated spectrum	114
5.6	Hardness ratio over galactic coordinates	115
5.7	Hardness ratio over time and RGS background	116
5.8	RGS background count rate dependent spectra	116
5.9	Hardness ration over count rates in high energy bands	117
5.10	Test observation T3 with different BFs and normalizations	119
5.11	Test observation T7 with different BFs and normalizations	120
5.12	Test observations with BF spectra from the merged event list	122
5.13	Test observation fits with different background spectra	124

LIST OF TABLES

1.1	EPIC-PN read-out modes	27
3.1	Summary of the analysed <i>BeppoSAX</i> observations	51
3.2	Best fit results for the four <i>BeppoSAX</i> observations	56
3.3	Best-fit results for the four <i>XMM-Newton</i> extraction regions	61
4.1	Input parameters for the charge cloud model.	73
4.2	Input model for the simulations.	74
4.3	Best-fit parameters of a continuum simulation	78
4.4	Best fit results for the Gaussian line model for different parameters	90
4.5	Best fit results for the DISKLINE line model for different parameters	91
4.6	Best fit results for the Gaussian line model for different parameters	92
4.7	Best fit results for the DISKLINE line model for different parameters	93
4.8	Best fit results for the Gaussian line model for different parameters	94
4.9	Best fit results for the DISKLINE line model for different parameters	95
4.10	Best-fit results for a relativistic line as input	96
4.11	Best-fit results for a relativistic line as input	97
4.12	Input and fit model values	98
4.13	Input and fit model values	99
4.14	Input and fit model values	100
4.15	Input and fit model values	101
4.16	Input and fit model values	102
4.17	Input and fit model values	103
5.1	Expected count ratios for different detector part combinations	110
5.2	Test sample information	118

CHAPTER 1

X-RAY ASTRONOMY

In the fifty years since the beginning of X-ray astronomy plenty of new astrophysical sources and phenomena were discovered by observing the sky in the energy range of 0.1 keV–100 keV. However, several new detection techniques and observing methods had to be developed to explore the Universe in X-rays. Because of the fact that X-rays from astronomical sources can only be detected from outside the atmosphere, space observatories carrying complex technologies are required for observations in X-rays, in contrast to observations in the optical waveband done from ground.

The working principles of the observation techniques used in the observatories, the main improvements, as well as the instruments used to obtain the results of this work, will be described in the following sections.

1.1 Evolution of detection techniques

1.1.1 The first steps

X-rays with an astrophysical origin are prevented from detection on Earth by atmospheric absorption. The same effect applies in the ultraviolet and infrared wavelengths, as well as in the γ -ray range (see Figure 1.1). Accordingly, direct observations in these energy bands are only possible in higher regions of the atmosphere or above it. Therefore, the pioneers of X-ray astronomy used rockets to reach these high altitudes. From early rocket missions only the Sun was known as an X-ray emitting astrophysical object when in 1962, Giacconi et al. (1962, 1964) detected the first extrasolar X-ray source, namely Scorpius X-1.

After it was shown that there are indeed detectable cosmic X-ray sources, a first satellite was developed which offered the possibility to perform systematic and specialised X-ray observations. The satellite was named *UHURU* (Jagoda et al. 1972) and was launched in 1970. A proportional counter of $\sim 840 \text{ cm}^2$, sensitive in an energy range of 2 keV–20 keV, was used to perform the observations. In its lifetime of more than two years, 339 X-ray sources were detected (Forman et al.

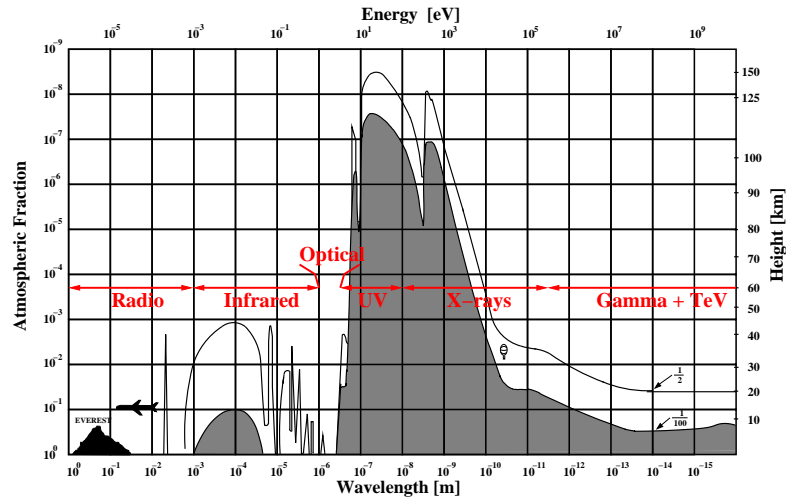


Figure 1.1: Absorption curve of electro-magnetic radiation in atmosphere. Illustration by T. Schanz (IAAT, Tübingen) based on Giacconi et al. (1968)

1978). Most of the sources were X-ray binaries, but supernova remnants, galaxies and clusters of galaxies were also found.

1.1.2 Focusing optics

The angular resolution of *UHURU* was limited to a value of $\sim 1^\circ$ due to the use of collimators. Consequently, a new method, namely focusing optics, was developed to reach higher angular resolution. The *Einstein* observatory (*HEAO-2*, Giacconi et al. 1979), launched in 1978 had focusing optics incorporated. The scientific instruments on board offered an angular resolution of the order of $1'$. This high resolution was provided by Wolter Type-I telescopes with an effective area of 30 cm^2 at 4 keV . The challenging point in the development of the telescopes was to decrease the focal length. X-rays are just reflected at small angles (for details see Aschenbach 1985). The angle is less than 1° for photon energies of $E_{ph} > 5 \text{ keV}$ and typical mirror materials like gold or iridium. A combination of a hyperbolic and a parabolic mirror part decreases the focal length to acceptable values (see Figure 1.2). Furthermore, the needed grazing incidence angle of the X-rays allows to nest several mirror shells in each other, which increases the effective area of the telescope.

The focusing optics of the *Einstein* observatory also offered, for the first time, the opportunity to perform high resolution observations with a grating spectrometer. Altogether, *Einstein* was the first mission which was capable of imaging extended objects, to resolve X-ray sources in neighbouring galaxies and detect fainter sources than any previous mission (e.g. catalogue by Fabbiano et al. 1992).

In the following years, several new missions were equipped with focusing optics.

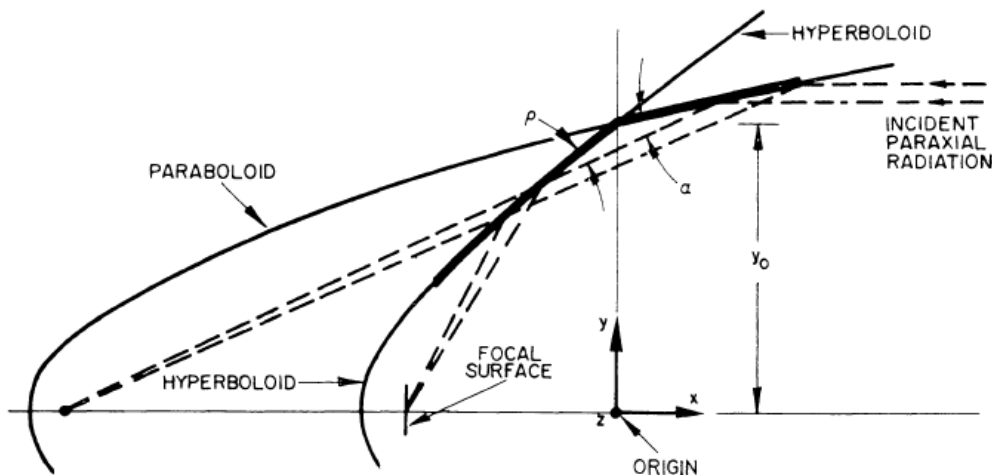


Figure 1.2: Schematic view of a Wolter Type-I telescope. To decrease the focal length a combination of a hyperbolic and parabolic mirror is used, Figure by Giacconi et al. (1969)

However, they were built to cover different aspects of X-ray astronomy. In 1983 the European Space Agency (ESA) launched its X-ray observatory called *EXOSAT* (White & Peacock 1988). For the first time Quasi Periodic Oscillations (QPOs, Elsner et al. 1986) and broad iron lines (White et al. 1986) were observed in Low Mass X-ray Binaries (LMXBs).

The intention of the ROentgen SATellite (*ROSAT*, Truemper 1982) launched in 1990, was to perform an all sky survey in the energy range of 0.1 keV–2.5 keV. More than 150 000 sources were detected in almost three years. Additionally, pointed observations were performed in the following six years. An overview of the history of X-ray astronomy is given by Santangelo & Madonia (2014).

Other missions like the still operating *Chandra* (Weisskopf et al. 2002) and *Suzaku* (Mitsuda et al. 2007) set their focus on a high spectral resolution. Two other missions with focusing optics, called *BeppoSAX* (Boella et al. 1997a) and *XMM-Newton* (Jansen et al. 2001), that have been used to obtain the data analysed in this thesis, will be described in more detail in forthcoming sections.

1.1.3 Detection Techniques

Hand in hand with the evolution of the optics, the used detectors were improved continuously. The combination of both allowed to make new discoveries.

Counters

In the early days of X-ray astronomy, mostly scintillation detectors and proportional counters were used (see for example Giacconi et al. 1968, for a review). Scin-

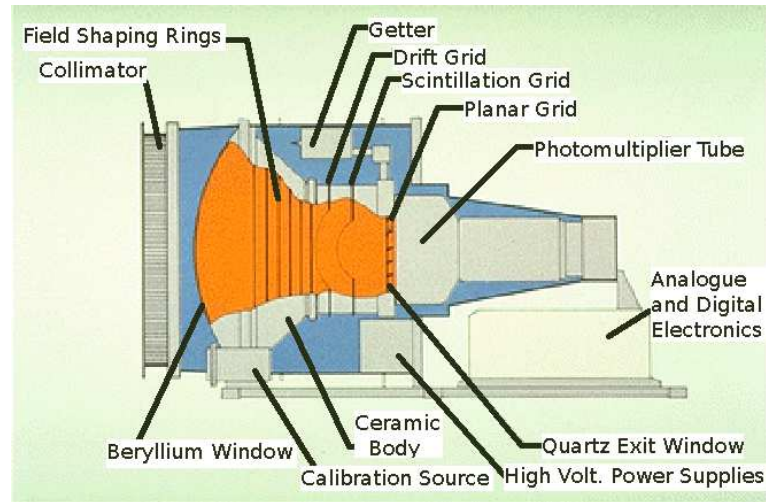


Figure 1.3: Illustration of the GSPC of *EXOSAT*. First the collimator in front of the beryllium entry window is shown which restricts the field of view. Afterwards in the scintillation region the photon creates electrons which excite the gas atoms. The photons emitted due to the deexciting of the atoms are measured in the photomultiplier tube. Furthermore, the electronics and power supplies are shown as well as the calibration source which delivers photons with a well-defined energy. Image, NASA HEASARC

tillation detectors are divided into two subgroups. At first, solid state detectors were used which were mostly built of NaI(Tl) or CsI(Na) crystals. The working principle is based on the fact that X-ray photons excite the electrons in the atomic shell to higher energy levels. Afterwards, when the electron relaxes again, a photon is emitted which can be measured. Such a solid state detector was used for example by Giacconi et al. (1962) in their rocket experiment. The same physical effect is used in Gas Scintillation Proportional Counters (GSPCs). They are filled with xenon or argon with admixed helium. Additionally, an electric field is applied. The incoming X-ray photons ionise the gas and the resulting photoelectrons create several other electrons. In the so-called drift region, the electrons follow the electric field to the scintillation region. Here the electrons excite the gas atoms and when deexciting photons are emitted, for most cases in the UV range. Finally the photons are measured by photomultipliers. As an example the GSPC (Peacock et al. 1981) used on board of *EXOSAT* is shown in Figure 1.3.

A similar working principle is used in proportional counters. Ionization takes place when a photon is absorbed in the gas. The emitted photoelectron is forced by an electric field to drift towards the anode. On its way it creates secondary electron-ion pairs. The final number of electrons is proportional to the energy of the original photon. An advanced version of a proportional counter was used, for example, in the Rossi X-ray Timing Explorer mission (*RXTE*, Jahoda et al. 1996).

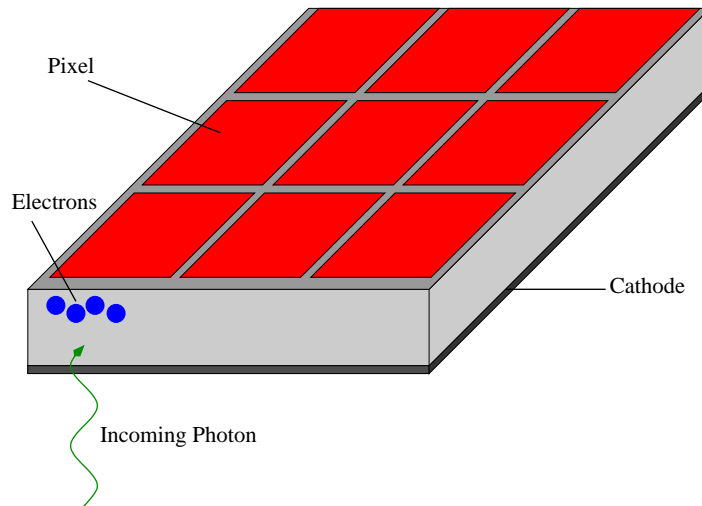


Figure 1.4: Shown is the basic principle of a CCD. The photon enters in this case from below and creates, depending on its energy, several free electrons. Due to the applied voltages the electrons are collected in a potential minimum in each pixel. Afterwards, well-defined pulses are applied to transfer the accumulated charge to the border of the CCD where the read-out electronics are placed.

Charge-coupled devices

A new kind of detectors, namely Charge-coupled devices (CCD), were first used in a Japanese mission called Advanced Satellite for Cosmology and Astronomy (*ASCA*, Tanaka et al. 1994). For the first time observations were performed with detectors based on semiconductors. An overview is given, for example, by Knoll (2000).

A semiconductor consists of silicon and is divided into two regions with different so-called dopings. Since silicon has four valence electrons, an element of the fifth element group, like phosphorous, creates an extra electron which cannot be bound. This creation of a free negative charge carrier is called n-doping. On the other hand, if an element of the third element group, like boron, is used, an electron is missing in the atomic bond, which is called a hole. Consequently, the material is called p-doped, since a positive charge carrier is created. Connecting both regions creates a depletion region in which free electrons and holes recombine and no free charge carriers remain. Due to that, current is only conducted in one way: If an external voltage is applied with the anode at the p-doped region and the cathode at the n-doped region, the depletion region decreases and a current flows. If the voltage is switched, the depletion region increases and no current can flow.

When applying a high voltage, the whole material becomes depleted. This effect is used in CCDs (a schematic view is given in Figure 1.4). If a photon enters this fully depleted region, it creates electrons via the photoelectric effect. To lift an electron from the valence band of silicon to the conduction band, an average energy of $\sim 3\text{eV}$ is necessary. Hence, a photon with an energy of 1keV

creates approximately 300 electrons. Due to the electric charge of the electrons and diffusion the resulting charge cloud widens while drifting through the detector to an applied potential minimum where the charge is accumulated. However, the widening can lead to a splitting of the accumulated charge over several pixels. Since detectors are tested intensely before launching, the expected pattern fractions are known to a certain degree and models can be established.

In addition to the electronics that provides the voltages which are necessary to deplete the material, control electrodes are mounted to create potential walls which subdivide the CCD into pixels. Also pulses can be applied by the electronics to transfer the charge to the border of the CCD where the read-out electronics are located. Altogether, the benefit of CCDs is a high signal-to-noise ratio which is achieved by a high number of free electrons leading to an energy resolution close to the statistical limit. Furthermore, a high quantum efficiency is achieved, as well as a small charge accumulation time and a simple way to read out the detector.

1.1.4 Outlook to Future Missions

The development of new observation methods and detection techniques is still in progress. Missions with different concepts are already under construction or in the first phase of the study. Three examples will be shortly described in the following.

eROSITA

The extended *RO*entgen Survey with an *Imaging Telescope Array*, *eROSITA* (Predehl et al. 2010), will be the next X-ray mission with European leadership which will start in March 2016. It is part of the Russian *Spektrum-RG* (Röntgen-Gamma) satellite.

Seven Wolter Type-I X-ray telescopes provide an effective area of 1365 cm^2 between 0.5 keV and 2 keV and 139 cm^2 in the energy range of 2 keV–10 keV which allows to perform a deep survey which is 20 times more sensitive as the *ROSAT* survey and will be able to detect more than 100 galaxy clusters with a redshift larger than one.

The so-called framestore CCDs allow to shift the complete accumulated image in a covered region from which it is read-out. Using this technique the out-of-time events are reduced which occurs if an event hits a pixel during the transfer and the read-out phase.

Athena

As the next large mission, *ATHENA* was chosen by the ESA to launch in 2028. *ATHENA* stands for *Advanced Telescope for High-Energy Astrophysics* and provide an effective area of about 2 m^2 by using a new kind of optics, namely silicon pore optics (Ferreira et al. 2012).

The instruments will be at the one hand the Wide Field Imager (WFI, Rau et al. 2013) which is working close to the theoretical limit of energy resolution and can be read-out in a short time which is achieved by active pixel sensors. Furthermore, the WFI allows to perform observations with a field of view of $40' \times 40'$. On the other hand there will be a cryogenic X-ray Integral Field Unit (X-IFU, Barret et al. 2013) which is a spectrometer with a high resolution of 2.5 eV and a field of view of $5' \times 5'$.

The scientific focus is set on large scale structures of the Universe and how they could have been formed as well as on black holes and their behaviour which is discussed in the mission White Paper by Nandra et al. (2013).

LOFT

LOFT (Bozzo et al. 2014), which stands for *Large Observatory For X-ray Timing*, will use another approach to provide, as the name indicates, a large effective area of about 10 m^2 . However, this cannot be achieved using focusing optics, but with the help of more than 2000 Silicon Drift Detectors which are placed on six separate panels that built the Large Area Detector (LAD). To restrict the field of view, collimators are placed on top of each detector which operates in an energy range of 2 keV–30 keV with an energy resolution of 260 eV. In addition, the Wide Field Monitor (WFM) is mounted on top of the satellite and encodes the sky by using a coded mask which is a well-defined pattern of transparent and opaque parts that allows to reconstruct an image of the sky.

Due to the increase of effective area of more than one order of magnitude, *LOFT* will be able to determine the mass-radius relation with a low uncertainty to put new constraints on the equation of state of neutron stars.

1.2 *BeppoSAX*

In this thesis data is analysed which was obtained by the Italian-Dutch satellite *SAX*, launched in 1996 from Cape Canaveral, Florida and operated until 2002. *SAX* stands for Satellite italiano per Astronomia X and was renamed after launch to *BeppoSAX* in honour of Giuseppe "Beppo" Occhialini who was involved in the discovery of the Pi-meson and contributed to the foundation of the European Space Agency (ESA). The mission was planned to cover a broad energy range of 0.1 keV–300 keV (Boella et al. 1997a) which was achieved by using four different kind of detectors shown in Figure 1.5. Although the focus was set on a broad energy coverage, the instruments provided good spectral capabilities at the energy of the iron K_α line ($\sim 6.4 \text{ keV}$) and at energies of cyclotron absorption features (above 20 keV). The low energy part up to 10 keV was covered by the Low Energy Concentrator Spectrometer (LECS, Parmar et al. 1997) and three units of the Medium Energy Concentrator Spectrometer (MECS, Boella et al. 1997b) which were placed at the focus of the X-ray telescopes (Conti et al. 1994). X-rays of energies above 10 keV

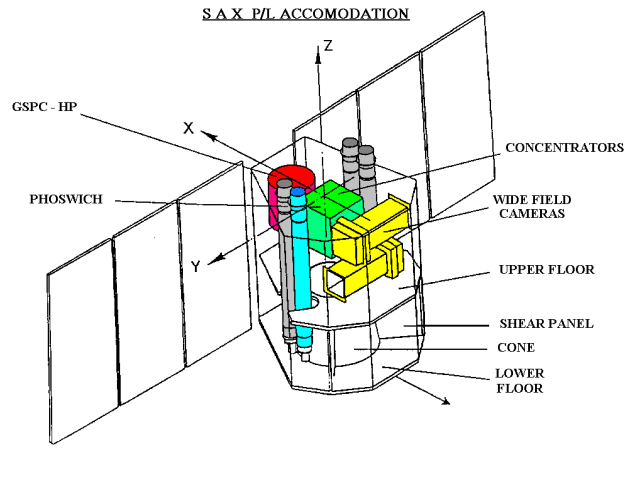


Figure 1.5: Illustration of *BeppoSAX*. Shown are the four Narrow Field Instruments as well as the Wide Field Cameras. Image, Boella et al. (1997a)

were able to be observed with the High Pressure Gas Scintillation Proportional Counter (HPGSPC, Giarrusso et al. 1995; Manzo et al. 1997) and the Phoswich Detection System (PDS, Frontera et al. 1995). Altogether, these four detectors were called the Narrow Field Instruments (NFIs) on board of *BeppoSAX*. Additional to that, two Wide Field Cameras (WFC, Jager et al. 1993) were mounted on the satellite which offered a sky coverage of $20^\circ \times 20^\circ$ simultaneously in an energy range of 2 keV–30 keV. In this work, only data obtained by the NFIs are discussed, and thus, the main features of these instruments are reported in the following.

1.2.1 LECS

The detection mechanism of the LECS followed the working principle of Gas Scintillation Proportional Counters. However, the counters were arranged to form pixels to achieve an imaging capability. The detector offered an effective area of 50 cm^2 at 6 keV, with an energy coverage from 0.1 keV–10 keV. Observations were able to be performed with a time resolution of $16 \mu\text{s}$ whereas the throughput was limited to 2000 events per second due to the dead time of the detector. Furthermore, an energy resolution of 8.8% FWHM at 6 keV allowed detailed spectral studies.

1.2.2 MECS

Similar to the LECS, the MECS units were made out of GSPCs. However, the effective area was 150 cm^2 at 6.4 keV, which was larger than that of the LECS. Furthermore, the energy resolution of 8% FWHM at 6 keV was also slightly better. The MECS only operated in an energy range of 1.3 keV–10 keV due to the used

filter. The MECS detectors also offered a maximum throughput of 2000 events per second.

1.2.3 HPGSPC

The HPGSPC was a cylindrical gas scintillation proportional counter that provided an effective area of 450 cm^2 which was sensitive in an energy range of 4 keV–120 keV with an energy resolution of 4% at 60 keV. The gas was a mixture of 90% xenon and 10% helium which was under a pressure of 5 atm. To limit the field of view to $1^\circ \times 1^\circ$ a collimator was mounted on top of the gas cell.

1.2.4 PDS

The PDS consisted of four units which were built out of NaI(Tl)/CsI(Na). It allowed observations to be performed in an energy range of 15 keV–300 keV with an effective area of 640 cm^2 . Since, similar to the HPGSPC, there were no focusing optics, a collimator was necessary to restrict the field of view, in the case of PDS to 1.3° . However, the energy resolution was limited to 14% at 60 keV.

1.2.5 Background of NFIs

To obtain proper results from the analysis of the performed observations, the background has to be taken into account. Several effects contribute to the background spectrum. At first, every detector exhibits specific internal features, like fluorescence lines which originate from surrounding materials. Furthermore, also electronic noise arises when the detector is read out and the obtained data is digitalized. Both effects are related to the detector and are not depending on the pointing of the telescope. On the other hand, the astrophysical background is changing from observation to observation which is created by diffuse X-ray emission and close-by sources that fall into the field of view of the detector. Finally, there is also particle background which consists mostly of protons that produce also a signal in the detector.

Therefore, different concepts of obtaining background spectra were developed. For the LECS as well as for the MECS the corresponding spectra are extracted from empty fields which are provided by the instrument teams. Another method has to be used for the HPGSPC and the PDS. The two instruments were rocking to off-source positions of $+3^\circ$ and -3° . Afterwards, the accumulated spectra from the off positions were subtracted from the on-source spectrum. However, the HPGSPC stopped rocking at the end of 2000 and a spectrum which is taken during the Earth occultation has to be used as background from this time on.

1.3 *XMM-Newton*

Three years after *BeppoSAX* another satellite was launched which should become one of the most successful ESA missions, namely *XMM-Newton*.

XMM stands for X-ray Multi-Mirror which emphasizes the fact that three X-ray telescopes simultaneously can be used to observe. The main part of this thesis is related to *XMM-Newton*, therefore, the optics and the instruments, in particular the European Photon Imaging Camera (EPIC) PN, will be described in the following.

1.3.1 Optics

The optics of *XMM-Newton* are discussed in Gondoin et al. (1998a), Gondoin et al. (1998b) and Jansen et al. (2001). The three X-ray telescopes on board of *XMM-Newton* consist of Wolter Type-I mirrors (see Section 1.1.2). To provide a high reflectivity, the nickel mirrors are coated with gold. Due to the grazing incidence technique, it is possible to nest 58 mirrors as shown on the left side of Figure 1.6. Accordingly, the size of the mirrors varies, namely between a diameter of 306 mm and 700 mm. Altogether, they provide a collecting area of 1500 cm² at 2 keV and 900 cm² at 7 keV. However, the nested mirrors have to be fixed with a spider wheel which creates shades that can be seen in the Point Spread Function (PSF, right side of Figure 1.6). The FWHM of the PSF was determined to be 6.6'' at 1.5 keV and 8 keV for mirror module 2. Furthermore, straylight from outside the field of view can contaminate observations. To prevent this, an X-ray baffle, which consists of a sieve plate, is mounted on top of each mirror module. Altogether, the optics has a focal length of 7.5 m.

1.3.2 EPIC-MOS

An EPIC-MOS (Metal Oxide Semi-conductor, Turner et al. 2001) camera is placed in the focal plane of two telescopes. Each MOS camera consists of seven front-illuminated CCDs whereas the imaging area is covered by 600×600 pixels. The 40 μm pixels, equivalent to 1.1'', cover an area of ~ 2.5 cm. To cover the whole focal plane with a diameter of 6.2 cm the seven CCDs are arranged to a mosaic, whereas the focal point lies in the middle of the central CCD. Observations can be performed in an energy range of 0.2 keV–10 keV with a spectral resolution of $E/\delta E \sim 20-50$. To deal with different kinds of sources, special read-out modes of the CCDs are provided. Since the MOS modes are similar to those of the other camera, the EPIC-PN, all modes will be described in the following EPIC-PN section.

1.3.3 EPIC-PN

As the name indicates, the EPIC-PN camera (Strüder et al. 2001) which is located in the focal plane of the third telescope (mirror module 2), consists of CCDs as

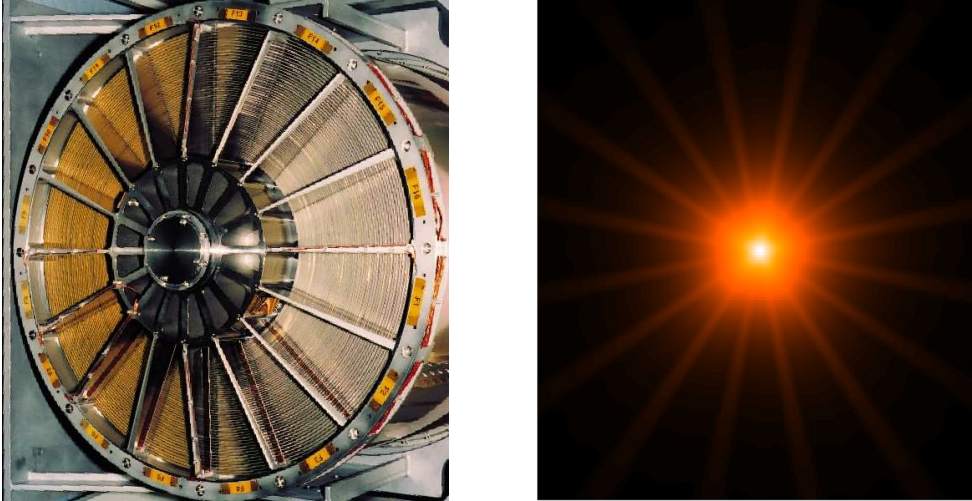


Figure 1.6: *Left hand:* The mirror module of *XMM-Newton* with the 58 nested mirrors which are fixed with the spider. *Right hand:* The PSF of the EPIC-PN telescope in which the spiders are also visible. Images, ESA.

described in Section 1.1.3 with a p-doping and a n-doping. The whole wafer is divided into twelve single CCDs each with 200×64 pixels with a size of $150 \times 150 \mu\text{m}$, which is equivalent to $4.1''$. The imaging area of $6 \times 6 \text{ cm}$ is covered by 400×384 pixels which is achieved by the superposition of the twelve CCDs. Due to the size of the pixels four types of events can occur, as it is shown in Figure 1.7. Any other pattern is marked as invalid because it cannot be the result of a single photon interaction. To avoid a gap between the single CCDs, the focal point is located close to the center of CCD0 in quadrant 1. Like the EPIC-MOS camera, the EPIC-PN is used by default in an energy range of $0.2 \text{ keV} - 10 \text{ keV}$, however, the EPIC-PN is also sensitive above 10 keV which allows to obtain reasonable results up to 15 keV .

As mentioned above, the EPIC cameras provide different read-out modes to deal with various count rates. The most important ones will be described in the following whereas for the EPIC-PN the temporal characteristics are given in Table 1.1 and an illustration is shown in Figure 1.8.

A complete following Chapter is addicted to the special problem of background extraction, hence, this problem will not be discussed here.

Full Frame Mode

When operating the camera in Full Frame Mode all pixels are active and are read out. The read-out is performed by so-called Normal Line shifts in which the charge of all pixels is shifted towards the CAMEX read-out chip and is read out (Kuster et al. 1999). Additional to the Normal Line shifts, which are per-

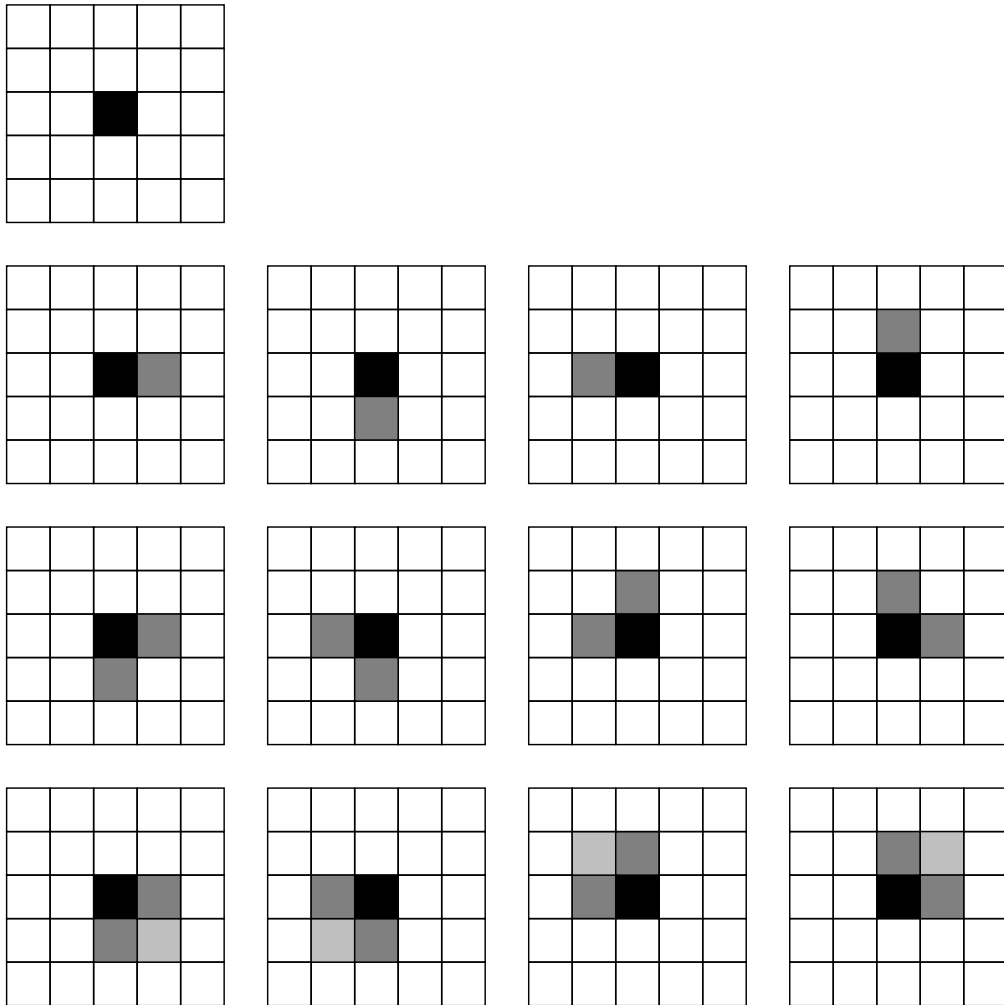


Figure 1.7: Shown are the valid patterns which can occur if the charge of an event splits over neighbouring pixels. The scheme is based on Dennerl et al. (1999). The intensity of the filling represents the amount of charge. The maximum charge in a triple pattern has to be in the corner, whereas in a quadruple the maximum and the minimum charge have to be in a diagonal line.

Table 1.1: Temporal characteristics of the different read-out modes of the EPIC-PN. The live time is defined as the ratio of the time in which scientific data can be collected and the frame time in which also the times for shifting and the read-out process are taken into account.

Mode	Time res. [ms]	Live time [%]	Max. count rate Point source [s ⁻¹]
Full Frame	73.4	99.9	2
Large Window	47.7	94.9	3
Small Window	5.7	71.0	25
Timing	0.03	99.5	<800
Burst	0.007	3.0	~ 60000

formed in 23.04 μ s, several other time lags are necessary between the read-out of the different CCDs and quadrants of the EPIC-PN. Altogether a time resolution of 73.4 ms results for the Full Frame Mode which can handle a count rate of 6 cts/s (0.7 mCrab¹ in the energy range of *XMM-Newton*) for point sources.

The MOS Full Frame Mode follows a similar working principle, however, the time resolution is 2.6 s which allows to deal with a maximal count rate of 0.7 cts/s (0.24 mCrab). A special mode for the EPIC-PN is the extended Full Frame Mode at which the integration time is increased and a time resolution of 199.1 ms (1 cts/s, 0.12 mCrab) is achieved.

Window Mode

The Window Mode can be sub-divided into Large Window and Small Window Mode. When the EPIC-PN is working in Large Window Mode, only data of the last 100 lines of each CCD are read out. Accordingly, the first 100 lines are fast shifted to the CAMEX and are not read out. Afterwards, the next 100 lines are read out like in the Full Frame Mode. Due to the limited imaging area, a time resolution of 47.7 ms can be reached, however, the maximal count rate is equal to the value of the Full Frame Mode. For the Small Window Mode, only one CCD is working. Consequently, the time resolution is increased to 5.7 ms and a count rate of 50 cts/s (6.5 mCrab) can be dealt with.

Both, the Large and Small Window Mode of the MOS cameras are restricted to the central CCD. The surrounding CCDs keep working in Full Frame Mode. In reading out just parts of the central CCD the time resolution is decreased to 0.9 s (1.8 cts/s, 0.6 mCrab) and 0.3 s (5 cts/s, 1.7 mCrab) for the Large and Small Window mode respectively.

¹A flux of 1 Crab is $\sim 3 \times 10^{-8} \text{ erg cm}^{-2} \text{ s}^{-1}$

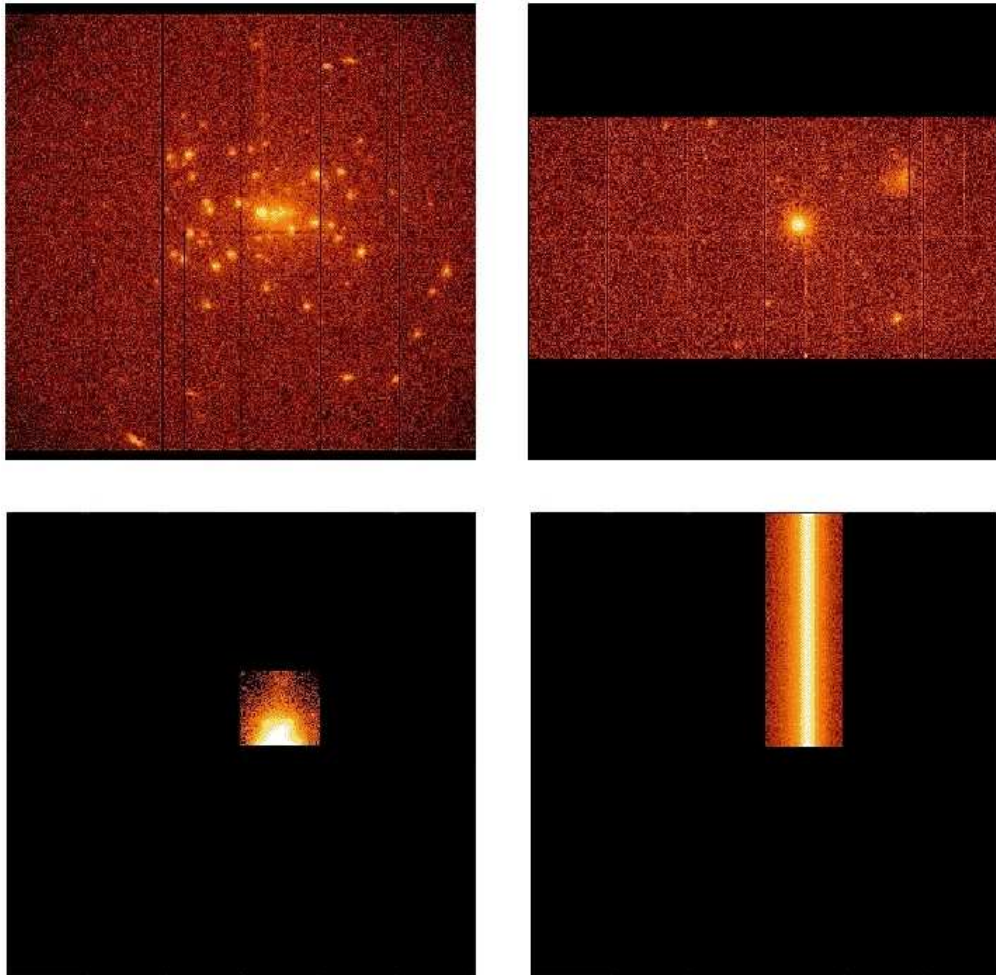


Figure 1.8: Operating modes of the EPIC-PN. Starting clockwise with the Full Frame mode, the Window Mode, the Timing Mode and the Burst Mode. Picture is taken from the *XMM-Newton* Users Handbook

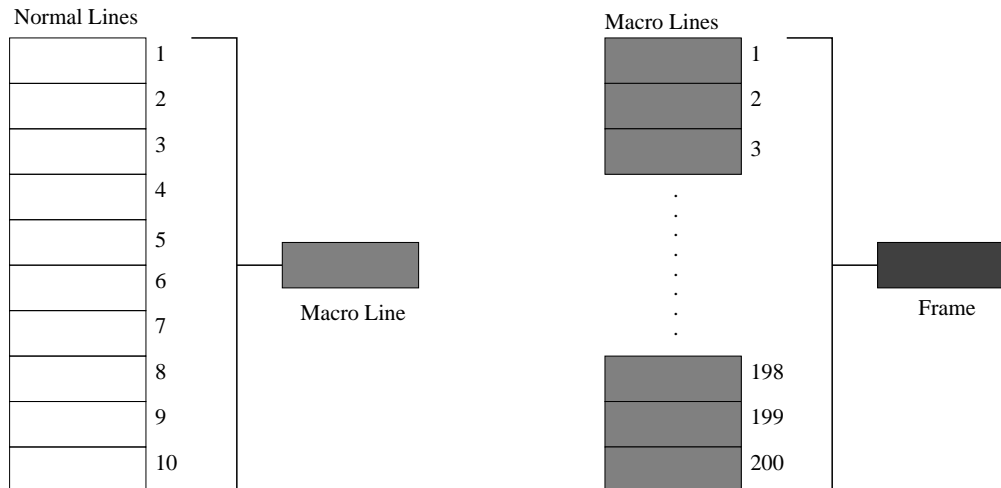


Figure 1.9: Shown is the setup of the EPIC-PN Timing Mode. The charge of ten normal lines are accumulated and then read-out as a macro line. A frame consists of 200 macro lines.

Timing Mode

The Full Frame Mode and the Window Modes are used for imaging. However, there are also modes which were developed to deal with high count rates. On the one hand, there is the Timing Mode in which usually only point sources are observed and therefore only one CCD, namely CCD 0 in quadrant 1, is used. A time resolution of $\sim 29.52 \mu\text{s}$ is achieved by shifting ten pixels via a fast Time Shift to the CAMEX. Doing this, the spatial resolution is limited to one dimension. The integrated charge of this ten pixels is seen as one macro pixel which is illustrated in Figure 1.9. Finally, the whole CCD is processed by reading out 20 macro pixels and one frame corresponds to ten times the complete CCD 0 or 200 macro lines. Due to the high time resolution, sources with count rates up to several hundred counts per second (tens of mCrab) can be dealt with. However, the exact count rate is not clear and under discussion in the community. In this work this problem will be studied and discussed in detail for the EPIC-PN.

The Timing Mode of the MOS cameras has the same mode of operation. However, it only offers a time resolution of 1.75 ms with a maximum count rate of 100 cts/s which is equivalent to 35 mCrab.

Burst Mode

A special mode of the EPIC-PN is the Burst Mode. In principle the read-out of this mode is similar to that of the Timing Mode. However, every read-out cycle starts with a Fast Shift of 200 lines. Since the source is placed close to line 190 and the fact that the core of the PSF covers a range from line 180–200, the following

180 lines were exposed to the source only during the Fast Shift. They are read out in the standard way. Consequently, the next 20 lines are not usable and are discarded. Although a time resolution of $7\ \mu\text{s}$ is achieved, which allows to handle a count rate of 60 000 cts/s, this mode is not used often since its livetime is 3%. This means that only in 3% of the exposure time, scientific usable data is accumulated.

There is no corresponding mode for the MOS cameras.

1.4 Outline of the thesis

In this Chapter, the improvements in X-ray astronomy were shown. Due to new developments and techniques new problems arise which have to be taken into account in the analysis of astrophysical observations.

However, it is not enough to understand the observation and detection methods, also the astrophysical processes which produce the observed photons have to be studied. Therefore, the basic production mechanisms and an overview of the sources of interest in this thesis, namely Low-mass X-ray binary systems, will be given in the next Chapter.

Subsequently, the thesis is divided into two parts. At first, the study of a low-mass X-ray binary system, namely 4U 1735–44, using observations performed with *BeppoSAX* and *XMM-Newton* will be presented in Chapter 3.

Furthermore, in the second part the focus is set onto observational problems of the EPIC-PN detector aboard *XMM-Newton*. The proper treatment of these issues is essential for a scientifically meaningful study. On the one hand, in Chapter 4 the problem of pile-up will be addressed which occurs at high source count rates and the influences of it on the spectral analysis will be investigated. On the other hand, the problem of a proper background extraction for the Timing Mode of the EPIC-PN will be studied in detail in Chapter 5.

Finally, the different parts of the thesis will be put together in the conclusions and an outlook for further studies will be given.

CHAPTER 2

SOURCES OF X-RAYS

The focus of this Chapter is set on the processes and mechanisms which are used to describe the emission properties of X-ray binaries which are the class of sources studied in this thesis. A sub-class of X-ray binaries, namely the Low-mass X-ray binary (LMXB) systems, will be described in more detail and two of the current theories developed to describe their behaviour will be presented.

2.1 Production of X-rays

X-rays cover an energy range from 0.1 keV up to some hundreds of keV, which corresponds to wavelengths from 10 nm to a few pm, respectively. Assuming thermal emission, such energies have to be produced in regions with temperatures above 1×10^6 K. However, there also mechanisms which take place in non-thermal regimes. Since both kind of mechanisms contribute to the spectral properties of LMXB systems, both will be discussed here. For details the reader is referred to Longair (2011).

2.1.1 Blackbody radiation

A perfect blackbody is an object in which electromagnetic radiation is in thermal equilibrium. Although a blackbody is just a theoretical object, it is often used to model the spectra of astrophysical sources in thermal equilibrium since in this state the assumption that the spectrum is determined only by the temperature and that the radiation is emitted isotropically is almost fulfilled. The corresponding intensity spectrum is described by the Planck function,

$$B_\nu = \frac{2h\nu^3}{c^2} \frac{1}{\exp(h\nu/kT) - 1}, \quad (2.1)$$

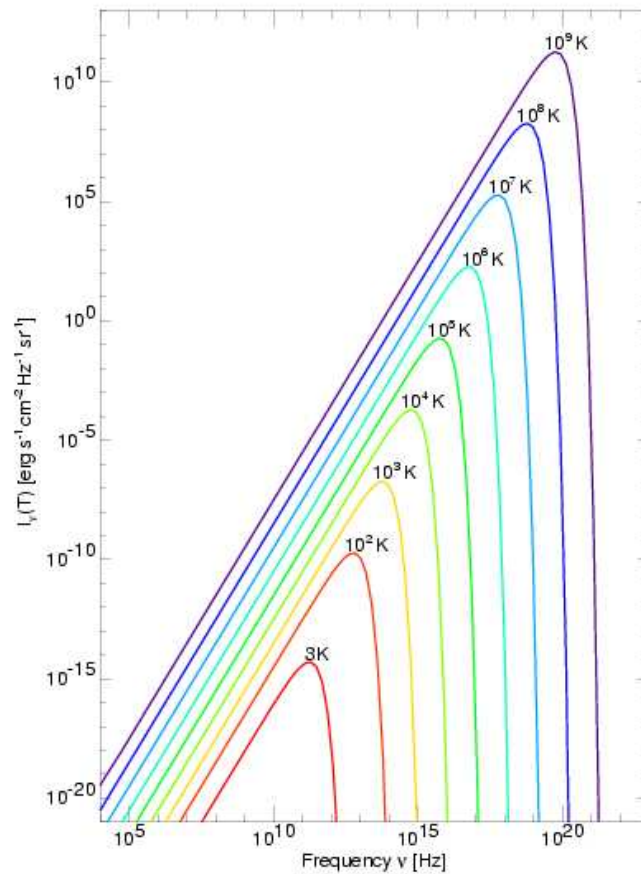


Figure 2.1: The spectrum of a blackbody only depends on its temperature. The intensity is shown on the y-axis and the frequency on the x-axis. Image, J. Wilms

where h is Planck's constant¹, k is Boltzmann's constant² and with T as the equilibrium temperature of the object. As it can be seen in Figure 2.1, spectra of higher temperatures fully enclose spectra of lower temperatures. Furthermore, the frequency of the maximum is shifted to higher values with increasing temperature, according to the Wien displacement law:

$$\nu_{\max} = 5.88 \cdot 10^{10} T K^{-1} \text{ Hz} \quad (2.2)$$

If several blackbody spectra of different temperatures are superposed, the resulting blackbody is called a *multicolor blackbody*.

¹ $h = 4.13566733(10) \cdot 10^{-15} \text{ eV s}$

² $k = 8.617343(15) \cdot 10^{-5} \text{ eV/K}$

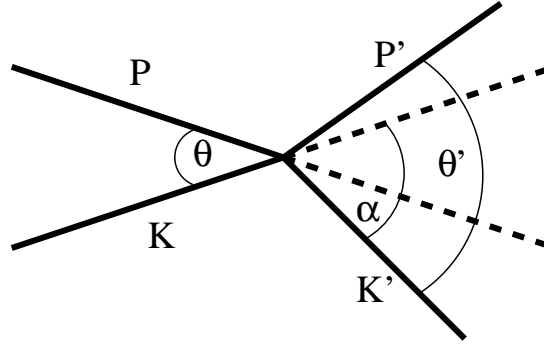


Figure 2.2: Schematic illustration of the Compton scattering. A photon with four-vector momentum \mathbf{P} interacts with an electron with the four-vector momentum \mathbf{K} under the angle θ . After the scattering the photon and the electron are described by \mathbf{P}' and \mathbf{K}' , respectively. The scattering angle α is defined as the angle between the incoming and outgoing electron.

2.1.2 Compton scattering

Compton scattering

Compton scattering is the generalization of Thomson scattering which describes the scattering of radiation on a stationary electron. Thomson scattering is valid if the energy of the photon $\hbar\omega$ is well below the rest mass of the electron $m_e c^2$. However, if $\hbar\omega \sim m_e c^2$, the frequency of the scattered radiation will change due to relativistic corrections and the Klein-Nishina cross section has to be used.

The effect of Compton scattering can be calculated by studying the geometry of the change of the momentum four-vectors of the photon \mathbf{P} and the electron \mathbf{K} . In Figure 2.2, Compton scattering is illustrated. Since the collision conserves momentum, it can be written as:

$$\mathbf{P} + \mathbf{K} = \mathbf{P}' + \mathbf{K}' \quad (2.3)$$

where

$$\mathbf{P} = [\gamma m_e c, \gamma m_e \vec{v}] \quad \text{and} \quad \mathbf{K} = \left[\frac{\hbar\omega}{c}, \frac{\hbar\omega}{c} \vec{i}_k \right] \quad (2.4)$$

are the momenta before the collision and

$$\mathbf{P}' = [\gamma m_e c, \gamma m_e \vec{v}'] \quad \text{and} \quad \mathbf{K}' = \left[\frac{\hbar\omega'}{c}, \frac{\hbar\omega'}{c} \vec{i}_{k'} \right] \quad (2.5)$$

are the momenta after the collision.

Further, the norms of the vectors are known to be

$$\mathbf{P} \cdot \mathbf{P} = \mathbf{P}' \cdot \mathbf{P}' = m_e^2 c^2 \quad \text{and} \quad \mathbf{K} \cdot \mathbf{K} = \mathbf{K}' \cdot \mathbf{K}' = 0. \quad (2.6)$$

Squaring 2.3, multiplying the result with \mathbf{K}' , and using 2.6 gives the four-vector equation:

$$\mathbf{P} \cdot \mathbf{K}' + \mathbf{K} \cdot \mathbf{K}' = \mathbf{P} \cdot \mathbf{K}. \quad (2.7)$$

Finally, inserting 2.4, using the scattering angle as $\vec{i}_k \cdot \vec{i}_{k'} = \cos \alpha$, $\cos \theta = \vec{i}_k \cdot \vec{v} / |\vec{v}|$ and $\cos \theta' = \vec{i}_{k'} \cdot \vec{v}' / |\vec{v}'|$ the resulting equation can be written as:

$$\frac{\omega'}{\omega} = \frac{1 - (v/c) \cos \theta}{1 - (v/c) \cos \theta' + (\hbar\omega/\gamma m_e c^2)(1 - \cos \alpha)}. \quad (2.8)$$

After the collision, the photon has a smaller frequency and therefore less energy. Part of the energy is transferred to the electron. In the special case of a stationary electron with $v = 0$ and $\gamma = 1$, the final frequency is:

$$\frac{\omega'}{\omega} = \frac{1}{1 + (\hbar\omega/m_e c^2)(1 - \cos \alpha)}. \quad (2.9)$$

Furthermore, the Thomson cross-section is only valid, if in the center of momentum frame $\hbar\omega \ll m_e c^2$ holds. Otherwise the Klein-Nishina cross-section must be used, which for low energy photons reduces to the Thomson cross-section:

$$\sigma_{\text{K-N}} = \frac{8\pi}{3} r_e^2 \left(1 - 2 \frac{\hbar\omega}{m_e c^2}\right) = \sigma_{\text{T}} \left(1 - 2 \frac{\hbar\omega}{m_e c^2}\right) \approx \sigma_{\text{T}} \quad (2.10)$$

Inverse Compton scattering

In Compton scattering the electron is usually assumed to be at rest. However, this is not always true. In many cases the electrons have some kinetic energy. In the case of a population of ultra-relativistic electrons interacting with a given photon field energy can be transferred to the photons which leads to an effective cooling of the electrons.

Assuming the energy of the photon to be much less than the rest mass energy of the electron ($\hbar\omega \ll m_e c^2$) allows the use of the Thomson scattering cross-section. To determine the energy loss the scattering is investigated in the laboratory frame S and in the rest frame of the electron S'. The key points of the calculation are to determine the photon energy in the rest frame of the electron and the rate of photons arriving at the electron. Following the calculations in Longair (2011) the photon energy is given by

$$\hbar\omega' = \gamma \hbar\omega [1 + (v/c) \cos \theta] \quad (2.11)$$

and the arrival rate of the photons can be determined with the help of

$$\frac{dE}{dt} = \frac{4}{3} \sigma_{\text{T}} c u_{\text{rad}} \left(\gamma^2 - \frac{1}{4} \right) \quad (2.12)$$

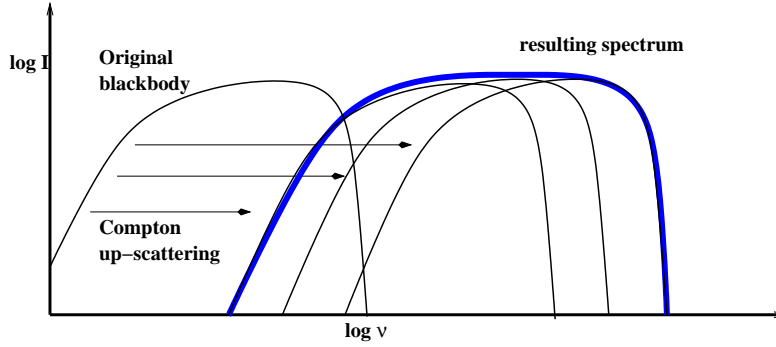


Figure 2.3: Schematic illustration of a Comptonized spectrum. A blackbody spectrum is Comptonized in a region of hot electrons. The resulting spectrum is a superposition of different up-scattered spectra. Illustration, Mück (2009)

where u_{rad} is the energy density of the radiation. Combining these equations, the average energy of the photons can be calculated as

$$\hbar\bar{\omega} = \frac{4}{3}\gamma^2 \left(\frac{v}{c}\right)^2 \hbar\omega_0 \approx \frac{4}{3}\gamma^2 \hbar\omega. \quad (2.13)$$

An example of the power of inverse Compton scattering can be given by looking at infrared photons that pass through a gas of electrons with Lorentz-factors of 1000. An infrared photon with a typical frequency of 3×10^{12} Hz produces X-rays of 3×10^{18} Hz, which is in the order of 10 keV.

2.1.3 Comptonization

If inverse Compton scattering is the dominant process and the contribution of other processes to the spectrum is negligible, the spectrum is said to be *Comptonized*. Comptonization mostly takes place in hot plasma which is not dense enough for other radiation processes to contribute to the spectrum. As before, the non-relativistic regime ($\hbar\omega \ll m_e c^2$) is investigated with the use of the Thomson cross-section. The average energy gain of the electron can be expressed by

$$\left\langle \frac{\Delta\epsilon}{\epsilon} \right\rangle = \frac{\hbar\omega}{m_e c^2}, \quad (2.14)$$

which was discussed in Section 2.1.2. Whereas, for the inverse Compton scattering process the average energy loss of the electrons can be determined by

$$\left\langle \frac{\Delta\epsilon}{\epsilon} \right\rangle = \frac{4kT_e}{m_e c^2}, \quad (2.15)$$

assuming a thermal distribution of the electron velocities of $\frac{1}{2}m_e \langle v^2 \rangle = \frac{3}{2}kT_e$.

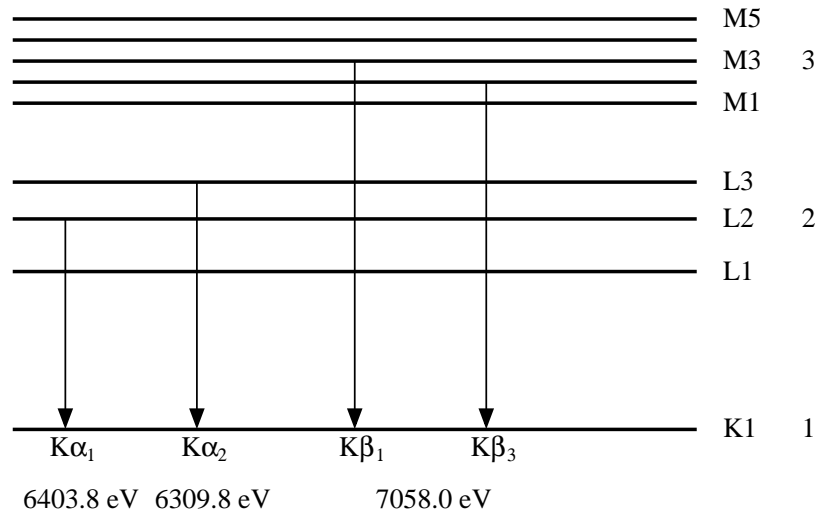


Figure 2.4: The most important transitions in astrophysics in the atomic shell of iron. The principal quantum numbers and the shell names are given on the right. The energy levels split due to the spin-orbit interaction in sub-levels. The Kβ₁ and Kβ₃ lines can not be resolved and therefore only one energy is reported. The transitions are named according to the X-ray data booklet (<http://xdb.lbl.gov/>)

Finally, this leads to the following equation of the average energy change per collision of the photon:

$$\left\langle \frac{\Delta\epsilon}{\epsilon} \right\rangle = \frac{4kT_e - \hbar\omega}{m_e c^2}. \quad (2.16)$$

This equation immediately shows, according to Longair (2011), three possibilities. If $4kT_e$ is equal to $\hbar\omega$, no net energy is transferred. Furthermore, if $\hbar\omega > 4kT_e$, Compton scattering takes place and for $4kT_e > \hbar\omega$, the photons gain energy on average by inverse Compton scattering.

However, the process of Compton scattering requires input photons which have to be provided by another mechanism. A possible mechanism is blackbody radiation which was discussed in Section 2.1.1. If a blackbody spectrum propagates through a population of hot electrons with different temperatures, the spectrum is shifted to higher energies, as shown in Figure 2.3.

2.1.4 Fluorescence

An important source of X-ray lines in astrophysics is due to fluorescence. This radiation occurs in several astrophysical sources when a plasma is irradiated on, for example, an accretion disc around a compact object. When an irradiating photon is absorbed by an atom, an electron is excited to higher energy levels or, if the energy is high enough, is ejected from the atom. However, if, for example, an electron in the lowest energy level, the K-shell, is lifted to a higher level, the

vacancy in the K-shell has to be filled again. This can be achieved by an electron of a higher level, as example the possible transitions in an iron atom are shown in Figure 2.4. In most cases an electron of the L- or M-shell fills the gap in the K-shell which results in a $K\alpha_1$ or $K\alpha_2$ fluorescence line for the L-shell and a $K\beta_1$ or $K\beta_3$ fluorescence line for the M-shell, respectively. Since it is not possible to resolve neither the $K\alpha_1$ and $K\alpha_2$ lines nor the $K\beta_1$ and $K\beta_3$ lines with the majority of detectors used in astronomy, only $K\alpha$ and $K\beta$ is used in the following.

The excessive, well-defined energy of the electron is carried away by emitting a photon. Therefore, a fluorescence line can be seen in the spectrum. The energy of the line depends on the ionization state of the atom. As an example, the energy of the $K\alpha$ line of iron can be 6.4 keV for no ionization and 6.97 keV if fully ionized.

2.2 X-ray Binaries

The radiation from astrophysical sources is produced by several different processes. In the following, the class of X-ray binaries will be discussed, for which an overview is given by Lewin & van der Klis (2006) and Longair (2011). To understand binary systems, the concept of accretion has to be understood first which is described in the next section. Subsequently, the formation processes are described which is followed by a description of the main spectral and timing properties of such systems.

2.2.1 Accretion

Accretion in general means the accumulation of matter. In particular in X-ray binary systems a compact object accretes matter from a companion star. When matter falls onto the surface of the accretor it loses its kinetic energy which is transformed to radiation by thermalization.

Assuming energy conservation and a neutron star as accretor, the energy of a proton approaching the neutron star can be written as:

$$\frac{1}{2}m_p v_{\text{ff}}^2 = \frac{GMm_p}{r} \quad (2.17)$$

with m_p the mass of the proton, v_{ff} the free-fall velocity and r the distance to the neutron star. Using the Schwarzschild radius with $R_S = 2GM/c^2$ and the assumption that the complete energy is transformed to radiation on the surface of the neutron star with Radius R , the released energy per second, called luminosity, can be written as:

$$L = \frac{1}{2}\dot{m}c^2 \left(\frac{R_S}{R} \right), \quad (2.18)$$

with \dot{m} as the mass accretion rate.

It can be seen that the luminosity is higher for a higher mass accretion rate. Furthermore, the luminosity increases if the accretor is more massive or of smaller radius. Hence, compact objects like neutron stars or black holes are the most

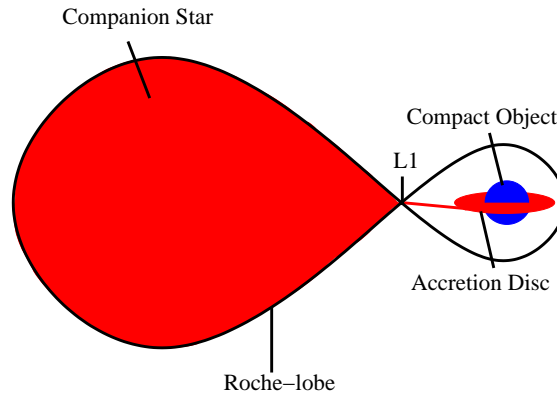


Figure 2.5: Schematic illustration of accretion via Roche-lobe overflow. The companion star fills its Roche-lobe and matter can be transferred to the compact object. The matter passes the intercepting point of the Roche-lobes which is called Lagrangian Point 1 (L1). Due to the conservation of angular momentum an accretion disc is formed around the compact object.

efficient accretors. However, at some point the outgoing radiation pressure is higher than the inward directed gravitational force and the infalling matter is stopped. This limit was first calculated by Sir Arthur Eddington. For a spherical accretion onto a compact object with mass M this limit can be determined to

$$L_E = 1.3 \times 10^{38} \left(\frac{M}{M_\odot} \right) \text{ erg s}^{-1}. \quad (2.19)$$

Nevertheless, it was shown that accretion can describe the observed luminosities, the companion star must first lose the matter. In X-ray binaries, two scenarios are possible in which the compact object accretes matter. Firstly, Roche-lobe overflow will be discussed.

Roche-lobe overflow

The gravitational potential in a binary system can be expressed by

$$\phi = -\frac{GM_1}{r_1} - \frac{GM_2}{r_2} - \frac{\omega^2 r^2}{2}, \quad (2.20)$$

with r_1 and r_2 defined as the distances from the center of the two stars, one with mass M_1 and the other with mass M_2 . Furthermore, r is the distance of the center of momentum and ω is the orbital frequency. This leads to equipotential surfaces whereas the surface which surrounds both stars is called the Roche-lobe. Within the Roche-lobe a particle is gravitationally bound to the central object. However, in a binary system the Roche-lobes of the two objects intersect in a point between the stars which is called the Lagrangian point L1. When one of the objects is a

Table 2.1: Typical X-ray binary parameters

	HMXB	LMXB
Companion star	$> 10 M_{\odot}$	$\sim 1 M_{\odot}$
Binary separation	$\sim 20 R_{\odot}$	$\sim 2 R_{\odot}$
Orbital period	\sim days	\sim hours
Lifetime	$\sim 10^5$ yr	$\sim 10^7$ yr

main-sequence star, it evolves and expands until it fills its Roche-lobe, now matter can be transferred via the L1, as it is shown in Figure 2.5.

Stellar wind accretion

Another accretion mechanism is capturing matter from a stellar wind with velocity v_W . However, it is not as efficient as accretion via the L1 since the stellar wind is uniformly distributed. Therefore, the mass loss rate of the companion star is thinned out to a fraction of $4\pi a^2$, where a is the distance of the two stars. The matter accreted by the compact object can be calculated by

$$\dot{M} \sim \frac{\pi r^2}{\Omega a^2} \dot{M}_W, \quad (2.21)$$

with the radius defined as $r = 2GM/v_W^2$ and \dot{M}_W the mass loss rate.

Although it is not an efficient process, a substantial amount of matter can be accreted if a strong stellar wind is present.

2.2.2 Formation

X-ray binaries are subdivided into High-Mass X-ray Binaries (HMXBs) and Low-Mass X-ray Binaries (LMXBs) which properties are summarized in Table 2.1. The formation processes will be discussed separately for both and is based on Lewin & van der Klis (2006). First of all, a binary system of two main-sequence stars is necessary.

High Mass X-ray Binaries

For HMXBs, the preceding binary system has to consist of two main-sequence stars with each exceeding $12M_{\odot}$. Alternatively, one star can be more massive and during its evolution becomes big enough to fill its Roche-lobe. Hence, the other star can accumulate matter by Roche-lobe overflow via the Lagrangian point L1. Nevertheless, one component of the system has to evolve faster and finally explode in a supernova. A compact object, such as a neutron star, could remain. The compact object can now accrete matter from the companion star by catching the

stellar wind. At this stage of the evolution the system is called a High-mass X-ray binary. The lifetime of the system depends on the mass of the companion star and its evolution. In Table 2.1 the most important parameters of HMXBs are summarized.

Low Mass X-ray Binaries

To end up with a LMXB system, two main-sequence stars with a significant mass difference are necessary. The more massive star typically has a mass of about $15 M_{\odot}$ and the companion a mass of around one solar mass. Some of the parameters of LMXBs are summarized in Table 2.1.

The more massive star evolves faster and fills its Roche-lobe. In certain circumstances, the massive star can expand until it encloses the companion. During this common envelope phase the companion spirals in. The massive star loses matter and evolves into a supernova whose remnant could be a neutron star or a black hole. Finally, the companion evolves and fills its Roche-lobe. Therefore, the compact object accretes matter by Roche-lobe overflow via the Lagrangian point L1.

Due to conservation of angular momentum, an accretion disk is formed around the compact object. The angular velocity in the disk depends on the radius and can be expressed by the Keplerian velocity:

$$\omega_{\text{K}}(R) = \sqrt{\frac{GM}{R}} \quad (2.22)$$

where G is the gravitational constant, M is the mass of the central object and R is the radius of an annulus of the disk. As it can be seen, each annulus of the disk moves with a different velocity and therefore a shear force is present. This leads to friction which can transport angular momentum and allows the matter to spiral inward and finally it can be accumulated onto the compact object.

The disk itself is optically thick, which means that the mean free path of a photon is short compared to the size of the disk and the disk is therefore a source of thermal emission. Furthermore, it is geometrically thin which means that the height H of the disk is much less than the radius which can be estimated following Lewin & van der Klis (2006):

$$H \simeq \frac{c_{\text{s}}}{\omega_{\text{K}}} R \ll R \quad (2.23)$$

with c_{s} as the local speed of sound.

Since the central object is compact, relativistic effects have to be taken into account. Therefore, orbits close to the compact object are not stable and an innermost stable circular orbit (ISCO) can be determined using the Schwarzschild metric for a non-rotating compact object:

$$R_{\text{ISCO}} = \frac{6GM}{c^2} = 3 R_{\text{s}} \quad (2.24)$$

This is the innermost theoretically allowed radius of an accretion disk. If the radius of the neutron star is as large as the ISCO, the accretion disk reaches down to the surface of the neutron star. Otherwise, the orbits inside the ISCO are not stable and therefore a gap is present between the inner part of the accretion disk and the neutron star in which the matter does not follow Keplerian orbits.

2.3 Properties of X-ray binaries

Since there are different physical components in an X-ray binary system, there are also different features in both spectra and light curves. In the following, the properties of, in particular, LMXBs are discussed.

2.3.1 Spectral properties

Blackbodies

Looking first at the companion star, it is not expected to observe any significant X-ray radiation from it because of the low temperature of around 5000 K. However, the compact object, here a neutron star, is hot enough to emit X-rays. Typically, the radiation is approximated with a blackbody with a temperature in the order of a fraction of keV up to a few keV (see for example Ng et al. 2010).

Furthermore, the accretion disk can be seen as a composition of several blackbodies of different temperatures which superimpose to a so-called multicolor blackbody with typical temperatures of about 1 keV.

Fluorescence lines and Reflection

In addition, the accretion disk is irradiated by the emission from the central object and, therefore, fluorescence can take place in the disk. In LMXB systems the most prominent fluorescence feature is typically the iron $K\alpha$ line which is formed when an electron of the L-shell fills the vacancy in the K-shell. The shape of the line is determined by the inner radius of the disk and the inclination under which the system is seen. An overview of the effects is given by Fabian et al. (2000) and Fabian (2008). First of all, the energy of the line depends on the ionization state of the iron atom. For higher ionization levels the centroid line energy increases. But not only the energy can differ, the width and the symmetry of the line can vary for different conditions. A double peaked line profile is created by simple Newtonian motion of the disk caused by the Doppler effect. The part of the disk which is approaching the observer is blue-shifted whereas the receding part is red-shifted. Furthermore, since the production of the line takes place close to a compact object, relativistic effects have to be taken into account. The whole profile is red-shifted due to gravitational redshift which is an effect of general relativity. However, in the inner parts of the disk matter moves with high velocities, therefore special relativity

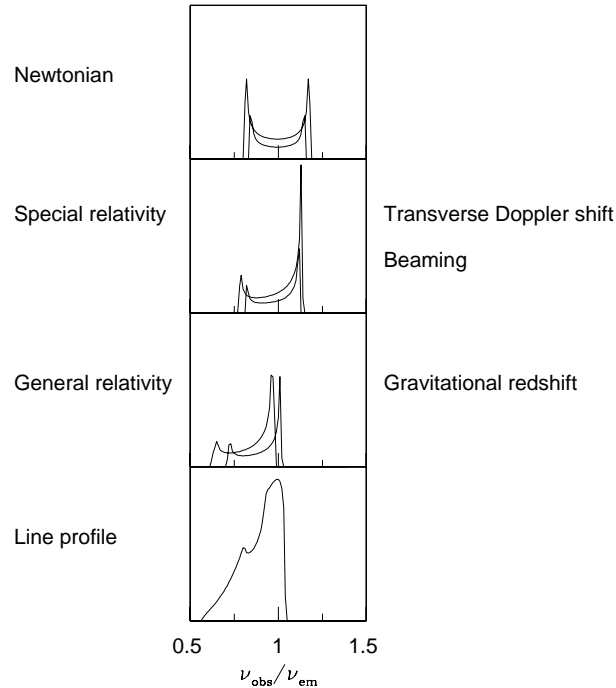


Figure 2.6: Illustration of the effects which shape a relativistic line profile, Fabian et al. (2000)

effects also occur. Also the effect of time dilation, or transverse Doppler shift, moves the whole profile to longer wavelengths. In addition, relativistic beaming enhances the blue part of the profile, due to the fact that radiation is pointing in the direction of movement. Altogether, the result of these effects is a broadened, asymmetric line profile. The influence of the individual effects on the shape, as well as the resulting profile, are shown in Figure 2.6. However, the accretion disk contains also other elements, like argon or calcium, and therefore, also other fluorescence lines can be detected, as well as a reflection component which manifests itself in a broad hump around 30 keV (see for example (Lightman & White 1988)).

Comptonization

It is still under discussion where another spectral component, the Comptonization component, has its origin. Two main ideas have been accepted: the Western (White et al. 1988) or Birmingham Model (Church & Balucinska-Church 1995), and the Eastern model (Mitsuda et al. 1984, 1989). In the Western model, the blackbody component arises from the neutron star and the additional Comptonization component originates from a hot, optically thin region in the vicinity of the disk as shown in the upper panel of Figure 2.7 which is called extended Accretion Disk Corona (ADC). In contradiction to this, the Eastern model claims that a

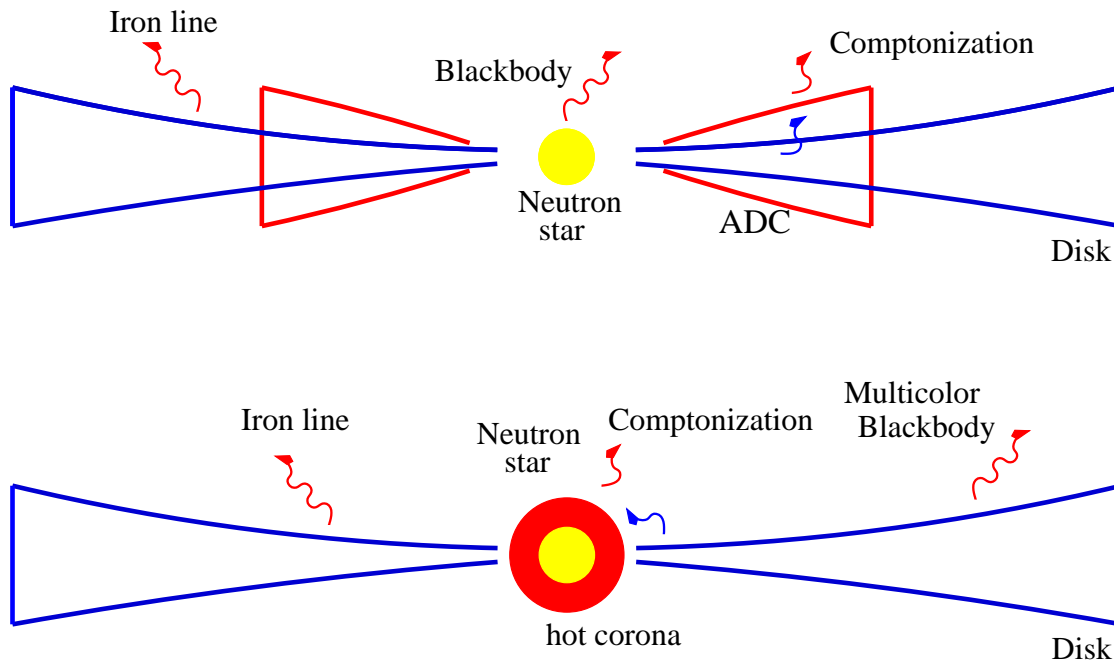


Figure 2.7: *Upper panel:* Illustration of the Western model. A blackbody spectrum is emitted from the neutron star surface and Comptonization takes place in the Accretion Disk Corona (ADC). *Lower panel:* Illustration of the Eastern model. A multicolor blackbody spectrum originates from the accretion disk whereas a Comptonized spectrum is emitted by a hot corona close to the neutron star. Both illustrations are based on Church & Balucinska-Church (2004).

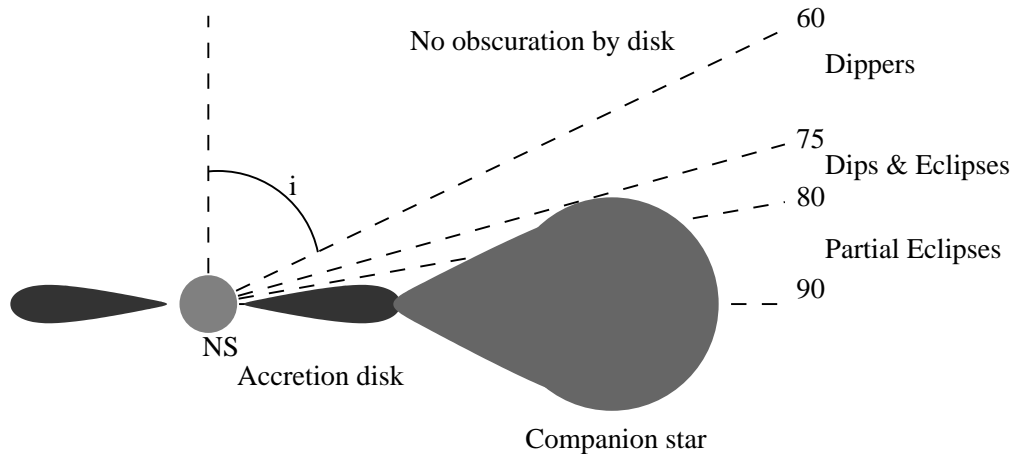


Figure 2.8: Sketch of a low-mass X-ray binary system. Dips and eclipses occur for higher inclination angles i , illustration is based on Seward & Charles (1995).

multicolor blackbody arises from the accretion disk and the Comptonization takes place close to the neutron star in a hot corona around the compact object (shown in the lower panel of Figure 2.7). Nevertheless, the necessity of a Comptonization component is proven.

Power-law

Finally, in some sources also a jet was observed which can produce a power-law up to 200 keV by Comptonization with very hot electrons. An overview of possible mechanisms which can produce such a power-law is given by Di Salvo & Stella (2002).

2.3.2 Timing properties

Bursts

The main source of power for LMXB systems is accretion. However, the matter does not just disappear, in the case of a neutron star, it is accumulated on the surface of the compact object. At some well-defined point, the pressure and density are high enough to ignite the hydrogen and it is burned into helium. This explosion can be observed as a Type-I X-ray burst.

Dips and Eclipses

Since the accretion disk is opaque for X-rays, some temporal features are caused by the geometry of the system. However, if the inclination angle under which the system is seen is below 60° , the source can be observed unobscured. If the inclination is larger, the companion star can occult the compact object and the

accretion disk. Therefore, dips and eclipses are observed. An illustration of the configuration is given in Figure 2.8.

kHz QPOs

As shown in Table 2.1, LMXB systems are compact systems in which processes take place on a small length scale. Due to this, variabilities of the source on short time scales are also expected. After detectors were developed to allow observations with a time resolution of below 1 ms, the so-called kilohertz Quasi-periodic Oscillations were detected (kHz QPOs, see van der Klis et al. 1996; van der Klis 2006, for a review). Such oscillations are only visible in a Power Spectral Density (PSD) plot which can be produced by a Fourier transformation of the light curve.

The origin of kHz QPOs is still under discussion. However, it is an accepted fact that the oscillations have to take place in the accretion disk in regions very close to the neutron star. This can easily be verified by using the equation for Keplerian orbits which gives the frequency

$$\nu_K = \frac{\sqrt{GM/r^3}}{2\pi} \approx 1184 \text{ Hz} \left(\frac{r}{15 \text{ km}} \right)^{-3/2} m_{1.4}^{1/2}, \quad (2.25)$$

with $m_{1.4}$ the mass of the compact object in units of $1.4 M_\odot$, and r the orbital radius.

In addition, using the definition of the innermost stable circular orbit (ISCO) in the Schwarzschild metric

$$R_{\text{ISCO}} = \frac{6GM}{c^2}, \quad (2.26)$$

an impression of the maximal frequency can be given as

$$\nu_{\text{ISCO}} = \frac{c^3}{2\pi 6^{3/2} GM} \approx \frac{1566}{m_{1.4}} \text{ Hz}. \quad (2.27)$$

Finally, assuming that the oscillations take place at the ISCO, it is possible to determine the mass of the neutron star.

The basic idea of the common models to describe kHz QPOs is the origin of a clump of matter in the disk which rotates with a certain Keplerian frequency around the neutron star. Additionally, a non-uniform structure, like a radiation pattern, on the surface of the neutron star has to exist which beats the clump. Different models using this basic principle exist with most of them discussed by Miller et al. (1998).

Atoll and Z-sources

To get an impression of the variability on longer timescales, such as some seconds or up to some hundreds of seconds, a color-color diagram is created. In a color-color diagram the flux in a high energy range is divided by the flux in a medium energy

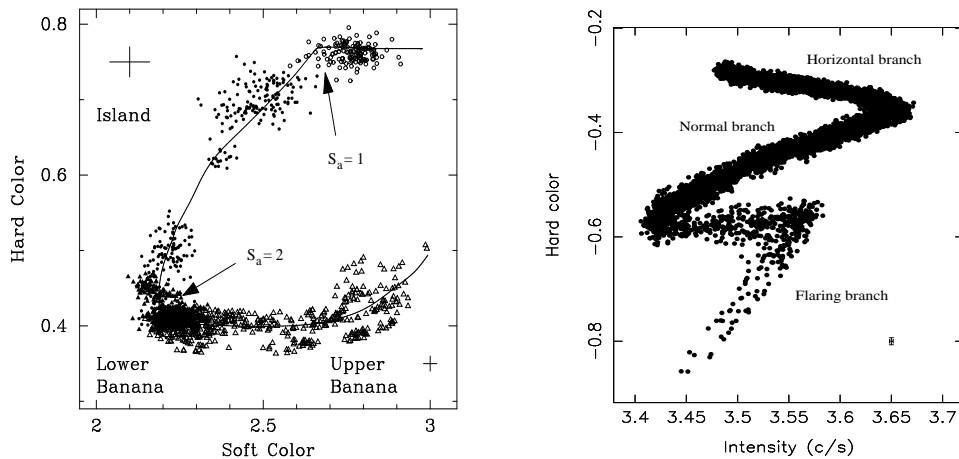


Figure 2.9: *Left panel:* Color-color diagram of an *atoll source* (4U 1608-52, Méndez et al. 1999). *Right panel:* Hardness-Intensity diagram of a *Z-source* (GX 340+0, Jonker et al. 1998).

range. The result is called the hard color. Furthermore, a soft color is calculated by dividing the flux in the medium energy range by the flux in a low energy range. Finally, the hard color is plotted over the soft color. Hasinger & van der Klis (1989) made a systematic analysis and found that two kinds of LMXBs exist. An overview of the differences is given by van der Klis (2006).

First, there are the so-called *atoll sources* which are named due to their characteristic shape in the color-color diagram (shown in the left panel of Figure 2.9).

In general, *atoll sources* have a luminosity up to $0.2 L_{\text{Edd}}$. The island state at the upper end of the color-color diagram is the lower luminosity state which is dominated by high frequency noise, whereas the banana state occupies the lower left to the lower right of the diagram. The banana state, which is subdivided into the lower and upper banana, is the higher luminosity state of an *atoll source*. The time variability is dominated by high frequency noise and also kHz QPOs can be observed.

The other group is also named according to its shape in the color-color diagram, namely the *Z-sources*. A *Z-source* is characterized by the horizontal branch with oscillations which show quasi-periodic behaviour, however, not up to kilohertz frequencies. Furthermore, the normal branch shows weaker variability and finally the spectrum of the flaring branch is thermal and no significant time variability can be observed.

CHAPTER 3

ANALYSIS OF 4U 1735-44 WITH *BEPPoSAX* AND *XMM-NEWTON*

In the course of this thesis, X-ray data obtained by two satellites, namely *BeppoSAX* (see Section 1.2) and *XMM-Newton* (see Section 1.3), were analysed. The results have been published in Mück et al. (2013).

4U 1735–44 is a low-mass X-ray binary whose general features were discussed in Section 2.2.2. In the analysis of the *XMM-Newton* data, especially the effect of pile-up has been taken into account. A more detailed study of these effects was performed in the course of this work.

In the following, an overview of the main features of the source is given. Afterwards, spectral models used to characterize the data will be described. Finally, the analysis results of the *BeppoSAX* observations, as well as the results of the *XMM-Newton* observation, will be discussed.

3.1 Introduction of the source 4U 1735–44

The source 4U 1735–44 is a low-mass X-ray binary system located at a distance of $6.5 (\pm 1.0)$ kpc as determined by Galloway et al. (2008) by analysing type-I X-ray bursts. Furthermore, van Paradijs et al. (1988) detected the first of such bursts from the source with *EXOSAT* observations. Hasinger & van der Klis (1989) classified 4U 1735–44 as an *atoll source* with a flux of about 4×10^{-9} erg cm $^{-2}$ s $^{-1}$ in the 2 keV–10 keV range. Accretion is driven by Roche-lobe overflow. Using the good timing capability of the *RXTE* satellite (Jahoda et al. 1996) it was possible to observe kHz QPOs with a frequency of 1150 Hz (Wijnands et al. 1996, 1998). In a later observation, Ford et al. (1998) detected two simultaneous kHz QPOs which showed a frequency separation of 300 Hz.

Observations in the optical waveband by Casares et al. (2006) allowed the measurement of the mass of the main-sequence companion star to be $0.53 (\pm 0.44) M_{\odot}$. Furthermore, with the help of optical photometry the orbital period was determined

to be 4.654 ± 0.005 h (Corbet et al. 1986).

Observations performed by *Ginga* (Makino 1987) and *ROSAT* (Truemper 1982) were analysed by Seon et al. (1997). The resulting broad-band spectrum was modeled by a combination of a blackbody and a Comptonization model. Line features were modeled by simple Gaussian models. Searching for iron lines, Cackett et al. (2009) and Torrejón et al. (2010) analysed *Chandra* (Weisskopf et al. 2002) data. Both found no evidence for an iron line in their observations which were taken at a luminosity varying between 2.77×10^{37} erg s⁻¹ and 3.37×10^{37} erg s⁻¹. However, Ng et al. (2010) found an iron line in the spectrum of 4U 1735–44 which was modeled with a Gaussian with an equivalent width of $43(\pm 13)$ eV and a centroid line energy of $6.74(\pm 0.10)$ keV. Compared to the *Chandra* observations, the *XMM-Newton* observation revealed a slightly higher luminosity of 3.98×10^{37} erg s⁻¹.

Different continuum models were used in these previous studies. Therefore, the exact understanding and correct use of the models is essential.

3.2 Details of the applied source models

The analysis of the spectra within this work was performed using the spectral fitting package XSPEC v12.7.1 (Arnaud 1996). XSPEC can perform spectral studies of many instruments from which data is given in the OGIP FITS standard (Arnaud K.A. 2009). Plenty of models are implemented to characterize different physical processes. After the spectral dataset is loaded with the corresponding response files, the models are applied and a fit is performed. The quality of a fit can be determined using the χ^2 statistic:

$$\chi^2 = \sum_{I=0}^N (C(I) - C_p(I))^2 / \sigma(I)^2$$

with $C(I)$ are the observed counts, $C_p(I)$ the model predicted counts and $\sigma(I)^2$ the error for channel I. In Poissonian statistic the error is defined as $\sigma(I) = \sqrt{C(I)}$. To check the quality of the fit, the reduced χ^2 is often used. This can be determined by the ratio of the χ^2 and the degrees of freedom defined as the number of channels subtracted by the number of spectral parameters. The fit is statistically significant, if the reduced χ^2 is close to one.

Therefore, the used models can be evaluated and the best-fitting model can be found. In the following the models which were used to fit the presented data are described.

3.2.1 Absorption

The low energy part, up to about 2 keV, of an X-ray spectrum is affected by photoelectric absorption. Astrophysical photons pass through the interstellar medium which mainly consists of hydrogen. Photons interact with the atoms and can be

absorbed or scattered. To characterize this effect the traversed material is given in a equivalent hydrogen column with 10^{22} atoms per cm^2 . Following Longair (2011) the net absorption cross-section σ_e of the interstellar material can be calculated by summing up the individual cross-sections σ_i weighted by their abundance n_i :

$$\sigma_e(\epsilon) = \frac{1}{n_{\text{H}}} \sum_i n_i \sigma_i(\epsilon) \quad (3.1)$$

In most cases the absorption edges of the different elements cannot be resolved and therefore an approximation is used. Finally, the optical depth can be written as

$$\tau_e(\hbar\omega) = \int \sigma_e n_{\text{H}} dl = 2 \times 10^{-26} \left(\frac{\hbar\omega}{1 \text{ keV}} \right)^{-8/3} \int N_{\text{H}} dl \quad (3.2)$$

which only depends on the energy of the photon $\hbar\omega$ and the column depth $\int n_{\text{H}} dl$.

In XSPEC the photoelectric absorption is implemented in a variety of models¹. They differ in the calculation of the cross-section and in the given abundances of the elements. In the presented analysis, the PHABS model was used which implements the photoelectric cross-section σ_e without considering Thomson scattering. The hydrogen column n_{H} is given in XSPEC in units of 10^{22} atoms per cm^{-2} . The cross-sections are based on the calculations by Balucinska-Church & McCammon (1992) and Yan et al. (1998) whereas the abundances are set to the solar values determined by Anders & Grevesse (1989). In total, the intensity decreases exponentially:

$$I(E) = I_{\star} e^{-n_{\text{H}}\sigma(E)} \quad (3.3)$$

with I_{\star} the intrinsic intensity.

3.2.2 Blackbody

As discussed in Section 2.3.1, blackbody radiation is one of the dominating processes in LMXB systems. Although a perfect blackbody radiation cannot exist in reality as described in Section 2.1.1, it describes very well the observed data. The model BBODY is implemented as

$$I(E) = \frac{K \times 8.0525 E^2 dE}{(kT)^4 [\exp(E/kT) - 1]} \quad (3.4)$$

with kT as the temperature of the blackbody in keV. The normalization K is defined as L_{39}/D_{10}^2 where L_{39} is the luminosity in units of 10^{39} erg s^{-1} and D_{10} is the distance of the source in units of 10 kpc.

Furthermore, the DISKBB model is used to describe the spectrum of an accretion disk which consists of multiple blackbody components. The parameters are the temperature at the inner disk in keV and the normalization which is given by

$$k_{\text{DBB}} = \left(\frac{R_{\text{in}}/\text{km}}{D/10 \text{ kpc}} \right)^2 \cos \theta \quad (3.5)$$

¹<http://heasarc.nasa.gov/xanadu/xspec/manual/Models.html>

with R_{in} as the apparent inner disk radius, D the distance of the source and θ the inclination angle of the disk. The DISKBB model was developed by Mitsuda et al. (1984) and Makishima et al. (1986).

3.2.3 Comptonization

Comptonization can be often modeled by a power-law, however, a better description is provided by the NTHCOMP model. The model was proposed by Zdziarski et al. (1996) and was extended by Zycki et al. (1999). As described in Section 2.1.2, photons are scattered to higher energies by inverse Compton scattering. The seed photons can be either provided by a blackbody or by a disk blackbody with a temperature kT_{bb} . The hot electron plasma is defined by the electron temperature kT_e . Furthermore, the model depends on the asymptotic power-law photon index γ and the normalization K which is set to unity for 1 keV.

3.2.4 Reflection

In systems with a central object and a surrounding disk which is illuminated by a power-law like radiation, reflection can occur as indicated in Section 2.3.1. To characterize such a process, Ross & Fabian (2005) proposed the REFLIONX model which calculates a reflection spectrum for an optically-thick atmosphere. The conditions are fulfilled in the surface of an accretion disk. Several ions are included in the calculation, starting from carbon and ending with iron. Hence, also the iron K_α line is modeled.

The shape of the model spectrum depends on the iron abundance relative to the solar value, whereas the abundances of the other elements are set to values obtained by Morrison & McCammon (1983). Further parameters are the power-law photon index γ of the illuminating radiation as well as the ionization parameter ξ which is defined as $\xi = 4\pi F/n$ where F is the illuminating flux and n the hydrogen number density.

3.2.5 Line

It is not always possible to model fluorescence lines, as discussed in Section 2.1.4, with a reflection model. XSPEC provides a simple GAUSSIAN model, described by:

$$I(E) = K \frac{1}{\sigma\sqrt{2\pi}} \exp\left(-\frac{(E - E_c)^2}{2\sigma^2}\right) \quad (3.6)$$

where E_c is the centroid line energy, σ the width of the line and K the normalization which is defined as the total number of photons per cm^2 and second in the line.

If relativistic effects have to be taken into account, as described in Section 2.3.1, a simple GAUSSIAN model is not sufficient to model the line profile. Fabian et al. (1989) have proposed a model for line emission from a relativistic accretion disk,

Table 3.1: Summary of the analysed *BeppoSAX* observations

OBS-ID	Beginning in UT	End	LECS	MECS	HPGSPC in ks	PDS
2083600200	03/20/2000	03/21/2000	14.1	38.7	18.4	19.0
Obs 1	17:03:58	14:21:58				
2122400300	08/26/2000	08/27/2000	14.5	41.8	33.1	19.6
Obs 2	02:59:56	04:24:45				
2122400400	09/25/2000	09/25/2000	7.2	17.7	15.7	7.9
Obs 3	06:31:21	16:04:16				
2122400410	09/27/2000	09/27/2000	5.1	16.6	13.2	6.8
Obs 4	12:41:39	23:39:30				

first used to model the spectrum of Cygnus X-1 in which broad iron lines were found for the first time by Barr et al. (1985). Such lines were also observed later on in the AGN MCG-6-30-15 (Tanaka et al. 1995). The model is implemented in XSPEC as DISKLINE. The profile depends on the line energy and a parameter for the scale of the emissivity. Further parameters are the inner and outer radius in units of GM/c^2 as well as the inclination under which the system is seen. Finally, the normalization is, as for the GAUSSIAN model, the total number of photons per cm^2 per second.

3.3 Analysis of *BeppoSAX* data

3.3.1 Data extraction and selection

In this work the results of four archival *BeppoSAX* observations are presented which were performed to achieve a broad-band spectrum of a low-mass X-ray binary. The observation dates and durations are summarized in Table 3.1.

The data were extracted using the SAX tools which were included in a previous version (v.5.3) of the HEASOFT² package. Following the instructions given in the NFI spectral analysis handbook³, the spectra of the four instruments were obtained. The response and ancillary response files of all four instruments were taken from the mission homepage⁴.

The spectra and the light curves of the LECS instrument were extracted from a region of $8'$ radius around the source center. Whereas for the MECS, a region of $4'$ was used. The corresponding background spectra were obtained by extracting data from empty field observations provided by the instrumental teams.

²<http://heasarc.nasa.gov/lheasoft/>

³<http://www.asdc.asi.it/bepposax/software/index.html>

⁴ftp://ftp.asdc.asi.it/sax/cal/responses/98_11/

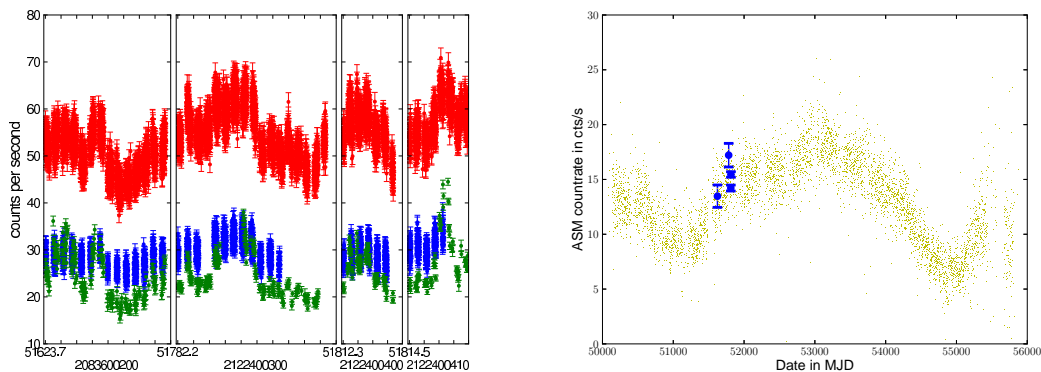


Figure 3.1: *Left panel:* The *BeppoSAX* light curves of all four observations of 4U 1735–44 of all used instruments. The LECS light curve (16 seconds binning) is shown in blue, the MECS (16 seconds binning) in red and the HPGSPC light curve (196 seconds binning) in green. *Right panel:* Complete *RXTE* ASM light curve. The *BeppoSAX* observations are marked in blue.

Unfortunately, it was not possible to use the data obtained by the PDS detector. Systematic effects were found above 20 keV which originate from the location of the source close to the galactic plane. As mentioned in Section 1.2, the background spectrum for the PDS instrument is achieved by rocking the instrument. Therefore, during the off-pointing the galactic plane coincided with the field of view which leads to an increased number of events in the background spectrum.

In the analysis of the HPGSPC data, in three of four observations the collimator was not rocking and therefore, the background was measured by taking data when the source was occulted by the Earth (as suggested in the handbook and discussed in Section 1.2.5). To assess any systematic effect, the spectra were compared to the background spectrum which could be extracted from the off-minus rocking of Obs 1. The spectra show the same features and an identical overall shape. However, summing all four Earth occultation spectra together provides better statistics, hence, the summed spectrum is used as background spectrum for all four observations.

3.3.2 Timing analysis

At first, light curves of all used observations were extracted. A 16second time binning was applied to produce the LECS and the MECS light curves, whereas the HPGSPC light curve was binned to 196 seconds. Afterwards, the light curves were checked for bursts. However, no bursts were found in all instruments (see left panel of Figure 3.1). Furthermore, it is apparent that the overall shape of the light curves is similar.

To classify the observations with respect to the history of the source, the light curve of the All Sky Monitor (ASM, Levine et al. 1996) on board of *RXTE* is

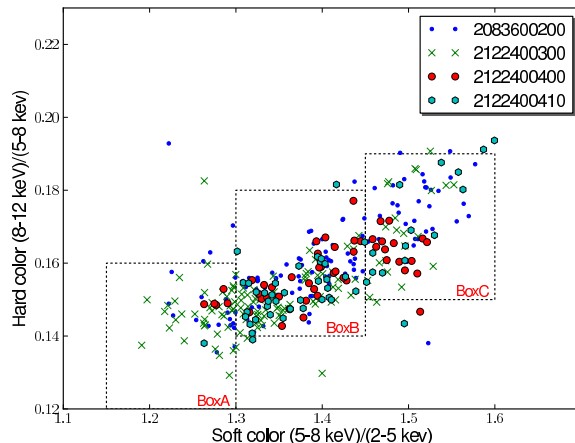


Figure 3.2: Color-color diagram of all four *BeppoSAX* observations of 4U 1735–44. One point represents 400 seconds of observation. The boxes indicate regions of the color-color diagram from which spectra were extracted to check for spectral changes along the path of the diagram (Mück et al. 2013).

shown. In the right panel of Figure 3.1 it can be seen that during the *BeppoSAX* observations the ASM flux varies between 13 cts/s and 17 cts/s. During the time between the observations the source showed no large variability.

Furthermore, a color-color diagram, as described in Section 2.3.2, of the MECS data was produced with the hard color defined as the ratio of the flux in the 8 keV–12 keV and the flux of the 5 keV–8 keV range and the soft color as the ratio of the flux in the 5 keV–8 keV range and the flux in the 2 keV–5 keV range. During all *BeppoSAX* observations the plot, shown in Figure 3.2, indicates that the source was in the banana state of an *atoll source*. The boxes in the plot mark regions from which spectra were extracted to check for spectral changes in the transition from the lower to the upper banana state.

3.3.3 Spectral analysis

To analyse the spectra of the *BeppoSAX* data in well calibrated energy ranges, energy bins were removed. For the LECS data the energy range from 0.2 keV–3.0 keV was used, the MECS data was used from 1.7 keV–10.0 keV and the HPGSPC data was analysed in the energy range of 7.0 keV–24.0 keV. In general, the HPGSPC data can be used up to 60 keV, however, in the present case the background dominates above 24 keV. Furthermore, a systematic error of 2% was applied to the HPGSPC data, to take the uncertainties in the background subtraction and in the calibration into account.

First of all, the continuum was fitted with different combinations of models in

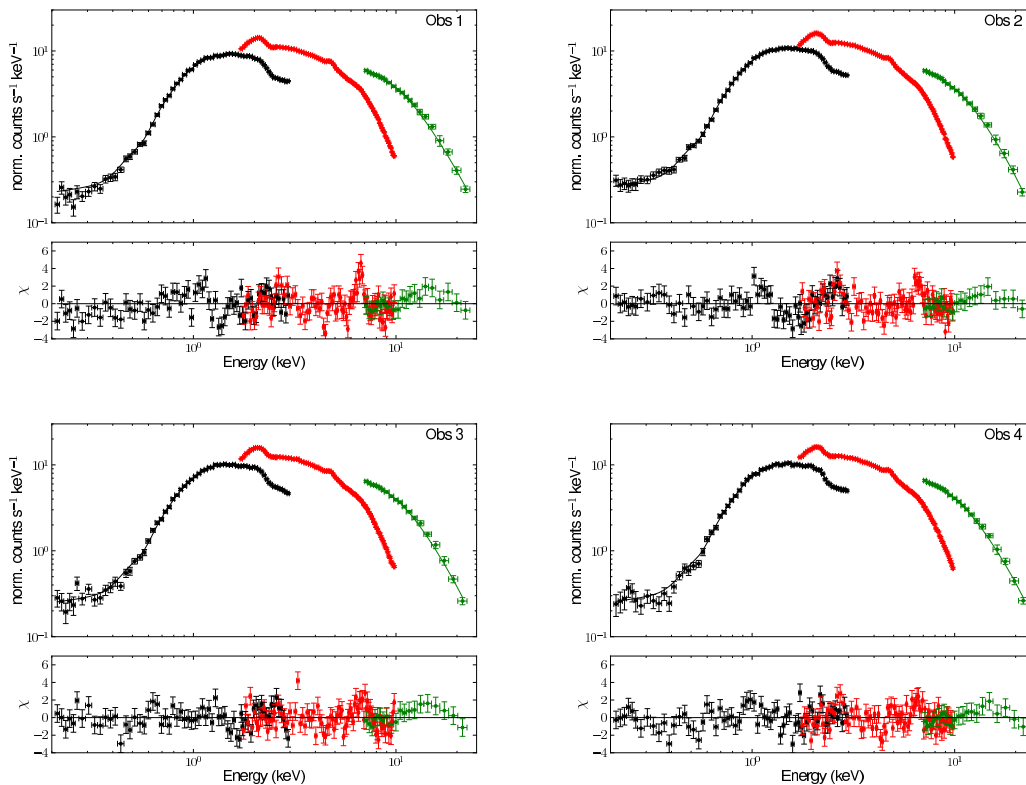


Figure 3.3: Shown are the spectra and residuals of the four *BeppoSAX* observations of 4U 1735–44 when the data were fitted with the model $\text{PHABS} \times (\text{DISKBB} + \text{NTHCOMP})$.

XSPEC. The best fits were obtained by using an absorbed (PHABS) combination of a multicolor disk-blackbody (DISKBB) and a Comptonization component modeled with NTHCOMP. However, after modeling the continuum, residuals of line-like features were present, as it is shown in Figure 3.3, together with the overall spectrum. These features could be modeled by Gaussian lines. The more physical model REFLIONX was also capable of fitting the data. Indeed, the fit statistics were slightly better in terms of reduced χ^2 (1.387 for 167 dof compared to 1.262 for 168 dof for Obs 1). Therefore, all four observations were fitted with the same model and all gave good fit statistics and residuals which show no need for an additional spectral component. The best-fit values are reported in Table 3.2 and the unfolded spectra as well as the residuals with the REFLIONX model included are shown in Figure 3.4.

Furthermore, spectra were extracted from different regions of the color-color diagram indicated in Figure 3.2 by the boxes BoxA, BoxB and BoxC. Different regions of the banana state of an *atoll source* are covered in this way. The spectra are shown on the left side of Figure 3.5. The different regions are color coded and it

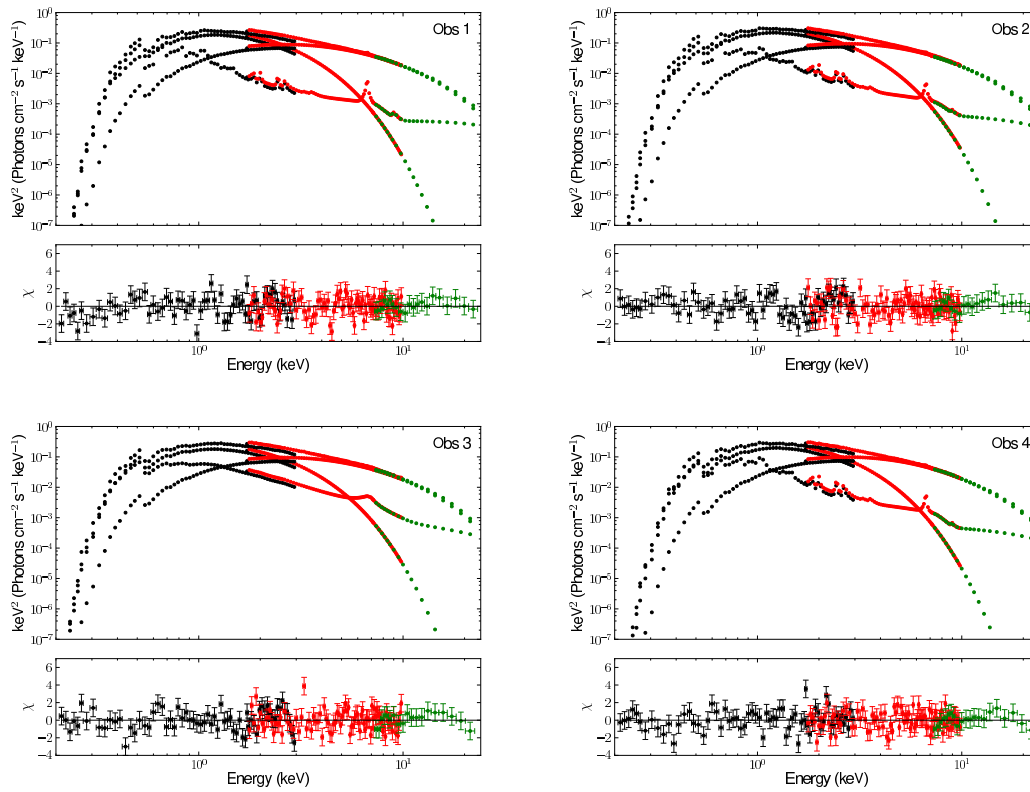


Figure 3.4: Shown are the unfolded spectra and residuals of the four *BeppoSAX* observations of 4U 1735–44 when the data were fitted with the model $\text{PHABS} \times (\text{DISKBB} + \text{NTHCOMP} + \text{REFLIONX})$.

Table 3.2: Best fit results for the four *BeppoSAX* observations

Parameter	Obs 1	Obs 2	Obs 3	Obs 4
$N_{\text{H}}[10^{22} \text{ cm}^{-2}]$	$0.33^{+0.01}_{-0.02}$	$0.33^{+0.02}_{-0.02}$	$0.30^{+0.01}_{-0.01}$	$0.37^{+0.03}_{-0.03}$
$kT_{\text{dbb}}[\text{keV}]$	$0.66^{+0.07}_{-0.16}$	$0.83^{+0.03}_{-0.03}$	$0.76^{+0.07}_{-0.06}$	$0.80^{+0.04}_{-0.03}$
k_{dbb}	432^{+430}_{-115}	251^{+34}_{-28}	288^{+90}_{-70}	291^{+46}_{-49}
Γ	1.62_{fixed}	2.19_{fixed}	1.78_{fixed}	2.31_{fixed}
$kT_{\text{e}}[\text{keV}]$	$2.60^{+0.04}_{-0.04}$	$3.20^{+0.14}_{-0.14}$	$2.80^{+0.06}_{-0.05}$	$3.42^{+0.15}_{-0.15}$
$kT_{\text{bb}}[\text{keV}]$	$0.81^{+0.14}_{-0.31}$	$1.34^{+0.04}_{-0.04}$	$1.05^{+0.10}_{-0.04}$	$1.38^{+0.04}_{-0.04}$
$k_{\text{comp}}[10^{-2}]$	$13.6^{+6.0}_{-3.6}$	$7.3^{+0.6}_{-0.5}$	$10.2^{+2.0}_{-2.0}$	$7.6^{+0.6}_{-0.6}$
$X_{\text{Fe}}/\text{solar}$	$1.69^{+0.51}_{-0.43}$	$0.94^{+0.64}_{-0.21}$	$3.23^{+4.78}_{-2.10}$	$1.40^{+1.46}_{-0.57}$
ξ	298^{+132}_{-43}	550^{+139}_{-207}	1996^{+523}_{-730}	559^{+192}_{-198}
$k_{\text{ref}}[10^{-6}]$	$13.5^{+5.6}_{-5.5}$	$5.33^{+4.61}_{-2.07}$	$0.94^{+0.87}_{-0.33}$	$7.07^{+3.00}_{-3.25}$
χ^2	212	194	197	193
D.o.f	168	167	167	171
red. χ^2	1.262	1.159	1.179	1.131

can be seen that the general shapes of the spectra are identical. Only the luminosity is different. To check for spectral changes, spectral parameters are plotted on the right side of Figure 3.5. The best-fit values are plotted related to the best-fit value of the region BoxA. The error ranges are plotted in the same scale. It can be seen that all parameter values are in between the error ranges. Therefore, it was not possible to state any significant spectral change of the source along the path of the color-color diagram.

3.4 Analysis of *XMM-Newton* data

3.4.1 Data extraction and selection

In this work EPIC-PN data of the source were analysed, which have been partially published by Ng et al. (2010). The observation was performed on the 3rd September 2001 with an exposure time of about 5.3 ks. The data were extracted using the *XMM* Science Analysis Software (SAS) version 12.0⁵. No background spectra were used since the standard method cannot be applied to observations performed in Timing Mode. In general the background is extracted from outer parts of the detector, however, in Timing Mode only one CCD is operated and the PSF affects also the outer parts of the chip. Therefore, it is difficult to get an uncontaminated background spectrum. This problem is widely discussed in Chapter 5.

⁵<http://xmm.esac.esa.int/sas/>

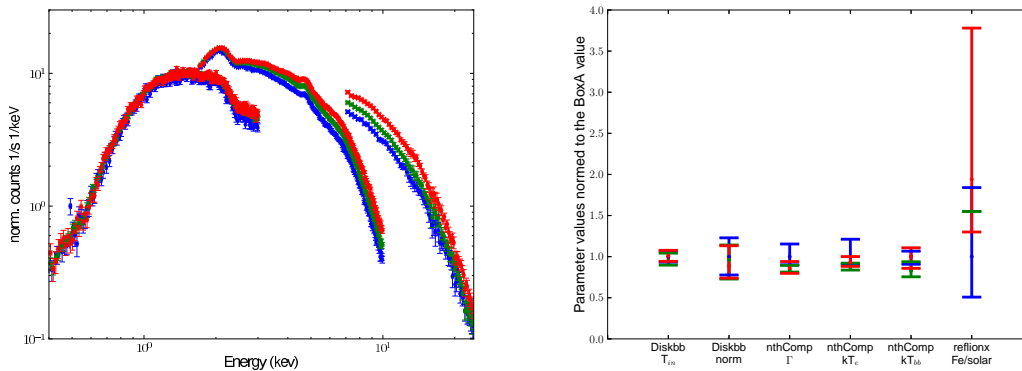


Figure 3.5: The spectra of the different color-color diagram boxes are shown on the left. The spectrum extracted from BoxA is marked in blue, BoxB in green and BoxC is marked in red. On the right side the best-fit parameters of the different boxes are compared. The values are normalized to the best-fit value of BoxA.

Despite the fact that the detector was working in Timing Mode, it was still necessary to check the observation for pile-up effects. Pile-up effects occurs when a photon hits the same or an adjacent pixel of the detector before the previous event is read out. A detailed description will be given in the following Chapter. To deal with pile-up, the suggested procedure is to exclude the inner columns of the PSF which are most affected. However, a significant fraction of source photons are discarded this way. Therefore, piled-up observations have to be treated carefully.

To estimate whether the observation is affected by pile-up the SAS task EPATPLOT⁶ can be used. In this task the observed pattern fractions are observed with the expected ones. Observations which suffer pile-up show an excess of double events, therefore a deviation from the model of the expected fraction gives an indication for pile-up. In the left upper panel of Figure 3.6 the EPATPLOT of the data extracted from a box with a width of 15 columns (region 1) centered at the bore-sight is shown. The resulting count rate is 1146 counts per second which is above the pile-up limit given in the user handbook. A clear deviation from the model can be seen. Therefore, the innermost column (region 2) was excluded, however, the plot still gives evidence for pile-up. Consequently, three (region 3) and five (region 4) columns were further excluded, for which the epatplots are shown in the lower panels of Figure 3.6. The rmf and the arf are produced using the SAS task RMFGEN and ARFGEN, respectively. When columns are excluded the generation of the ancillary response files is not straightforward. First of all, the arf of the whole 15 columns has to be generated, followed by the generation of the arf of the excluded region. Finally, the arf of the excluded region has to be subtracted from the arf of the whole region. The epatplots were checked carefully and it was decided to use

⁶<http://xmm.esac.esa.int/sas/current/doc/epatplot/index.html>

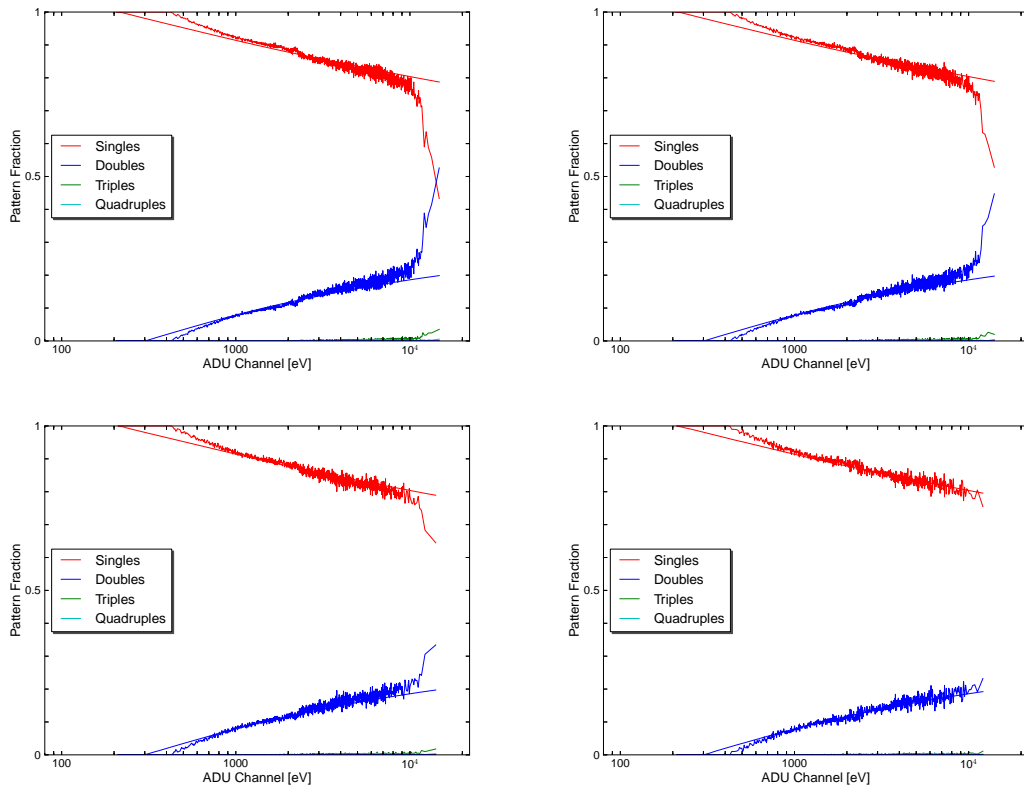


Figure 3.6: Shown are the epatplots of the four *XMM-Newton* extraction regions of 4U 1735–44. In the epatplot the pattern fractions of the observation are compared to expected ones. Clockwise starting from the upper left panel region 1 (all columns), region 2 (without one central column), region 3 (without three central columns) and region 4 (without five central columns) are presented.

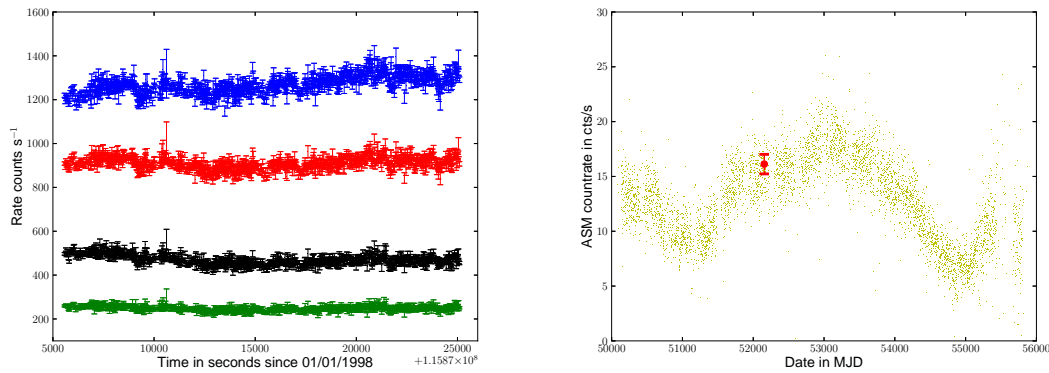


Figure 3.7: *Left panel:* Shown are the light curves of all four extraction regions (region 1 in blue, region 2 in red, region 3 in black and region 4 in green). All light curves are binned to 16 seconds. *Right panel:* Complete *RXTE* ASM light curve. The *XMM-Newton* observation is marked in red.

data obtained from region 3 up to an energy of 10 keV. The count rate is in the order of 470 counts per second which is in the border area in which pile-up effects occur.

Furthermore, the EPIC-MOS data were checked for usability. Both cameras were operated in partial window mode. Since this operation mode can handle a flux of two counts per second, a high fraction of pile-up is present. Therefore, the MOS cameras could not be used for the analysis.

3.4.2 Timing analysis

Analogous to the *BeppoSAX* analysis, the *XMM-Newton* data were checked for bursts. The light curve in the left panel of Figure 3.7 shows no evidence for bursts. Plotting the light curves of all four extraction regions illustrates the decrease of the count rate when omitting more central columns. Only one third of the original count rate remains for region 3 which leads to a worse statistic. Studying the whole ASM light curve in the right panel of Figure 3.7 yields an *RXTE* ASM flux of 16 cts/s during the *XMM-Newton* observation which is in the same luminosity range as the *BeppoSAX* observations. In addition, a color-color diagram was produced to determine the state of the source. Figure 3.8 shows that also during the *XMM-Newton* observation the source was in the banana state. This result supports the fact that the ASM flux was at the same level and no transition to another state was observed.

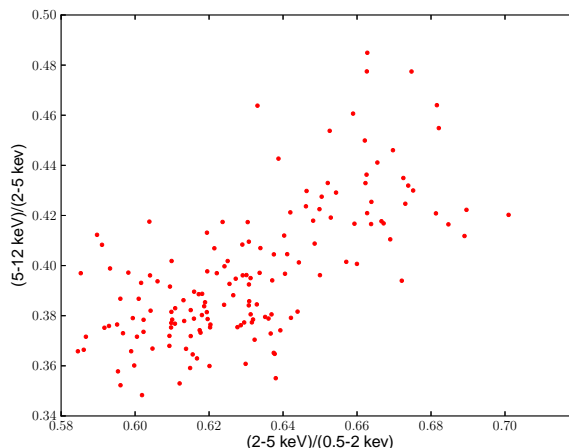


Figure 3.8: Color-color diagram of extraction region 3 of the *XMM-Newton* EPIC-PN data. One point represents 128 seconds of observation.

3.4.3 Spectral analysis

In general, data of the EPIC-PN camera can be used in the energy range of 0.7 keV–10 keV in Timing Mode. However, a broad feature was found at about 1 keV (see also Ng et al. 2010). Furthermore, residuals remained in the Si and Au absorption region around 1.7 keV (D’Ai et al. 2010). Therefore, the energy bins below 2.4 keV were removed (as in Piraino et al. 2012) as well as the bins above 10 keV.

In accordance with the *BeppoSAX* analysis, the EPIC-PN data were also fitted with the model combination of PHABS*(DISKBB + NTHCOMP + REFLIONX). However, the fit gave no satisfying result, since the PN data do not cover such a broad energy range as the *BeppoSAX* data do. Hence, another less complex model was used. The best fit was achieved by using an absorbed combination of a disk blackbody, a single blackbody and a Gaussian line profile. Since the *XMM-Newton* data were not used below 2.4 keV, it is not possible to determine the absorption parameter. Therefore, the value obtained from the *BeppoSAX* analysis was used. To compare the different extraction regions, their spectra and the resulting residuals are shown on the left side of Figure 3.9. Furthermore, the residuals of the continuum fit and the unfolded spectra are shown on the right side. It can be seen that for region 4 the width of the Gaussian line profile is maximal which is emphasized by the best-fit values reported in Table 3.3. The simple Gaussian line model gave acceptable fits for all four extraction regions. Nevertheless, the data were also fitted using a relativistic line model, namely DISKLINE. The reported best-fit values in Table 3.3 show that similar statistical results were obtained in terms of reduced χ^2 , hence, it is not possible to definitively state the relativistic origin of the line. Therefore, the Gaussian model is preferred.

However, the DISKLINE model allows to obtain an estimation of the inner radius

Table 3.3: Best-fit results for the four *XMM-Newton* extraction regions. The spectra were extracted from region 1 (all columns), region 2 (without one column), region 3 (without three columns) and region 4 (without five columns). The absorption was frozen to $0.3 \times 10^{22} \text{ cm}^{-2}$. Also the best-fit results are reported when using the DISKLINE model instead of a Gaussian line profile. Except for region 4 the continuum model parameters do not change.

Parameter	Reg 1	Reg 2	Reg 3	Reg 4
Continuum				
kT_{dbb} [keV]	$1.00^{+0.03}_{-0.03}$	$1.00^{+0.03}_{-0.02}$	$0.98^{+0.04}_{-0.04}$	$0.91^{+0.06}_{-0.05}$
k_{dbb}	147^{+14}_{-16}	157^{+17}_{-16}	172^{+27}_{-25}	211^{+50}_{-45}
kT_{bb} [keV]	$2.04^{+0.03}_{-0.02}$	$2.06^{+0.03}_{-0.03}$	$1.99^{+0.03}_{-0.04}$	$1.85^{+0.04}_{-0.03}$
k_{bb} [10^{-2}]	$5.8^{+0.1}_{-0.1}$	$6.4^{+0.1}_{-0.1}$	$6.3^{+0.1}_{-0.1}$	$5.9^{+0.1}_{-0.2}$
Gaussian				
E_{gau} [keV]	$6.79^{+0.09}_{-0.09}$	$6.82^{+0.09}_{-0.09}$	$6.77^{+0.09}_{-0.10}$	$6.70^{+0.15}_{-0.13}$
σ_{gau} [keV]	$0.39^{+0.19}_{-0.13}$	$0.39^{+0.17}_{-0.12}$	$0.37^{+0.12}_{-0.11}$	$0.43^{+0.26}_{-0.17}$
k_{gau} [10^{-3}]	$1.64^{+0.87}_{-0.54}$	$2.01^{+0.93}_{-0.61}$	$2.38^{+1.05}_{-0.76}$	$2.81^{+2.01}_{-1.15}$
EW [eV]	32.4	36.8	43.2	53.2
χ^2	1528	1503	1421	1401
D.o.f	1512	1512	1512	1485
red. χ^2	1.011	0.994	0.94	0.941
DISKLINE				
E_{disk} [keV]	$6.77^{+0.07}_{-0.07}$	$6.78^{+0.07}_{-0.07}$	$6.72^{+0.09}_{-0.10}$	$6.47^{+0.08}_{-0.13}$
R_{in} [GM/ c^2]	$30.0^{+38.1}_{-16.1}$	$32.9^{+40.0}_{-20.7}$	$44.0^{+52.9}_{-24.0}$	$6.1^{+16.6}_{-0.0}$
Incl [deg]	43^{+16}_{-7}	45^{+19}_{-8}	54 _{fixed}	66^{+0}_{-12}
norm [10^{-3}]	$1.6^{+0.40}_{-0.4}$	$1.9^{+0.2}_{-0.4}$	$2.4^{+0.9}_{-0.8}$	$6.0^{+1.5}_{-2.0}$
χ^2	1528	1503	1422	1401
D.o.f	1511	1511	1512	1484
red. χ^2	1.011	0.995	0.94	0.939

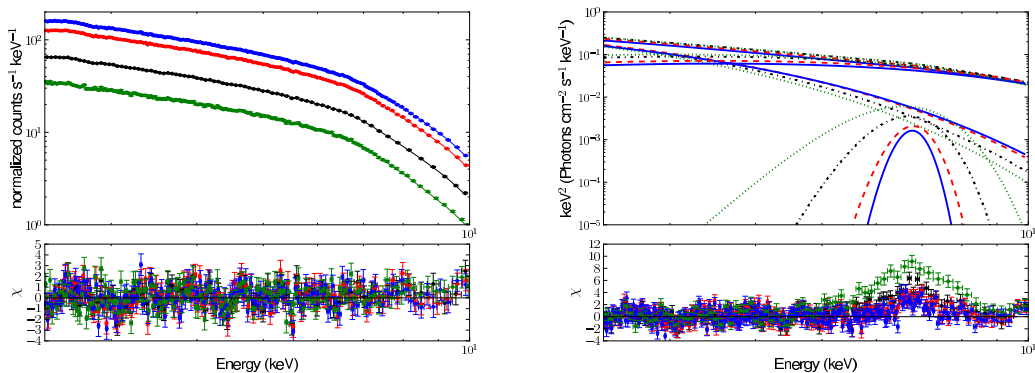


Figure 3.9: *Left panel:* EPIC-PN spectra and residuals of all four extraction regions (region 1 in blue, region 2 in red, region 3 in black and region 4 in green). The used model is $\text{PHABS} \times (\text{DISKBB} + \text{BBODY} + \text{GAUSSIAN})$. *Right panel:* Shown are the unfolded spectra as well as the residuals obtained by using only the continuum model.

of the disk. Disregarding the results for region 4, the inner radius is larger than 15 Schwarzschild radii, which is $R_S = 2 \text{ GM}/c^2$. Due to the poor statistics it was not possible to determine some parameters for region 4, therefore the results are not reliable. This is expected since a significant fraction of the photons are discarded.

3.5 Discussion

The presented *BeppoSAX* and *XMM-Newton* observations both show no significant features in their light curves. Studying the color-color diagrams suggests that during all observations the source was in the banana state of an *atoll source*. Using the *RXTE* ASM light curve also gave no evidence for any significant change of the luminosity or spectral state.

The spectral analysis supports the presence of a multicolor disk blackbody and a Comptonization part which could be modeled either with a Comptonization model or a single blackbody. A corona of hot electrons close to the neutron star in the central region of the accretion disk is most likely the origin of the Comptonization part. Furthermore, the necessity of a model describing the line-like features is emphasized. The broad energy spectrum of *BeppoSAX* allows the use of a reflection model which can account for all prominent features in the continuum fit. The most prominent feature was located around 6.7 keV and can be interpreted as an iron K_α fluorescence line. No relativistic blurring of the line was necessary which indicates that the production of the observed line does not take place close to the neutron star. The normalization of the disk blackbody model was used to estimate the inner radius of the disk. There is a discrepancy between the apparent and real

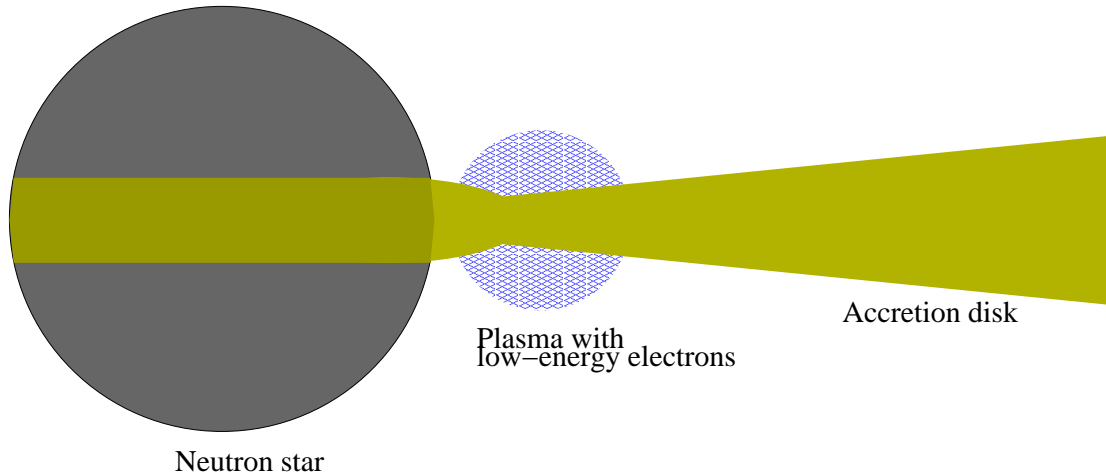


Figure 3.10: Shown is a possible geometry of 4U 1735–44. The model is based on Sakurai et al. (2012) and Matsuoka & Asai (2013).

inner disk radius. A correction has to be applied to calculate the real inner radius which takes into account the relativistic effects at the inner boundary. The real radius is further out and can be calculated using the hardening factor κ (equal to 1.7, Shimura & Takahara 1995) and the correction for inner boundary conditions ξ (equal to 0.412, Kubota et al. 1998). Furthermore, the inclination of the system has to be known. Casares et al. (2006) gave an upper limit of 60° which is not ruled out by the results obtained using the DISKLINE model for the *XMM-Newton* data or the timing properties. Taking this into account, an inner radius of 18 to 23 km can be calculated for the *BeppoSAX* results. Assuming a mass of the neutron star of $1.4 M_\odot$ the inner radius is, in units of the Schwarzschild radius, $R_{\text{in}} \sim 4 R_S - 6 R_S$. However, a typical radius of a neutron star (as it is given by e.g. Lattimer & Prakash 2007) is between 10 km and 15 km. Therefore, the results indicate that the accretion disk approaches close to the surface of the neutron star. Otherwise, for a more massive neutron star of, for example, $2 M_\odot$, the Schwarzschild radius would be 5.9 km and the Innermost Stable Circular Orbit (ISCO) would be 18 km, hence, the accretion disk reaches down to the innermost allowed radius.

The focus was set onto the effects caused by pile-up in the analysis of the *XMM-Newton* data. Extracting spectra from four different regions gave no evidence for a significant change of the line profile. On the contrary, the Gaussian line profile is broadest ($\sigma = 0.43$ keV) when the absence of pile-up is guaranteed by excluding the five innermost columns. Furthermore, the radius of the production site of the iron K_α fluorescence line was determined to be more than $15 R_S$ which supports the assumption that the observed line does not have its origin close to the neutron star.

A possible geometry of the system is based on the model by Sakurai et al. (2012) and Matsuoka & Asai (2013) which is illustrated in Figure 3.10. A plasma com-

posed of low-energy electrons is placed close to the neutron star. Comptonization can take place in this region. The seed photons have their origin in the equatorial regions of the neutron star where a blackbody spectrum is emitted as well as in the inner parts of the accretion disk. Since the inclination angle is large, the blackbody originating from the neutron star surface cannot be observed due to the region of plasma close to the neutron star. Furthermore, the plasma covers the inner parts of the accretion disk which explains the radius of the production site of the fluorescence line. Finally, the multicolor disk blackbody can be observed without any restrictions. Although the model is based on the eastern model, some ideas of the Birmingham model are also included. The hot plasma is similar to the Accretion Disk Corona (ADC) shown in Figure 2.7, though the hot plasma region has a smaller size. Altogether, the findings which lead to the possible geometry provide a connection between the two main models to describe the spectral behavior of low-mass X-ray binary systems.

CHAPTER 4

PILE-UP SIMULATIONS

In the previous Chapter it was shown that the correct treatment of observations, which suffer pile-up, is essential for a meaningful analysis of bright astrophysical sources. The impact of pile-up on the *XMM-Newton* spectra can vary and is still not fully understood. Furthermore, the current tools to check for pile-up do not deliver unique results and therefore the determination if pile-up is present is not clear.

Another way to determine the degree of pile-up as well as to investigate the impact on spectral parameters is provided by simulations. In the following Chapter first pile-up and the problems caused by it will be introduced. Furthermore, the used simulation package will be described and finally the results which were obtained by the simulations will be discussed.

4.1 Motivation

In Section 1.1 the various read-out modes for the EPIC-PN detector aboard *XMM-Newton* were described. They were developed to account for different count rates and fluxes of the observed sources. However, at high count rates even the read-out modes with the highest time resolutions are not sufficient to handle the amount of photons. A second photon can hit the same (energy pile-up) or an adjacent pixel (pattern pile-up) already hit by a first photon within the same read-out cycle. Both scenarios are illustrated in Figure 4.1. As a consequence of pile-up, the flux of the source is not correctly determined, since the event signal seems to be due to one photon, although two photons were collected. Moreover, an event can be rendered invalid by exceeding the upper energy threshold of the detector when summing up the energies of two photons. Similarly, an invalid pattern can be produced and the event will not be processed.

Further effects influences not only the determination of the flux but also the spectral analysis. If pile-up is present, the spectrum gets harder, which means flatter, at the high energy end of the spectrum since one high energy photon is er-

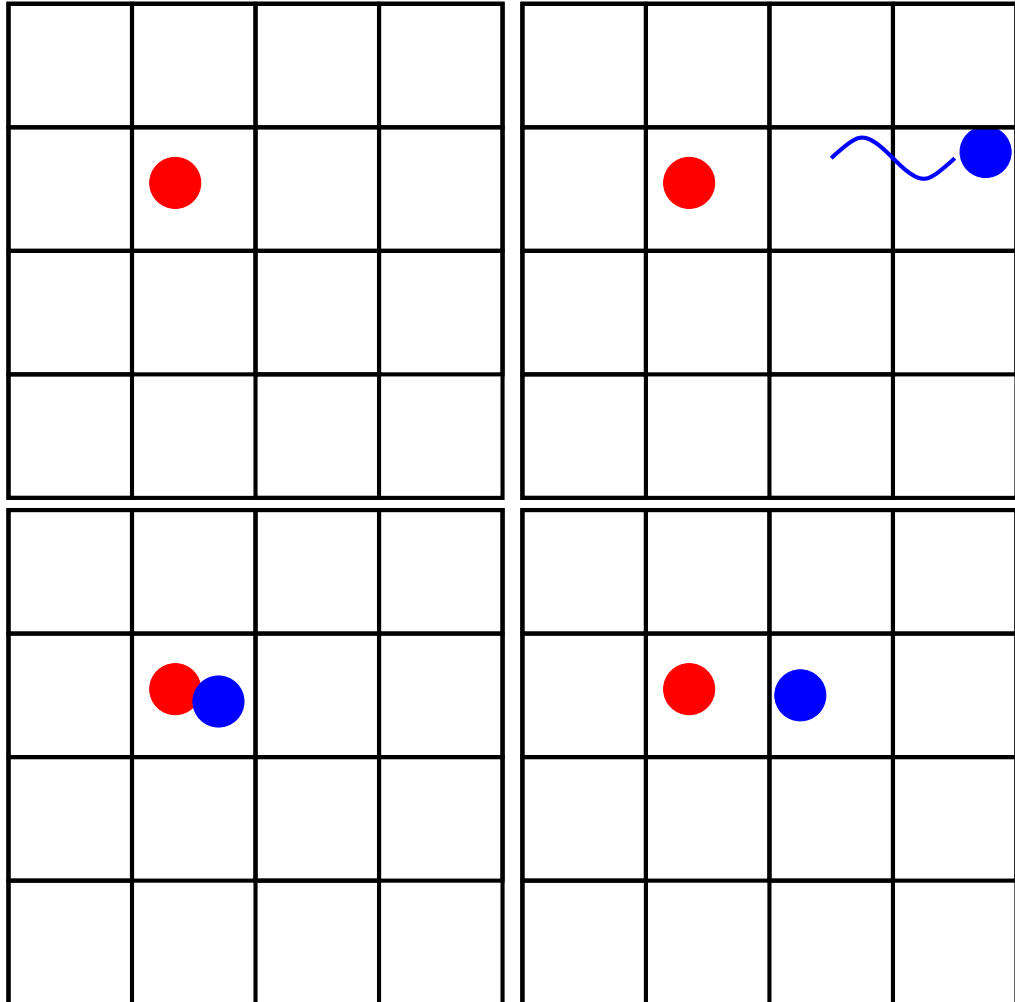


Figure 4.1: Illustration of pile-up in a CCD. *First panel:* One pixel is hit by a photon with energy E_1 and would be detected as a single event with energy E_1 . *Second panel:* An additional photon arrives with energy E_2 . *Third panel:* The second photon hits the same pixel as the first photon. The event will be detected as a single event with energy $E_3=E_1+E_2$ what is called energy pile-up. *Fourth panel:* The second photon hits a neighbouring pixel. It seems that one photon with energy $E_3=E_1+E_2$ creates a double event. This kind of pile-up is called pattern pile-up.

ronously detected instead of two low energy photons. For the EPIC-PN this effect is most prominent, depending on the degree of pile-up, around 10 keV. Although this effect on the general shape of the spectrum is well-known, it is still under discussion if pile-up has also an impact on the most prominent spectral feature in a low-mass X-ray binary system, the iron K_{α} fluorescence line at 6.4 keV (see Section 2.3.1). Since the correct modelling of this line feature is essential for the understanding of the nature of the source, the focus of the simulation performed within the framework of this thesis is set on the investigation of the effects of pile-up on the iron line.

The standard way to obtain an estimation of the degree of pile-up is to compare the pattern fractions in the observation and the expected ones. In the SAS analysis package this comparison is implemented in the EPATPLOT tool, shown in Figure 3.6 of the previous Chapter. A deviation of the observed double event fraction from the model plot is an evidence of pile-up. However, sometimes the plots of the observed fraction and the expected one are close-by and no objective criterion is defined if pile-up is present.

A detailed study of the impact of pile-up on the spectral shape of LMXB systems was performed by Ng et al. (2010). The authors analysed a sample of 16 systems with neutron stars and focusing on the shape of the iron K_{α} line. Taking pile-up effects into account and following the suggestions of the Science Data Center (SDC) by removing the inner parts of the PSF (for the Timing Mode the central columns), they stated that in their sample any asymmetry of the iron line is caused by pile-up. Therefore, the iron line features in the spectra could be described well by a GAUSSIAN line model with no need for a relativistic line model.

In contradiction, Miller et al. (2010) found that the shape of the line is robust within pile-up conditions for different telescopes and modes, including the *XMM-Newton* Timing Mode. Furthermore, the line tends to get narrower when pile-up gets stronger. In summary, the influence of pile-up on the spectral shape is still to be investigated.

4.2 Simulation of pile-up for the EPIC-PN

Miller et al. (2010) limited their simulations to the use of the XSPEC package. The instrument is only characterized by the redistribution matrix file (RMF) and the ancillary response file (ARF). In this work a different approach is chosen. The SIMulation of X-ray TELEscopes (SIXTE, Schmid et al. 2010) package¹ is used. It provides the implementation of the complete photon track starting from the astrophysical source, along the path through the optics and the complete detection and read-out mechanisms. This method allows to check if pile-up is present or not

¹SIXTE was developed during the PhD thesis of Christian Schmid at the Karl-Remeis Sternwarte Bamberg of the University of Erlangen-Nuremberg, http://www.sternwarte.uni-erlangen.de/new/Arbeiten/2012-07_Schmid.pdf

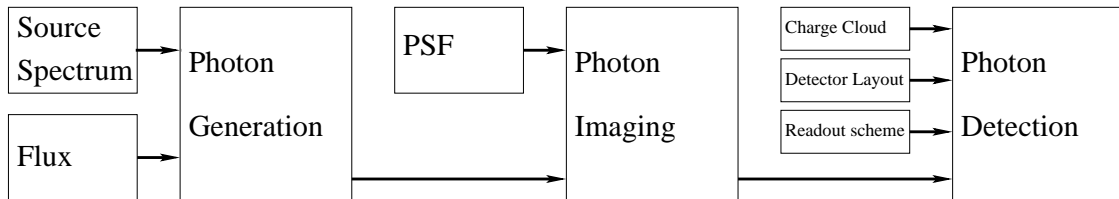


Figure 4.2: Illustration of the simulation setup, showing the various simulation steps.

without being dependent on theoretical models.

In the following, the basics of the simulation package and the setup are described. Furthermore, the required input files which are necessary to perform a proper simulation will be given.

4.2.1 The SIXTE simulation package

The intention of the SIXTE simulation package is to provide a generic simulation environment for all kind of X-ray telescopes. The package is capable to perform simulations for both forthcoming missions, like *eROSITA* on the Spektrum Röntgen-Gamma satellite or *ATHENA* and for current observatories like *XMM-Newton*.

This flexibility is achieved by a modular organisation of the simulation. The setup is divided into three individual parts which are illustrated in Figure 4.2 and will be described in detail in the following.

Photon Generation

First of all, the amount of photons which originates from the astrophysical source and their corresponding energy has to be defined. The properties of the sample are based on a given spectral model which characterizes the source of interest and the timing properties which can be given by a power spectrum, a pulse period or just a flux from which the arrival times are calculated.

These source informations have to be given in a specifically developed format which is called SIMPUT, described by Schmid et al. (2010). If desired, a source catalogue can be given and the software identifies the sources which are in the field of view of the current pointing of the telescope. This option is especially used for surveys and observations in imaging modes for which several sources fall into the field of view. However, for EPIC-PN observations in Timing Mode the field of view is restricted to one twelfth of the whole camera and only pointed observations are taken into account, so it is sufficient to provide a single source.

If all necessary informations are given, the resulting count rate which is registered on the detector can be determined using the source flux and the effective

area of the detector. To get the number of photons in each energy bin, the flux density has to be multiplied with the size of the bins which are stored in the ARF. Furthermore a randomization is performed to get realistic energy values.

However, it is not enough to produce a realistic energy distribution, especially when pile-up is important. Also a realistic arrival time distribution has to be ensured. The average photon rate R is calculated using the given flux in a reference energy band in the input SIMPUT file and the ARF of the instrument. Schmid et al. (2010) use the probability density given in Knoll (2010) to determine the time intervals Δt between two photons:

$$k(\Delta t)d(\Delta t) = \frac{(R \cdot \Delta t)^0 e^{-R \cdot \Delta t}}{0!} \cdot R d(\Delta t) = R \cdot e^{-R \cdot \Delta t} d(\Delta t) \quad (4.1)$$

which leads to the probability distribution

$$K(\Delta t) = \int_0^{\infty} k(\Delta t)d(\Delta t) = 1 - e^{-R\Delta t} \quad (4.2)$$

and finally the time intervals between two photons can be determined using the inversion method (e.g. Gould et al. 2006) as:

$$(\Delta t)_i = -\frac{1}{R} \ln(u_i) \quad (4.3)$$

with u_i as a random number in the interval of $[0,1)$.

An energy value and an arrival time is assigned to all produced photons and finally a standard OGIP FITS format (Arnaud K.A. 2009) conform photon list is created in which these values as well as the place of origin in equatorial coordinates are stored.

Photon Imaging

The previously produced photon list is given as input to the Photon Imaging which reproduces the path of each photon through the telescope. To obtain a simulated image close to what is really observed, the vignetting function and the Point Spread Function (PSF) of the telescope are necessary. The vignetting accounts for the fact that photons depending on their energy and especially their off-axis angle are just reflected with a certain probability. In particular, this effect has to be taken into account for survey missions or for imaging with a large field of view.

The PSF, on the other hand, describes the reproduction of a point source by the mirrors. In general, the exact profile of the PSF depends on the energy and the off-axis angle. As input for the simulations a 2-dimensional image of the PSF is necessary, which is centered on the ideal impact position. To include the displacement from the ideal position Schmid et al. (2010) uses a deviation from the obtained value:

$$\begin{aligned} x' &= x + \Delta x \\ y' &= y + \Delta y \end{aligned} \quad (4.4)$$

Since within the simulation the PSF is converted to a 2-dimensional probability function, a randomization process can be performed which leads to a realistic value of the impact point.

The generated impact list is basically the original photon list, however, to every photon a specific impact point is assigned.

Photon detection

Finally, the photons hit the detector with a well-defined energy, arrival time and position. However, it is not possible to measure these values with infinite precision. Several effects take place during the detection process and the read-out. At first, the geometry of the pixels has to be known, especially, the pixel size and the alignment of the whole CCD chip. Furthermore, the response matrix is required, which gives the probability of a photon with a certain energy to be detected in a given energy bin. Also detector specific features like bad pixels and other detector defects can be used to design a more realistic simulation. Another important point is to reproduce the read-out process (see Section 1.3.3) correctly. Therefore, the times which are necessary to shift the accumulated charge to the border of the CCD, where the read-out chip is placed, as well as the time to read-out the pixels have to be known and implemented.

Since the comparison of the expected pattern fractions with the measured ones is the standard way to check for pile-up, the reproducing of the charge cloud (see Section 1.1.3) is essential for pile-up simulations.

In addition to the already implemented charge cloud models in the SIXTE software package, another model was implemented in the course of this thesis, as a simple Gaussian profile was not sufficient to characterize the pattern fractions. Therefore, an asymmetric energy-dependent model was implemented based on the results reported by Kimmel et al. (2006). The asymmetry is a result of the mounted read-out electronics which produces an electric field that influences the charge cloud. Taking this into account the model was implemented in the following way:

$$\begin{aligned} X &= X_0 + p_1 \cdot E^{p_2} \\ Y &= Y_0 + p_1 \cdot E^{p_2} \end{aligned} \tag{4.5}$$

with X and Y the size of the charge cloud in the horizontal and vertical direction, X_0 , Y_0 , p_1 and p_2 as parameters which reproduces the size depending on the energy E of the detected photon.

Finally, after the read-out process is performed, an event list as well as a recombined pattern list is produced in the standard OGIP FITS format. The analysis of these lists can be performed using the standard tools, e.g. for *XMM-Newton* data the SAS analysis package. However, the exact pile-up fraction is known, since every photon track can be reconstructed and every recombined pattern can be checked if it is caused by a single photon or by pattern pile-up.

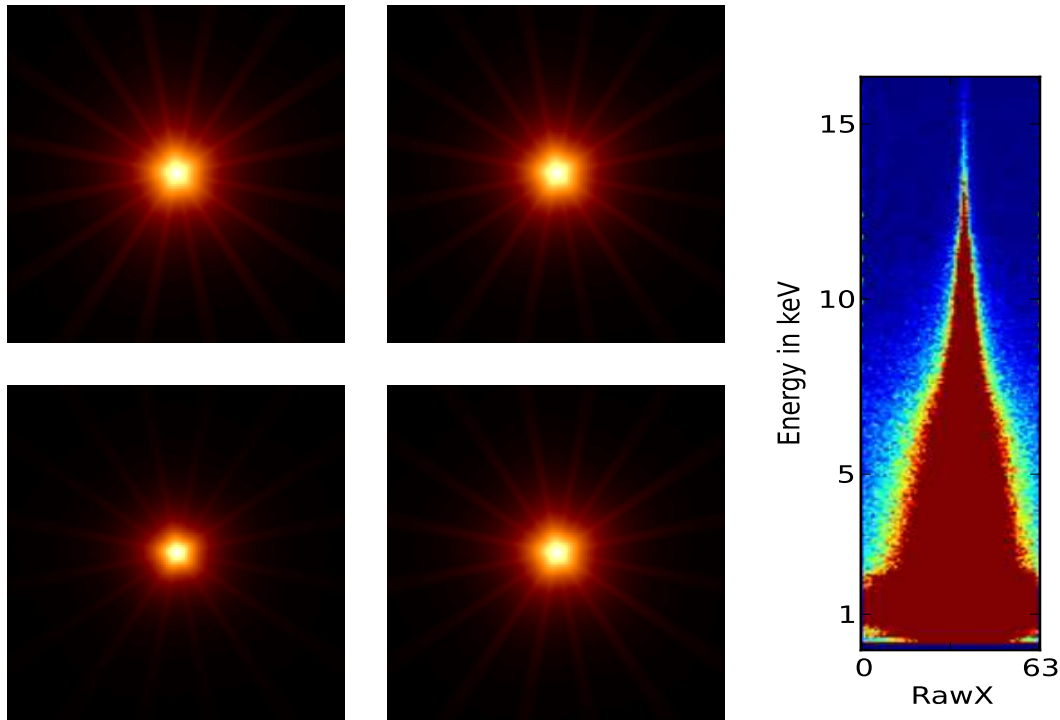


Figure 4.3: *Left side:* PSF at different energies produced with ELLBETA. Clockwise there are: *First panel:* PSF at an energy of 0.2 keV. *Second panel:* PSF at an energy of 1.0 keV *Third panel:* PSF at an energy of 5.0 keV *Fourth panel:* PSF at an energy of 10.0 keV. *Right side:* Shown is the contribution of each energy in every Raw X column which is directly related to the width of the PSF. As example the observation of 4U 1735–44 (reported in Chapter 3) is shown.

4.2.2 Simulation Inputs

To offer a generic simulation tool for several kind of detectors, the mission specific parameters are not hard-coded but are given in a XML format. This allows to check easily different settings for the simulations. In the following the input files and parameters which are required to perform a simulation will be described.

Point Spread Function

As mentioned before the PSF characterizes the imaging capabilities of a telescope. Since the PSF is energy dependent, PSFs were produced using the SAS tool ELLBETA for different energies, namely 0.2 keV, 0.5 keV and in 1 keV steps from 1 keV up to 15 keV (examples are shown in Figure 4.3). The images show that for higher energies the PSF is narrower. An alternative representation is given on the right hand of Figure 4.3 in which the pulse invariant (PI) energy is plotted over the RawX coordinate of the detector. The contribution of each energy in each detec-

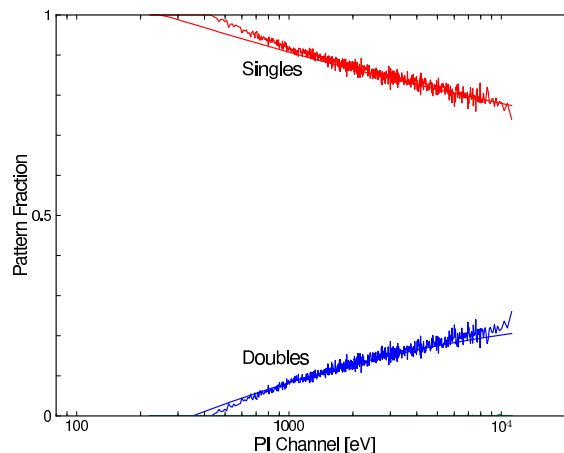


Figure 4.4: The EPATPLOT to adjust the parameters of the charge cloud model. The solid lines represent the model given in the current calibration files.

tor column is illustrated. A horizontal line would indicate a uniformly distributed energy which is expected from detector lines. However, the contribution from the source should center around the ideal impact position in the middle of the detector. As it can be seen, the photons at low energies are distributed over a huge column range whereas at high energies the majority of the photons are concentrated in a few columns around the focal point.

Charge Cloud

As described above, the modeling of the charge cloud is important to reproduce the right splitting behaviour of the detector. However, the newly implemented charge cloud model has to be adjusted to the given detector. Therefore, a simulation with a low flux ($5 \times 10^{-10} \text{ ergs s}^{-1} \text{ cm}^{-2}$) was performed to assure that no pile-up is present. The parameters were varied to match the model given in the Current Calibration Files (CCFs) which is represented in the EPATPLOT shown in Figure 4.4. In Table 4.1 the used input parameters for the charge cloud model are reported. To verify that the parameters are not dependent on the spectral model, a variety of models were used in a test run which gave no evidence for a dependence.

Detector Parameters

Also the geometrical layout of the detector must be modelled. Since in the Timing Mode only one CCD is working, the detector is given as 64×200 pixels with a size of $150 \mu\text{m} \times 150 \mu\text{m}$. The event threshold is set to 200 eV whereas however, also events with lower energies are read out but not recombined to valid events. Furthermore, the read-out scheme is also implemented in the XML file. At first, ten lines are

Table 4.1: Input parameters for the charge cloud model.

Parameter	Variable	Value
Horizontal start value	X_0	$7.2 \mu\text{m}$
Vertical start value	Y_0	$6.9 \mu\text{m}$
Step width	p_1	$0.1 \mu\text{m}$
Energy dependence	p_2	0.5

read out with each lineshift lasting $0.72 \mu\text{s}$. After the completion of one macro pixel, a wait time of $22.3 \mu\text{s}$ is set to account for the read-out time. In this way, the time resolution of $29.5 \mu\text{s}$ is reproduced. Other necessary inputs are the RMF as well as the ARF which were created using the RMFGEN, respectively ARFGEN tool included in the SAS package in version 10.0. In this work, the simulations were performed using the thin filter parameters of the EPIC-PN.

Flux and Model

The previously defined input parameters are all related to the observation and detection methods. However, the observed astrophysical source has to be also defined. The observed flux is related to the luminosity of the source. Since pile-up should be studied, the input parameters of the flux vary between $5.0 \times 10^{-10} \text{ ergs cm}^{-2} \text{ s}^{-1}$ and $1.0 \times 10^{-8} \text{ ergs cm}^{-2} \text{ s}^{-1}$ in the energy range of 0.2 keV–15 keV. Using the effective area the count rate results in a range from well below 100 cts/s up to above 1000 cts/s.

In addition to that, the spectral shape has to be defined. The spectral information stored in the SIMPUT file is based on the models implemented in XSPEC. Some of the standard models have been introduced in 3.2. The results of the *XMM-Newton* analysis reported in Mück et al. (2013) and in Chapter 3 are used as a reference point for a set of generic simulations. A combination of an absorbed single blackbody and a multicolor disk blackbody is given as input with the input values reported in Table 4.2. In addition to the continuum, different characterizations of the iron line feature are used. The line is first modeled by a GAUSSIAN line profile whereas the width is varied to account for different, realistic source conditions. In another set of simulations, the line was characterized by an asymmetric, relativistically broadened line profile using the DISKLINE model.

A summary of all input line models is given in Table 4.2. In Sim1 a Gaussian is simulated with a width which is comparable to the spectral resolution of the detector. Furthermore, Sim2 reproduces the line which was found by Mück et al. (2013) in 4U 1735–44. The broadest line profile is based on results reported by Cackett et al. (2012) who has found a Gaussian with a width of about 1.0 keV. Finally, a relativistic line is simulated in an extreme case with an inner radius of the accretion disk of six gravitational radii which is the closest radius theoretically

Table 4.2: Input model for the simulations.

Parameter	Continuum for all setups			
phabs[$10^{22}/\text{cm}^2$]	0.3			
T _{Dbb} [keV]	1.00			
norm _{Dbb}	200			
kT[keV]	2.00			
norm _{bb} [10^{-2}]	7.00			
Parameter	Narrow Sim1	Normal Sim2	Broad Sim3	Relativistic Sim4
E _{Gau} [keV]	6.75	6.75	6.75	
σ_{Gau} [keV]	0.10	0.40	1.00	
norm _{Gau} [10^{-2}]	0.50	0.50	5.00	
E _{Disk} [keV]				6.70
R _{in} [GM/c ²]				6.00
R _{out} [GM/c ²]				1000
Incl [deg]				30.0
norm _{Disk} [10^{-2}]				1.00
Betor				-2.4

allowed (as shown in Section 2.2.2).

4.3 Results of generic simulations

After simulations were performed for 22 different fluxes, it was possible to define three regimes: no pile-up (Regime 1), modest pile-up (Regime 2) and extreme pile-up (Regime 3). A flux of $1.0 \times 10^{-9} \text{ ergs cm}^{-2} \text{ s}^{-1}$ was chosen for Regime 1, which results in a count rate of 172 cts/s. Regime 2 corresponds to a flux of $4.5 \times 10^{-9} \text{ ergs cm}^{-2} \text{ s}^{-1}$ for a count rate of 779 cts/s. Finally, for Regime 3 the highest simulated flux ($1.0 \times 10^{-8} \text{ ergs cm}^{-2} \text{ s}^{-1}$) was chosen, which leads to a count rate of 1716 cts/s. The data was extracted using the standard *XMM-Newton* analysis tools included in the SAS package. A spectrum was obtained following the standard way by extracting it from a 15 columns wide box around the focal point. Checking for pile-up was performed using the EPATPLOT tool and if pile-up was present, the innermost columns were excluded from the extraction until no pile-up was present anymore. To ensure an unbiased analysis, the fitting was performed using XSPEC in the same way as in the case of a *real* observation: different continuum and line models were tried in the fit.

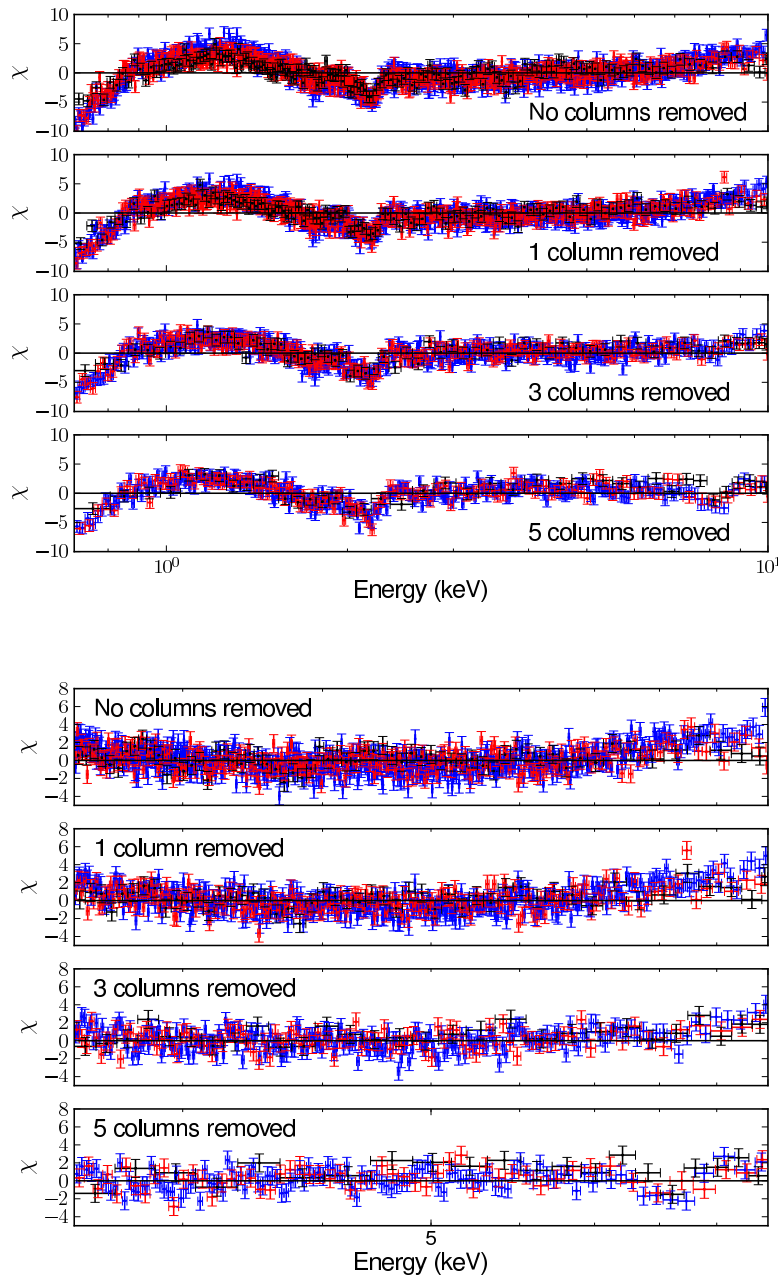


Figure 4.5: *Upper panel:* Residuals obtained by fitting the simulated continuum spectra using the complete energy range from 0.5 keV–10 keV. The spectra were extracted from a 15 columns wide box around the focal point with excluding columns of the center to deal with pile-up. *Lower panel:* Residuals obtained by fixing the fit parameters to the input values. In both plots Regime 1 is given in black, Regime 2 in red and Regime 3 in blue.

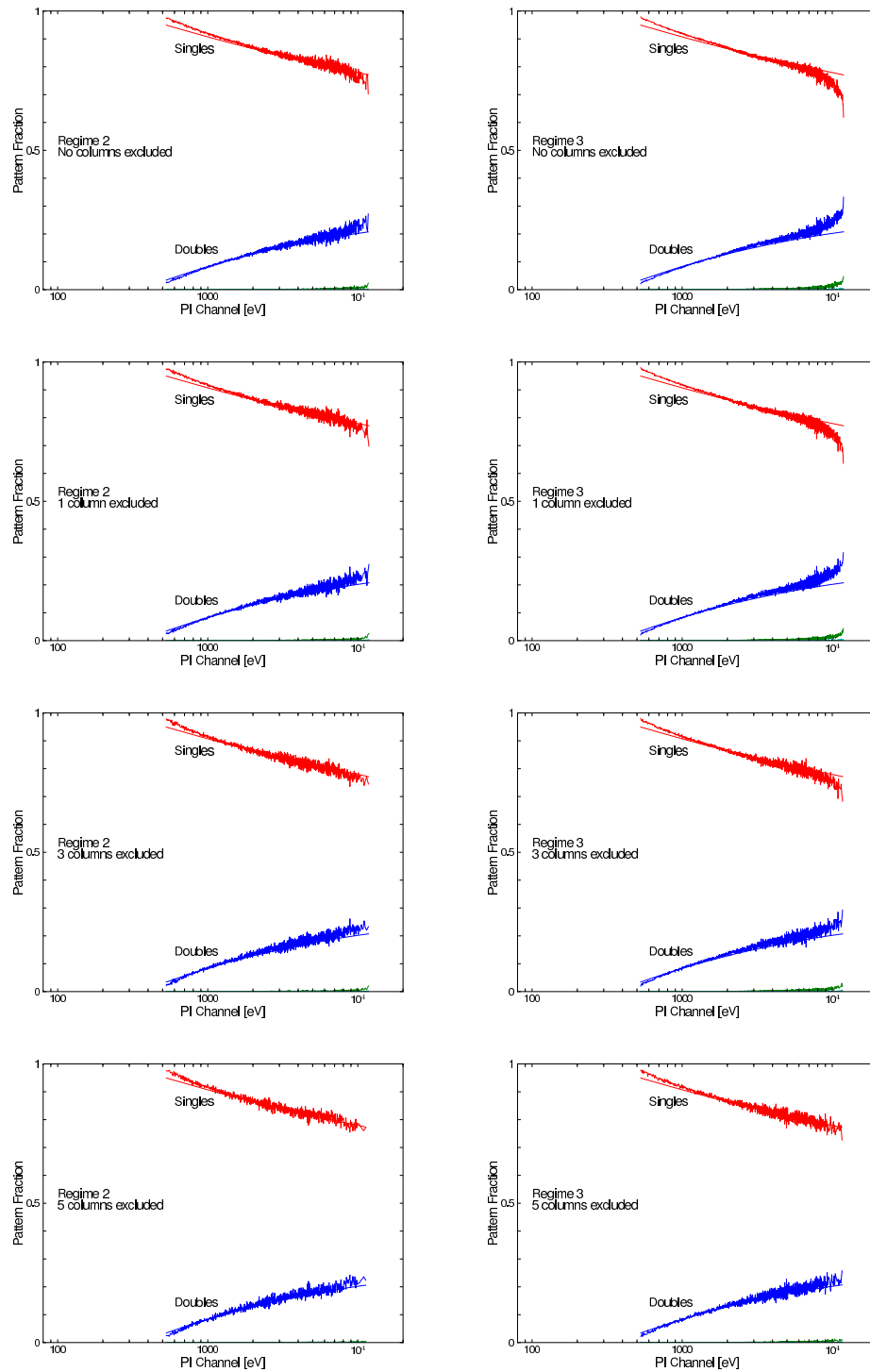


Figure 4.6: *Left side:* Epatplots for different extraction regions for Regime 2. *Right side:* Epatplots for different extraction regions for Regime 3.

4.3.1 Continuum

Before studying the effect of pile-up on the shape of the line feature, the modifications on the spectral continuum, as given in Table 4.2, caused by pile-up have to be understood. The simulated *observed* spectrum was fitted using the standard continuum model $\text{PHABS} \times (\text{DISKBB} + \text{BBODY})$. Residuals of the fit are shown on the upper panel of Figure 4.5. Other continuum models, like COMPTT to account for comptonization, gave no satisfying results. As it can be seen, systematic residuals caused by Si and Au absorption appear around 2 keV. These systematic effects have been discussed by Piraino et al. (2012), D’Aì et al. (2010) and Mück et al. (2013). Since the results should be comparable to Mück et al. (2013), only data in the 2.4 keV–10 keV range will be used to avoid effects in the spectral fitting in the following.

A benefit of the simulation is the knowledge of the original spectral model and therefore it is possible to compare the original with the simulated spectrum. The parameter values were fixed to the input values which results in the residuals shown on the lower panel of Figure 4.5. As expected from piled-up observations, the spectra become harder for higher count rates which manifests itself in the excess above 8 keV especially for Regime 3 shown in blue. A slight steepening of the spectrum can be also seen in Regime 2 (red) when no columns are excluded. Looking at the results of the EPATPLOT tool, shown in Figure 4.6, shows a clear evidence for pile-up in Regime 2 and Regime 3. Following the usual instructions for piled-up observations, the innermost column was removed. The resulting residuals are shown in the second subpanel on the lower panel of Figure 4.5.

Running the EPATPLOT tool again yields to the conclusion that in the extreme case the observation still suffer pile-up and therefore additional columns have to be excluded from the extraction whereas five columns were necessary to provide a pile-up free observation. However, for Regime 2 the result of the EPATPLOT is not clear. Therefore, the recording of every photon is used, which allows to calculate the real pile-up fraction of an observation. The pile-up fraction is 2.8% in the energy range of 9 keV–10 keV. No significant distortion due to pile-up is expected from such a fraction. Moreover, the study has shown that for a pile-up fraction of below 3% no pile-up effects can be observed.

For comparison, for all three regimes the fits from the different extraction regions are presented in Figure 4.5 for the continuum simulation.

Furthermore, the fit was performed without fixing the temperatures, as it would be done in an analysis of a real observation. Since it is not possible to obtain a reasonable value for the absorption when the energy range below 2.4 keV is excluded, this parameter is fixed. The resulting best fit values as well as the corresponding errors are reported in Table 4.3. These results emphasize the findings of the residual plots. For Regime 2 and especially for Regime 3 the temperature of the blackbody (BBODY) is higher than the input value. This effect is expected to account for the harder spectrum.

Furthermore, it can be stated that for all regimes and extraction regions rea-

Table 4.3: Best-fit parameters of a pure continuum simulation for region 1 (no columns excluded), region 2 (one column excluded), region 3 (three columns excluded) and region 4 (five columns excluded) for the simulation input model PHABS*(DISKBB + BBODY).

Parameter	Region 1	Region 2	Region 3	Region 4
$1 \cdot 10^{-9} \text{ erg s}^{-1} \text{ cm}^{-2}$ – Regime 1				
$T_{\text{Dbb}}[\text{keV}]$	$0.98^{+0.03}_{-0.03}$	$0.97^{+0.04}_{-0.03}$	$1.00^{+0.06}_{-0.05}$	$0.96^{+0.08}_{-0.07}$
norm_{Dbb}	$25.7^{+3.3}_{-2.8}$	$26.8^{+3.9}_{-3.5}$	$24.4^{+5.3}_{-4.5}$	$28.3^{+9.4}_{-7.2}$
$kT[\text{keV}]$	$1.99^{+0.03}_{-0.04}$	$1.99^{+0.04}_{-0.05}$	$1.99^{+0.06}_{-0.05}$	$1.90^{+0.08}_{-0.06}$
$\text{norm}_{\text{bb}}[10^{-2}]$	$0.76^{+0.01}_{-0.01}$	$0.80^{+0.01}_{-0.01}$	$0.79^{+0.01}_{-0.01}$	$0.81^{+0.02}_{-0.03}$
red. χ^2 (1515 dof)	1.0206	1.0314	0.9978	1.0146
$4.5 \cdot 10^{-9} \text{ erg s}^{-1} \text{ cm}^{-2}$ – Regime 2				
$T_{\text{Dbb}}[\text{keV}]$	$0.99^{+0.01}_{-0.02}$	$0.97^{+0.02}_{-0.01}$	$1.00^{+0.03}_{-0.03}$	$0.98^{+0.03}_{-0.03}$
norm_{Dbb}	$111.7^{+6.3}_{-6.0}$	$120.5^{+7.9}_{-7.5}$	$109.1^{+10.7}_{-9.9}$	$120.5^{+17.4}_{-15.4}$
$kT[\text{keV}]$	$2.02^{+0.01}_{-0.02}$	$2.01^{+0.02}_{-0.02}$	$2.01^{+0.03}_{-0.03}$	$1.96^{+0.04}_{-0.04}$
$\text{norm}_{\text{bb}}[10^{-2}]$	$3.46^{+0.02}_{-0.01}$	$3.64^{+0.02}_{-0.01}$	$3.63^{+0.03}_{-0.03}$	$3.73^{+0.04}_{-0.05}$
red. χ^2 (1515 dof)	0.9791	1.0197	1.0279	1.1036
$1 \cdot 10^{-8} \text{ erg s}^{-1} \text{ cm}^{-2}$ – Regime 3				
$T_{\text{Dbb}}[\text{keV}]$	$0.99^{+0.01}_{-0.01}$	$0.99^{+0.01}_{-0.01}$	$0.99^{+0.02}_{-0.02}$	$1.00^{+0.03}_{-0.02}$
norm_{Dbb}	$244.4^{+9.0}_{-8.8}$	$251.4^{+10.9}_{-10.5}$	$251.1^{+16.1}_{-15.2}$	$249.3^{+23.5}_{-21.7}$
$kT[\text{keV}]$	$2.04^{+0.02}_{-0.01}$	$2.05^{+0.01}_{-0.02}$	$2.02^{+0.02}_{-0.02}$	$1.99^{+0.03}_{-0.02}$
$\text{norm}_{\text{bb}}[10^{-2}]$	$7.78^{+0.02}_{-0.02}$	$8.15^{+0.03}_{-0.02}$	$8.15^{+0.04}_{-0.04}$	$8.29^{+0.07}_{-0.07}$
red. χ^2 (1515 dof)	0.9724	1.030	1.0570	1.0459

sonable values close to the input ones and a good fit in terms of reduced χ^2 can be obtained.

4.3.2 Narrow Line - Sim 1

After investigating the effect on the continuum, the impact on a spectrum in which a line feature is included is studied. The input parameters are given in Table 4.2. As before, a standard analysis was performed without fixing any value, except the absorption. First, the spectrum was fitted using the original model. To illustrate the shape of the line the GAUSSIAN model was removed which is shown in Figure 4.7. With higher count rates the shape of the line feature does not change significantly which is emphasized by the best-fit results reported in Table 4.4. The continuum model parameters vary in the same way as found in the pure continuum simulation, the blackbody temperature slightly increases with higher flux.

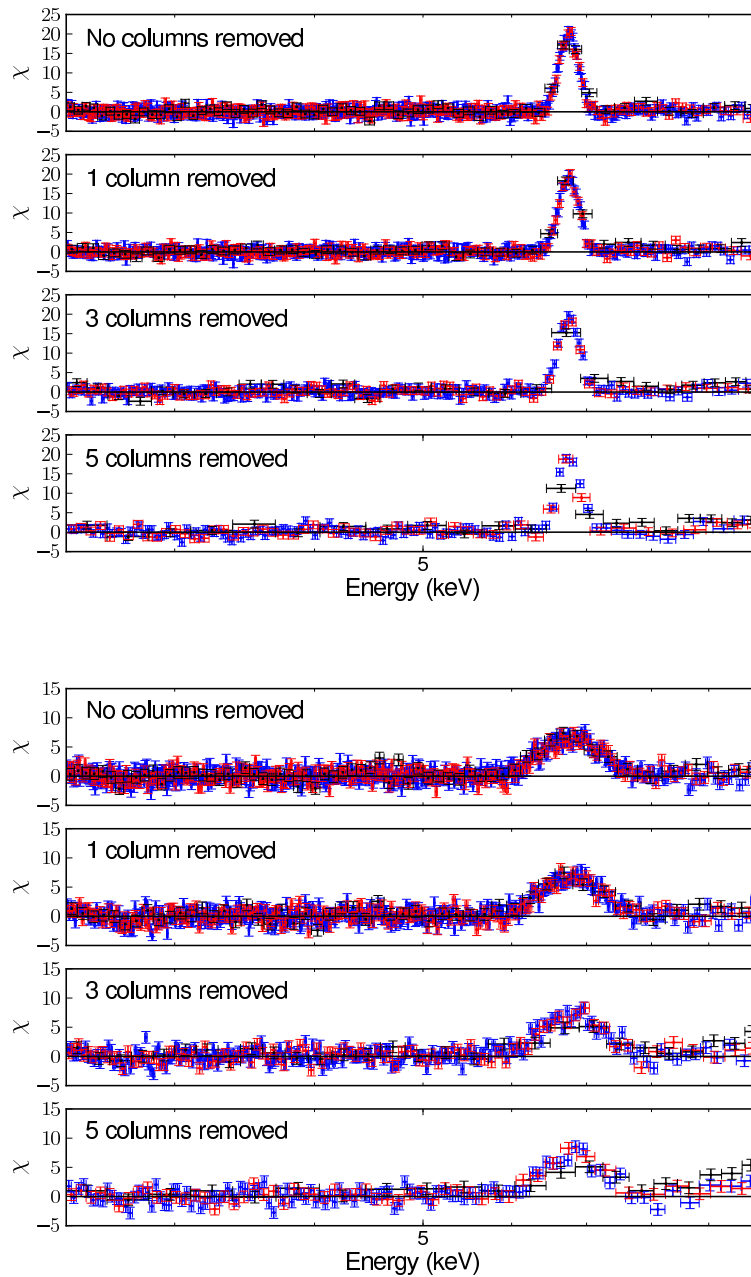


Figure 4.7: *Upper panel:* Residuals obtained by fitting the simulated spectrum with a narrow line included and removing the line model. The spectra were extracted from a 15 columns wide box around the focal point whereas columns are excluded from the extraction to deal with pile-up. *Lower panel:* Residuals of a simulated spectrum with a *normal* line when only the continuum is modeled. In both plots Regime 1 is given in black, Regime 2 in red and Regime 3 in blue.

Furthermore, the fit results support the evidence that the line does not change. In contradiction to that, the width of the line shows a tendency to larger values when columns were excluded for Regime 3. However, within the error margin the GAUSSIAN widths are consistent.

To check if another astrophysical model can reproduce the line feature in a comparable way or even better, the GAUSSIAN was replaced by the DISKLINE model. In consideration of the results given in Table 4.5, it can be stated that the DISKLINE model characterizes the line feature in a comparable way in terms of the reduced χ^2 . However, the production place of the line is at very large inner radii, which should not result in a significant broadening or in an asymmetric shape of the line. For the highest count rate the inner radius is smallest, but still not in a region in which a significant line distortion is expected. Furthermore, it can be stated that the use of a different line model does not effect the continuum.

4.3.3 Normal Line - Sim 2

Afterwards the case of a *normal*² line was investigated (values in Table 4.2) with a GAUSSIAN width of 0.4 keV. Along the lines of the previous study, the spectrum was fitted without putting any restrictions on the blackbody temperatures. In the lower panel of Figure 4.7 the shape of the line is shown for the different fluxes and extraction regions whereas the best-fit values are reported in Table 4.6.

The residuals as well as the parameter values suggest that higher fluxes and therefore pile-up do not modify the shape of the line profile significantly. In the case of the lowest flux the width of the GAUSSIAN decreases when columns are removed. However, these results have to be dealt with caution, because statistics is poor since the removing of five columns results in a count rate of only about 12 cts/s in the used energy range.

Furthermore, also the DISKLINE model reproduced the spectral shape as it can be seen in Table 4.7. For count rates of Regime 2 and Regime 3 the inner radius of the disk tends to lower values when columns are excluded, however, the results are consistent within the error ranges. Compared to the narrow line, the obtained values for the inner radius is smaller and the values for the inclination is larger. A smaller inner radius means that the production place of the line is closer to the neutron star and therefore the line profile is stronger influenced by the relativistic effects which can lead to a broader line.

4.3.4 Broad Line - Sim 3

To account for the broadest lines reported in literature, a broad line was simulated using a width of the GAUSSIAN model of 1 keV. For higher fluxes again a trend to higher blackbody temperatures can be found whereas the shape of the line seems to be not affected by pile-up. On the contrary, for Regime 2 and Regime 3 the

²A *normal* line is defined as a slightly broadened line

width of the line is decreasing when columns are removed which can be seen in the upper panel of Figure 4.8 and in Table 4.8. Hence, the line appears to be narrower as it is.

Furthermore, the DISKLINE model reproduces the spectral shape in an acceptable way as shown in Table 4.9. However, the values obtained for the inclination angle (90°) are not reasonable, since the radiation originating from the inner parts of the disk would be covered by the disk itself and therefore the continuum would be different.

4.3.5 Relativistic Line - Sim 4

In order to compare the results of a non-relativistic origin of the line with a relativistic one, for the last simulation set a relativistic iron line described by the DISKLINE model was chosen for which the input parameters are reported in Table 4.2.

A clear deviation from a simple Gaussian profile can be seen in the residuals which are shown in the lower panel of Figure 4.8. The best-fit values reported in Table 4.10 show the same effect as before: the temperature of the blackbody increases with flux. However, for Regime 1 the temperature of the disk blackbody as well as the temperature of the blackbody are significant lower as the input value. Pile-up and columns exclusion have no effect on the shape of the line, the relativistic profile is reproduced.

Fitting the spectrum with a GAUSSIAN line profile instead of the DISKLINE model results in an equally good fit for Regime 1. The width of the line is about 0.25 keV. In the case of modest and extreme pile-up a comparable fit can be just obtained by excluding columns.

4.4 Results of specific observations

In the previous Section the general impact of pile-up on the spectral shape was studied. Thereafter, simulations were performed with the intention to reproduce published observational results. As basis for the input models, three sources were chosen which have been studied by Ng et al. (2010). As mentioned before, they have reanalyzed observations which have been published before with the focus set on pile-up effects. The sources are Serpens X-1 (Cackett et al. 2010), 4U 1705-44 (di Salvo et al. 2009) and 4U 1636-536 (Pandel et al. 2008). In each of the publications a relativistic origin of the line was stated which were doubted by Ng et al. (2010) and were explained by distortion of the line caused by pile-up.

Therefore, simulations were performed based on both, the models describing the relativistic origin and the model used by Ng et al. (2010). The data extraction was performed according to the corresponding publications. Afterwards, each spectrum was fitted with the input spectrum and the corresponding alternative model and the performances were compared. Hence, it is possible to clarify, if pile-up effects

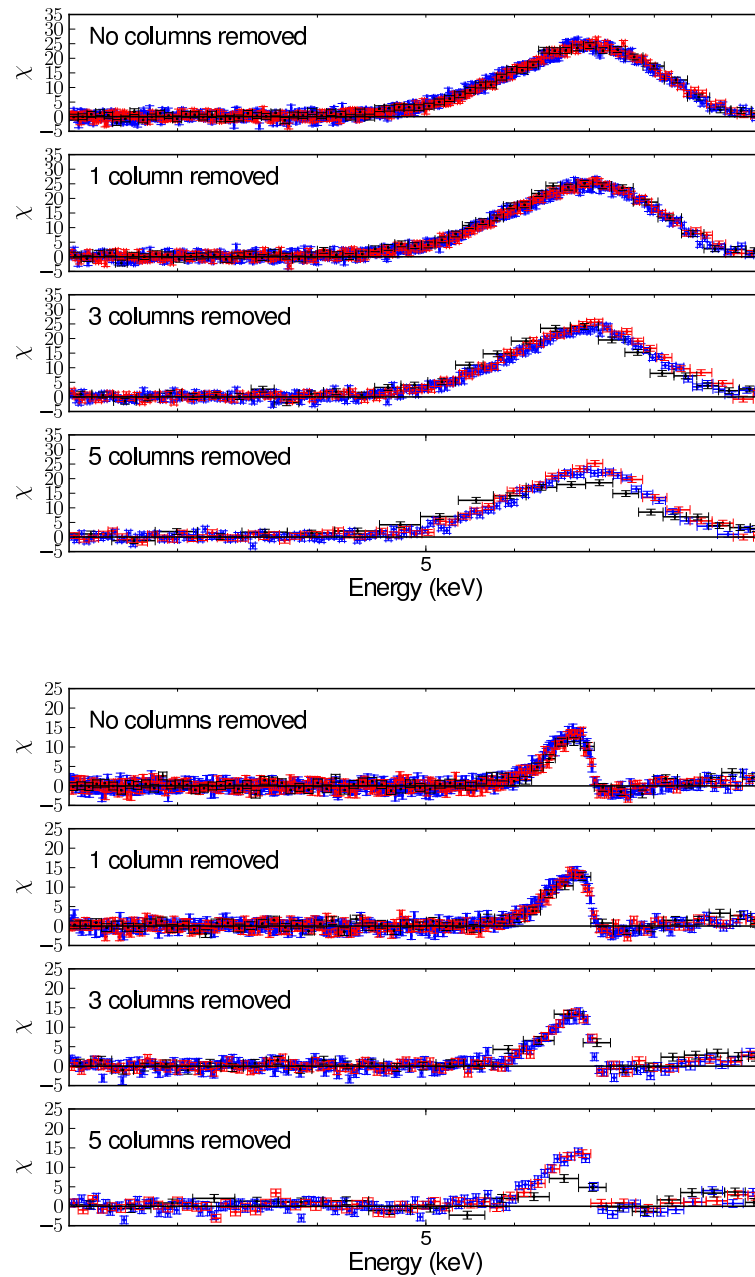


Figure 4.8: *Upper panel:* Residuals obtained by fitting the continuum of a simulated spectrum with a broad line. The spectra were extracted from a 15 columns wide box around the focal point whereas columns are excluded to deal with pile-up. *Lower panel:* Remaining residuals after fitting the continuum of a simulated spectrum with a relativistic line. In both plots Regime 1 is given in black, Regime 2 in red and Regime 3 in blue.

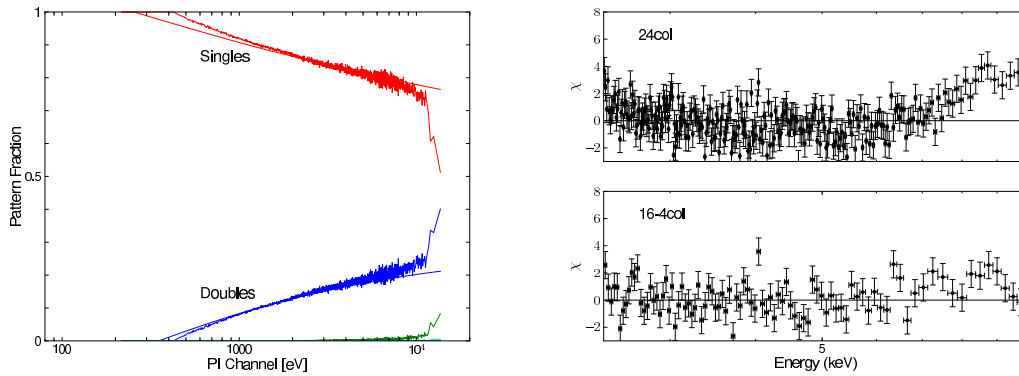


Figure 4.9: *Left side:* Shown is the EPATPLOT of the simulation based on the results reported by Cackett et al. (2010). *Right panel:* Shown are the spectra when the energy is fixed to the input values for the extraction performed in analogy to Cackett et al. (2010) (upper panel) and Ng et al. (2010) (lower panel).

can distort a symmetric, Gaussian line to an asymmetric, relativistic line. On the contrary it is also possible, that a relativistic line appears to be a Gaussian line due to the decrease of counts and therefore worse statistics.

4.4.1 Serpens X-1

In Table 4.12 the models used by Cackett et al. (2010) and Ng et al. (2010), in the following Model 1 and Model 2 respectively, are given to describe the spectral shape of the *XMM-Newton* observation of Serpens X-1 (ID 0084020501).

Cackett et al. (2010) found no evidence to exclude columns from the extraction region to reduce pile-up effects, hence, they extracted the spectrum from a 24 columns wide box around the central column. However, Ng et al. (2010) stated the presence of pile-up which results in removing the four central columns of the 16 columns wide extraction region. The count rate of about 1000 cts/s is above the pile-up limit of 800 cts/s given in the user handbook, which results in a clear occurrence of pile-up (see the corresponding EPATPLOT in Figure 4.9). This finding is emphasized by the pile-up fraction which is determined to be higher than 3% above 7 keV.

First of all simulations were performed based on the best fit results reported by Cackett et al. (2010). The extraction was performed according to Cackett et al. (2010) and Ng et al. (2010). In Table 4.12 the fit results for the used models and the two extraction regions are given. The temperature of the disk blackbody is reproduced in an acceptable way for both models and extraction regions. However, the temperature of the blackbody is slightly higher in the case of the extraction from a region with a width of 24 columns. This could be explained by the occurrence of pile-up.

Moreover, the shape of the line is not affected by the presence of pile-up, the input parameters are reproduced in the case of the diskline model. Fitting the spectrum with Model 2 results in different continuum parameters than the ones reported by Ng et al. (2010). However, the line parameters of the Gaussian reported by them are well in between the error range of the fit of the simulated observation.

Furthermore, since the use of the F-test is not statistically correct to determine if the Gaussian line profile or the DISKLINE model is preferred, the ppp-test³ described by Hurkett et al. (2008) is used. Therefore, a spectrum is simulated using the FAKEIT⁴ command of XSPEC based on the fit results of Model 2. The resulting spectrum is fitted with Model 1 and the difference of the χ^2 is noted. In order to obtain significant results, this is performed 1000 times. Finally, it is checked how often the difference of the χ^2 is larger than the χ^2 of the original fit. The higher this number, the higher the probability that the improvement in χ^2 is caused by chance.

Applying this test on the results reported in Table 4.12 yields to the result that in the case when no columns are excluded the probability of chance improvement is 1.9%, whereas the probability is 46.9% when four columns are excluded. Although the line has a relativistic origin, it can be described almost equally good by the relativistic DISKLINE model and a Gaussian line profile when columns are excluded. In the upper panel of Figure 4.10 the line profiles are shown when performing the analysis in analogy to Cackett et al. (2010) and Ng et al. (2010). It can be seen that in the case of column exclusion the profile tends to be more symmetric and can be therefore characterized by a Gaussian.

Using the parameters reported by Ng et al. (2010) as input for the simulations results in fit parameters given in Table 4.13. Although the line parameters of Cackett et al. (2010) are almost reproduced, a Gaussian line model is preferred since the χ^2 gets even slightly worse (1461.4 compared to 1460.9). This finding is emphasized by the case of excluding columns, here the difference in χ^2 is larger than two.

It can be stated that in both cases the resulting spectra can be modeled by both models. However, the original input model is always preferred.

4.4.2 4U 1705–44

Subsequently, following the same procedure as described for Serpens X-1, the simulations were performed and analysed for 4U 1705-44 which are based on the parameters reported by di Salvo et al. (2009) and are given as Model 1 in Table 4.14.

di Salvo et al. (2009) found a count rate of 767 cts/s and excluded therefore no columns to avoid pile-up effects. They extracted the spectrum from a 13 columns wide box around the central column. However, Ng et al. (2010) stated the necessity to exclude seven columns to achieve a pile-up free spectrum. The EPATPLOT shown

³posterior predictive p values

⁴<http://heasarc.gsfc.nasa.gov/docs/xanadu/xspec/manual/XSfakeit.html>

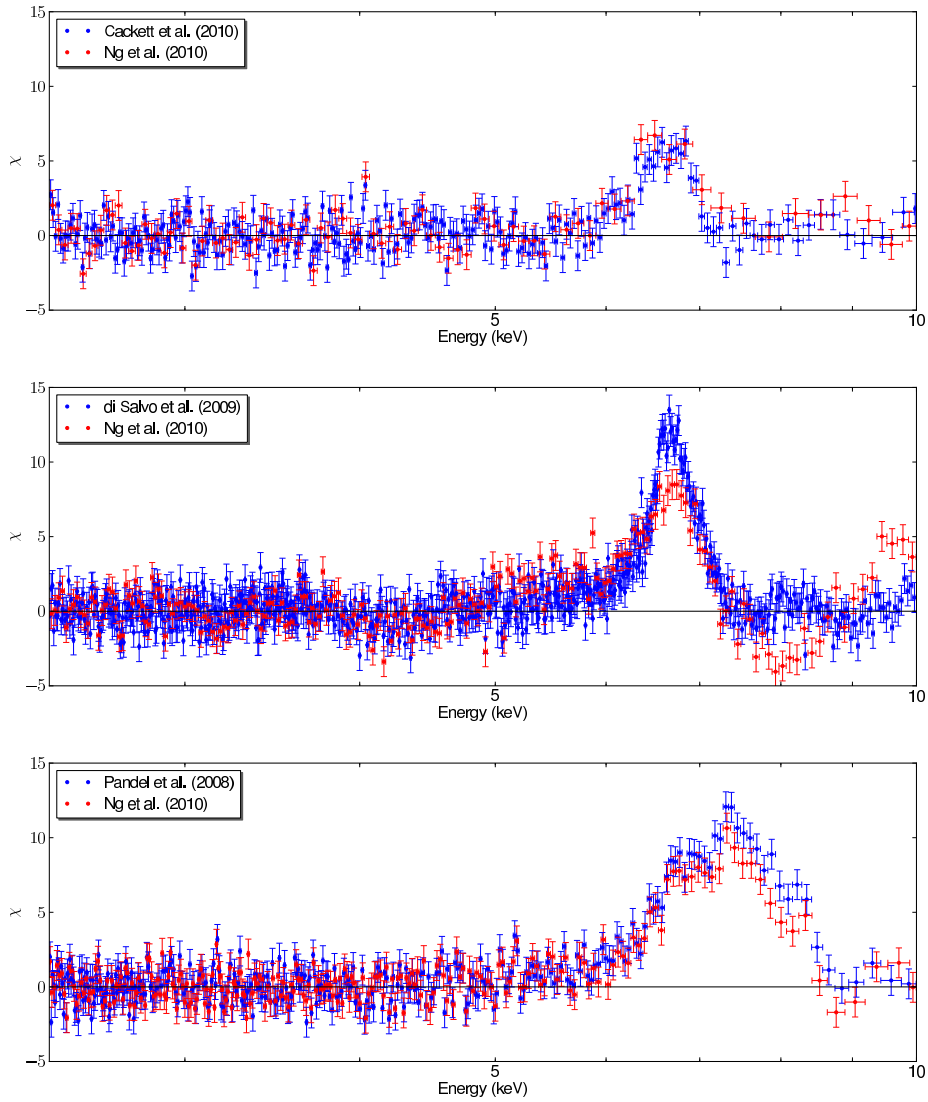


Figure 4.10: Shown are the line profiles of the simulated spectra of Serpens X-1 (upper panel), 4U 1705-44 (middle panel) and 4U 1636-36 (lower panel). The extraction mechanisms and models are according to the references given in the text.

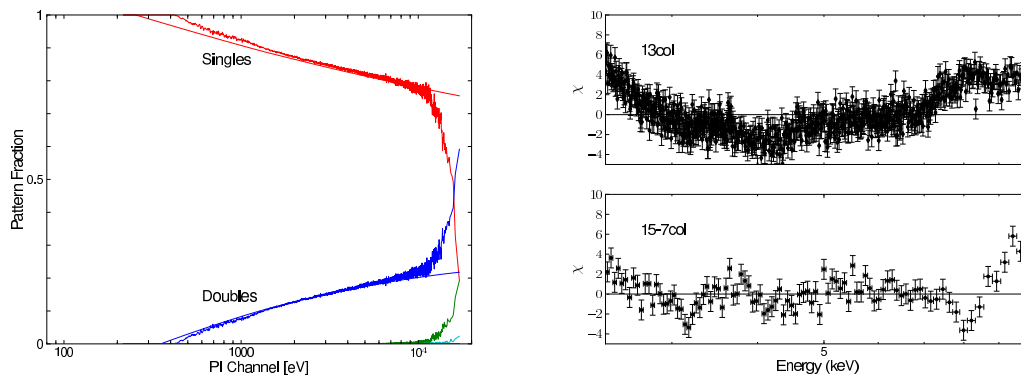


Figure 4.11: *Left side:* Shown is the EPATPLOT of the simulation based on the results reported by di Salvo et al. (2009). *Right panel:* Shown are the spectra when the energy is fixed to the input values for the extraction performed in analogy to di Salvo et al. (2009) (upper panel) and Ng et al. (2010) (lower panel).

in Figure 4.11 gives evidence for appearance of pile-up. Also the calculated pile-up fraction points to the presence of pile-up with a pile-up fraction higher than 5% above 10 keV, however, below 10 keV the pile-up fraction is less than 3%.

As it can be seen in Table 4.14, it is difficult to determine the parameters of the COMPTT model component, though the parameters of the DISKLINE model are reproduced. Using the model suggested by Ng et al. (2010), the spectral shape cannot be modeled.

Studying the simulations results when Model 2 is given as input, showed that pile-up effects do not have any effect on the line. The fit parameters are given in Table 4.15 whereas for the case of no column extraction the blackbody temperature is higher to compensate the hardening of the spectrum caused by pile-up. The relativistic line model used by di Salvo et al. (2009) gives no reasonable values for the inclination angle and therefore it can be stated that it is not capable to fit the spectrum.

In the middle panel of Figure 4.10 the line profiles of both extraction procedures as reported in literature can be seen. It is emphasized that the model used by Ng et al. (2010) is not capable to give a satisfying fit of the simulated spectrum based on di Salvo et al. (2009).

4.4.3 4U 1636–36

Finally, the simulation results were studied for 4U 1636-36 whereas the simulation input model is based on Pandel et al. (2008) which is given Table 4.16. In both publications they found a count rate of about 500 cts/s which should be free from pile-up. Also in the simulations a count rate of about 500 cts/s was obtained, whereas the results of the epatplot is not unique as can be seen in Figure 4.12.

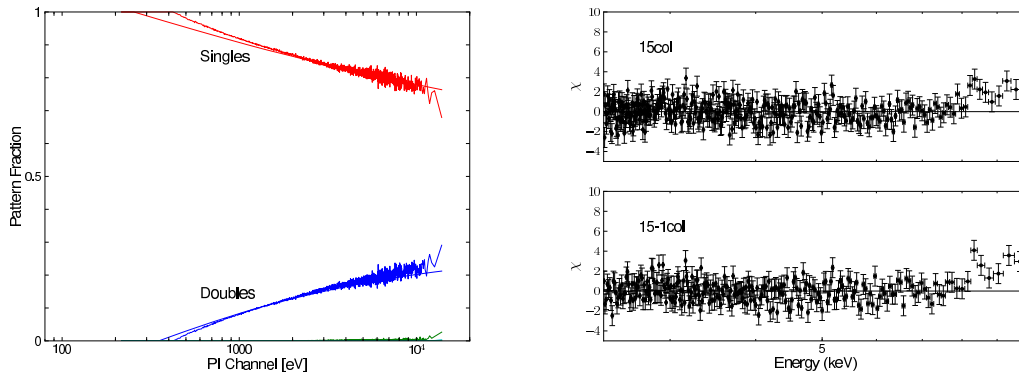


Figure 4.12: *Left side:* Shown is the EPATPLOT of the simulation based on the results reported by Pandel et al. (2008). *Right panel:* Shown are the spectra when the energy is fixed to the input values for the extraction performed in analogy to Pandel et al. (2008) (upper panel) and Ng et al. (2010) (lower panel).

However, a pile-up fraction of well below 3% was determined for all energy ranges. The simulated spectra were extracted from a 15 columns wide box around the central column as well as from the same region but with excluding the central column as in Ng et al. (2010).

As it can be seen in Table 4.16, it is difficult to determine the temperature of the plasma of the COMPTT spectral component. The best-fit result of the inner radius is significant smaller than the input value, which, however, still lies in the error range of the fit. When one column is excluded the input model parameter values of the line model are well reproduced. For the whole extraction region the fit with the alternative Model 2 gives no satisfying results. In the case of excluding one column, the fit with Model 2 is acceptable and the parameter values are close to the ones reported by Ng et al. (2010).

Studying the results of the simulations using the model by Ng et al. (2010) as input, it is observed that the values reported by Pandel et al. (2008) are almost reproduced. As seen in Table 4.17, the centroid energy of the line is higher when using the whole extraction region, but the input value is still in the error range. The relativistic model gives a slightly better χ^2 , however, the probability of chance improvement is 80%.

For this simulation setup the line profiles are shown in the lower panel of Figure 4.10. For both a relativistic profile can be seen, whereas it was discussed before, in the case of column exclusion it can be also fitted with a Gaussian.

4.5 Conclusions

In this work the effect of pile-up for observations performed with the EPIC-PN camera aboard *XMM-Newton* in Timing Mode was studied. This study was done using simulations which have been performed with the SIXTE simulation package. In order to guarantee a proper study, the setup of the PN camera was implemented and tested.

The focus of the study was set on the influence of pile-up on the profile of the iron K_{α} line feature observed in the spectrum of LMXB systems. Different model parameters and fluxes were used to account for different source characteristics. In all simulation setups a higher flux results in a harder spectrum which is an expected effect of pile-up. However, the shape of the line was not influenced by the presence of pile-up. On the contrary, the standard method to decrease pile-up effects, exclusion of the central columns, lead to a worse statistic and make it therefore possible to model an intrinsic relativistic line profile with a Gaussian model.

At first a pure continuum model without any line feature was simulated. When fitting the data, first the temperatures of the blackbody and the disk blackbody as well as the column depth of the absorption were fixed to the input values. Doing so, the change of the spectrum due to pile-up effects can be illustrated. An excess above 8 keV was found which gets more prominent with increasing flux. This is due to the well-known fact, that two photons create a single event for which the energies of both photons are summed up. Checking for pile-up, the SAS tool EPATPLOT gave a clear evidence for pile-up, hence, the central columns were excluded from the extraction as suggested if an observation is affected by pile-up. Indeed, the features caused by pile-up vanish and the input spectrum is reproduced.

A free fit was performed resulting in parameter values which are close to the input values for the non pile-up flux Regime 1 without any columns excluded. Increasing the flux and therefore the probability of pile-up, leads to a higher temperature of the blackbody component, which is necessary to balance the hardening of the spectrum. In general, it can be stated that the values of all input spectral parameters are perfectly reproduced when no pile-up is present.

In a next step a line feature was added to the continuum model. The continuum model parameters showed the same effect as before. To account for different line characteristics, the width of the GAUSSIAN model was varied. No distortion of the line due to pile-up effects were observed for any simulated width. Hence, no evidence for broadening of the line profile or any asymmetry due to pile-up effects were found.

Finally, the impact of pile-up on a relativistic line profile was studied. It was shown that the shape of the line has no influence on the effects on the continuum. Furthermore, a reduced χ^2 close to one with a GAUSSIAN line profile was just achieved, only when columns were excluded. The fit using the DISKLINE model was preferred for most of the combinations of flux and excluded columns. However,

when no pile-up is present the DISKLINE and GAUSSIAN models provide equally good fits and it cannot be distinguished between the origin of the line.

In addition to the study of generic models, simulations based on publications were performed. The focus was set on observations which were reanalyzed by Ng et al. (2010) who claimed that the relativistic origin of the line is potentially caused by pile-up effects. However, the simulations revealed that the intrinsic source model was preferred, even if an alternative model delivered reasonable results. Furthermore, the procedure to reduce pile-up effects enhance the chance that the alternative non-relativistic model is preferred. Therefore, it is essential to carefully take pile-up effects into account. It was shown that the nature of the source can be determined even if pile-up is present. In other words it can be concluded that the analyses published in literature by Cackett et al. (2010), di Salvo et al. (2009) and Pandel et al. (2008) are robust against pile-up and the relativistic origin of the line can be solidly discussed.

Table 4.4: Best-fit parameters when the simulated Gaussian data was fitted with the continuum model and a Gaussian line model. The width of the input line is $\sigma=0.1$ keV. Reported are the results for region 1 (no columns excluded), region 2 (one column excluded), region 3 (three columns excluded) and region 4 (five columns excluded) for the different input fluxes. When no error is given the calculation was not possible.

Parameter	Region 1	Region 2	Region 3	Region 4
$1 \times 10^{-9} \text{ erg s}^{-1} \text{ cm}^{-2}$				
$T_{\text{Dbb}}[\text{keV}]$	$0.95^{+0.03}_{-0.03}$	$0.95^{+0.03}_{-0.04}$	$0.97^{+0.06}_{-0.05}$	$0.98^{+0.09}_{-0.08}$
norm_{Dbb}	$28.8^{+3.7}_{-3.3}$	$29.6^{+4.5}_{-3.9}$	$26.8^{+6.3}_{-5.1}$	$26.2^{+9.4}_{-7.0}$
$kT[\text{keV}]$	$1.96^{+0.04}_{-0.03}$	$1.95^{+0.04}_{-0.03}$	$1.96^{+0.06}_{-0.05}$	$1.91^{+0.08}_{-0.07}$
$\text{norm}_{\text{bb}}[10^{-2}]$	$0.76^{+0.01}_{-0.01}$	$0.79^{+0.1}_{-0.01}$	$0.80^{+0.01}_{-0.02}$	$0.79^{+0.03}_{-0.03}$
$E_{\text{Gau}}[\text{keV}]$	$6.74^{+0.01}_{-0.01}$	$6.74^{+0.01}_{-0.02}$	$6.73^{+0.02}_{-0.02}$	$6.73^{+0.03}_{-0.03}$
$\sigma_{\text{Gau}}[\text{keV}]$	$0.11^{+0.02}_{-0.01}$	$0.11^{+0.02}_{-0.01}$	$0.11^{+0.02}_{-0.02}$	$0.11^{+0.03}_{-0.03}$
$\text{norm}_{\text{Gau}}[10^{-3}]$	$0.57^{+0.06}_{-0.05}$	$0.62^{+0.06}_{-0.06}$	$0.61^{+0.09}_{-0.09}$	$0.70^{+0.13}_{-0.13}$
red. χ^2 (1512 dof)	1.0091	1.0504	1.0254	1.0359
$4.5 \times 10^{-9} \text{ erg s}^{-1} \text{ cm}^{-2}$				
$T_{\text{Dbb}}[\text{keV}]$	$0.97^{+0.02}_{-0.01}$	$0.97^{+0.02}_{-0.01}$	$1.00^{+0.03}_{-0.03}$	$1.01^{+0.04}_{-0.04}$
norm_{Dbb}	$116.3^{+6.8}_{-6.5}$	$119.7^{+8.3}_{-7.9}$	$107.8^{+11.3}_{-10.4}$	$108.2^{+16.9}_{-14.9}$
$kT[\text{keV}]$	$2.00^{+0.02}_{-0.02}$	$2.00^{+0.02}_{-0.02}$	$2.01^{+0.03}_{-0.03}$	$1.98^{+0.05}_{-0.03}$
$\text{norm}_{\text{bb}}[10^{-2}]$	$3.45^{+0.02}_{-0.02}$	$3.62^{+0.02}_{-0.02}$	$3.61^{+0.03}_{-0.04}$	$3.67^{+0.06}_{-0.05}$
$E_{\text{Gau}}[\text{keV}]$	$6.75^{+0.01}_{-0.01}$	$6.74^{+0.01}_{-0.01}$	$6.74^{+0.01}_{-0.01}$	$6.73^{+0.01}_{-0.01}$
$\sigma_{\text{Gau}}[\text{keV}]$	$0.10^{+0.01}_{-0.01}$	$0.10^{+0.01}_{-0.01}$	$0.11^{+0.01}_{-0.02}$	$0.10^{+0.02}_{-0.02}$
$\text{norm}_{\text{Gau}}[10^{-3}]$	$2.25^{+0.11}_{-0.10}$	$2.42^{+0.12}_{-0.13}$	$2.53^{+0.18}_{-0.19}$	$2.67^{+0.27}_{-0.27}$
red. χ^2 (1512 dof)	1.0434	1.0121	0.9591	1.0352
$1 \times 10^{-8} \text{ erg s}^{-1} \text{ cm}^{-2}$				
$T_{\text{Dbb}}[\text{keV}]$	$0.99^{+0.01}_{-0.01}$	$0.99^{+0.01}_{-0.02}$	$1.00^{+0.02}_{-0.02}$	$1.02^{+0.02}_{-0.01}$
norm_{Dbb}	$245.7^{+9.6}_{-9.3}$	$255.1^{+11.7}_{-11.2}$	$244.2^{+16.7}_{-15.7}$	$236.9^{+23.5}_{-21.7}$
$kT[\text{keV}]$	$2.04^{+0.01}_{-0.01}$	$2.04^{+0.01}_{-0.01}$	$2.02^{+0.02}_{-0.02}$	$2.02^{+0.03}_{-0.02}$
$\text{norm}_{\text{bb}}[10^{-2}]$	$7.76^{+0.02}_{-0.03}$	$8.13^{+0.03}_{-0.03}$	$8.08^{+0.05}_{-0.04}$	$8.19^{+0.08}_{-0.07}$
$E_{\text{Gau}}[\text{keV}]$	$6.75^{+0.00}_{-0.01}$	$6.74^{+0.01}_{-0.01}$	$6.74^{+0.01}_{-0.01}$	$6.75^{+0.01}_{-0.01}$
$\sigma_{\text{Gau}}[\text{keV}]$	$0.10^{+0.01}_{-0.01}$	$0.11^{+0.01}_{-0.01}$	$0.11^{+0.01}_{-0.01}$	$0.12^{+0.02}_{-0.01}$
$\text{norm}_{\text{Gau}}[10^{-3}]$	$4.92^{+0.16}_{-0.16}$	$5.26^{+0.19}_{-0.20}$	$5.84^{+0.29}_{-0.29}$	$6.53^{+0.43}_{-0.46}$
red. χ^2 (1512 dof)	0.9774	0.9371	0.9392	1.0127

Table 4.5: Best-fit parameters when the simulated Gaussian data was fitted with the continuum model and the relativistic diskline model. The width of the input line is $\sigma=0.1$ keV. Reported are the results for region 1 (no columns excluded), region 2 (one column excluded), region 3 (three columns excluded) and region 4 (five columns excluded) for the different input fluxes. When no error is given the calculation was not possible.

Parameter	Region 1	Region 2	Region 3	Region 4
$1 \times 10^{-9} \text{ erg s}^{-1} \text{ cm}^{-2}$				
$T_{\text{Dbb}}[\text{keV}]$	$0.94^{+0.03}_{-0.03}$	$0.94^{+0.04}_{-0.03}$	$0.97^{+0.05}_{-0.05}$	$0.98^{+0.08}_{-0.08}$
norm_{Dbb}	$29.4^{+3.7}_{-3.3}$	$30.3^{+4.5}_{-4.0}$	$27.2^{+6.3}_{-5.1}$	$26.5^{+9.6}_{-6.9}$
$kT[\text{keV}]$	$1.96^{+0.03}_{-0.03}$	$1.95^{+0.04}_{-0.03}$	$1.96^{+0.06}_{-0.05}$	$1.90^{+0.08}_{-0.06}$
$\text{norm}_{\text{bb}}[10^{-2}]$	$0.76^{+0.01}_{-0.01}$	$0.80^{+0.01}_{-0.01}$	$0.80^{+0.01}_{-0.02}$	$0.79^{+0.03}_{-0.02}$
$E_{\text{Disk}}[\text{keV}]$	$6.76^{+0.02}_{-0.03}$	$6.75^{+0.02}_{-0.02}$	$6.73^{+0.02}_{-0.02}$	$6.73^{+0.03}_{-0.02}$
$R_{\text{in}}[\text{GM}/c^2]$	$245.6^{+9658.9}_{-144.5}$	$345.9^{+9597.2}_{-128.3}$	$996.3^{+9003.4}_{-898.2}$	$992.6^{+9006.8}_{-928.8}$
Incl [deg]	$24.3^{+17.4}_{-7.4}$	$27.5^{+16.1}_{-9.4}$	$38.4^{+7.5}_{-7.6}$	$37.8^{+9.9}_{-10.6}$
$\text{norm}_{\text{Disk}}[10^{-3}]$	$0.54^{+0.05}_{-0.04}$	$0.59^{+0.04}_{-0.06}$	$0.59^{+0.07}_{-0.07}$	$0.67^{+0.10}_{-0.10}$
red. χ^2 (1511 dof)	1.0123	1.0527	1.0256	1.0362
$4.5 \times 10^{-9} \text{ erg s}^{-1} \text{ cm}^{-2}$				
$T_{\text{Dbb}}[\text{keV}]$	$0.97^{+0.02}_{-0.01}$	$0.97^{+0.02}_{-0.02}$	$1.00^{+0.02}_{-0.03}$	$1.00^{+0.05}_{-0.03}$
norm_{Dbb}	$117.6^{+6.7}_{-6.7}$	$121.1^{+8.3}_{-7.9}$	$109.2^{+11.2}_{-10.5}$	$109.9^{+16.8}_{-14.9}$
$kT[\text{keV}]$	$2.00^{+0.01}_{-0.02}$	$2.00^{+0.02}_{-0.02}$	$2.00^{+0.03}_{-0.02}$	$1.98^{+0.04}_{-0.04}$
$\text{norm}_{\text{bb}}[10^{-2}]$	$3.46^{+0.01}_{-0.02}$	$3.63^{+0.02}_{-0.02}$	$3.61^{+0.04}_{-0.03}$	$3.68^{+0.05}_{-0.05}$
$E_{\text{Disk}}[\text{keV}]$	$6.76^{+0.02}_{-0.01}$	$6.76^{+0.02}_{-0.01}$	$6.76^{+0.02}_{-0.02}$	$6.74^{+0.03}_{-0.02}$
$R_{\text{in}}[\text{GM}/c^2]$	$273.6^{+9708.0}_{-137.9}$	$205.1^{+9775.4}_{-90.7}$	$173.9^{+9804.1}_{-86.7}$	$301.4^{+674.4}_{-198.8}$
Incl [deg]	$23.0^{+12.9}_{-5.3}$	$21.4^{+15.7}_{-4.4}$	$20.9^{+22.1}_{-5.4}$	$24.3^{+15.8}_{-11.3}$
$\text{norm}_{\text{Disk}}[10^{-3}]$	$2.20^{+0.09}_{-0.10}$	$2.35^{+0.11}_{-0.12}$	$2.45^{+0.17}_{-0.17}$	$2.58^{+0.25}_{-0.23}$
red. χ^2 (1511 dof)	1.0437	1.0152	0.9606	1.0339
$1 \times 10^{-8} \text{ erg s}^{-1} \text{ cm}^{-2}$				
$T_{\text{Dbb}}[\text{keV}]$	$0.99^{+0.01}_{-0.01}$	$0.98^{+0.02}_{-0.01}$	$0.99^{+0.02}_{-0.02}$	$1.01^{+0.03}_{-0.03}$
norm_{Dbb}	$248.1^{+9.7}_{-9.2}$	$258.0^{+11.7}_{-11.2}$	$248.9^{+16.8}_{-15.8}$	$253.3^{+13.8}_{-31.8}$
$kT[\text{keV}]$	$2.04^{+0.01}_{-0.01}$	$2.04^{+0.01}_{-0.02}$	$2.02^{+0.02}_{-0.02}$	$2.01^{+0.03}_{-0.02}$
$\text{norm}_{\text{bb}}[10^{-2}]$	$7.77^{+0.02}_{-0.03}$	$8.15^{+0.03}_{-0.03}$	$8.10^{+0.05}_{-0.04}$	$8.23^{+0.07}_{-0.08}$
$E_{\text{Disk}}[\text{keV}]$	$6.77^{+0.01}_{-0.01}$	$6.77^{+0.01}_{-0.01}$	$6.76^{+0.02}_{-0.01}$	$6.77^{+0.01}_{-0.02}$
$R_{\text{in}}[\text{GM}/c^2]$	$155.3^{+119.8}_{-44.0}$	$164.3^{+155.6}_{-53.3}$	$192.8^{+361.0}_{-81.0}$	$236.1^{+9710.7}_{-114.4}$
Incl [deg]	$19.7^{+4.3}_{-2.4}$	$20.6^{+5.1}_{-2.8}$	$22.8^{+9.1}_{-4.1}$	$26.1^{+17.3}_{-5.6}$
$\text{norm}_{\text{Disk}}[10^{-3}]$	$4.79^{+0.15}_{-0.15}$	$5.10^{+0.18}_{-0.18}$	$5.58^{+0.27}_{-0.27}$	$6.18^{+0.39}_{-0.39}$
red. χ^2 (1511 dof)	0.9792	0.9407	0.9474	1.0180

Table 4.6: Best-fit parameters when the simulated Gaussian data was fitted with the continuum model and a Gaussian line model. The width of the input line is $\sigma=0.4$ keV. Reported are the results for region 1 (no columns excluded), region 2 (one column excluded), region 3 (three columns excluded) and region 4 (five columns excluded) for the different input fluxes. When no error is given the calculation was not possible.

Parameter	Region 1	Region 2	Region 3	Region 4
$1 \times 10^{-9} \text{ erg s}^{-1} \text{ cm}^{-2}$				
$T_{\text{Dbb}}[\text{keV}]$	$0.95^{+0.04}_{-0.04}$	$0.96^{+0.05}_{-0.04}$	$0.98^{+0.09}_{-0.06}$	$0.97^{+0.10}_{-0.09}$
norm_{Dbb}	$28.2^{+4.3}_{-3.6}$	$27.1^{+5.1}_{-4.5}$	$24.5^{+6.9}_{-6.4}$	$26.3^{+11.3}_{-8.4}$
$kT[\text{keV}]$	$1.95^{+0.03}_{-0.04}$	$1.96^{+0.04}_{-0.04}$	$1.94^{+0.07}_{-0.06}$	$1.84^{+0.09}_{-0.07}$
$\text{norm}_{\text{bb}}[10^{-2}]$	$0.76^{+0.01}_{-0.01}$	$0.79^{+0.1}_{-0.01}$	$0.79^{+0.02}_{-0.03}$	$0.79^{+0.03}_{-0.03}$
$E_{\text{Gau}}[\text{keV}]$	$6.71^{+0.07}_{-0.07}$	$6.72^{+0.08}_{-0.09}$	$6.94^{+0.15}_{-0.19}$	$6.98^{+0.13}_{-0.12}$
$\sigma_{\text{Gau}}[\text{keV}]$	$0.36^{+0.09}_{-0.08}$	$0.38^{+0.11}_{-0.09}$	$0.35^{+0.28}_{-0.15}$	$0.30^{+0.15}_{-0.12}$
$\text{norm}_{\text{Gau}}[10^{-3}]$	$0.46^{+0.12}_{-0.11}$	$0.49^{+0.16}_{-0.13}$	$0.38^{+0.31}_{-0.17}$	$0.48^{+0.25}_{-0.19}$
red. χ^2 (1512 dof)	1.0433	1.0690	1.0461	1.0502
$4.5 \times 10^{-9} \text{ erg s}^{-1} \text{ cm}^{-2}$				
$T_{\text{Dbb}}[\text{keV}]$	$0.95^{+0.01}_{-0.02}$	$0.95^{+0.01}_{-0.02}$	$0.97^{+0.03}_{-0.03}$	$0.99^{+0.04}_{-0.04}$
norm_{Dbb}	$129.2^{+8.6}_{-8.2}$	$134.6^{+10.4}_{-9.9}$	$120.9^{+14.2}_{-13.0}$	$115.8^{+19.8}_{-17.7}$
$kT[\text{keV}]$	$1.98^{+0.02}_{-0.02}$	$1.98^{+0.02}_{-0.02}$	$1.98^{+0.03}_{-0.02}$	$1.96^{+0.05}_{-0.03}$
$\text{norm}_{\text{bb}}[10^{-2}]$	$3.49^{+0.02}_{-0.02}$	$3.67^{+0.02}_{-0.03}$	$3.64^{+0.04}_{-0.04}$	$3.70^{+0.06}_{-0.06}$
$E_{\text{Gau}}[\text{keV}]$	$6.78^{+0.03}_{-0.04}$	$6.76^{+0.04}_{-0.04}$	$6.78^{+0.05}_{-0.05}$	$6.76^{+0.06}_{-0.07}$
$\sigma_{\text{Gau}}[\text{keV}]$	$0.38^{+0.04}_{-0.03}$	$0.37^{+0.04}_{-0.04}$	$0.37^{+0.05}_{-0.05}$	$0.34^{+0.08}_{-0.07}$
$\text{norm}_{\text{Gau}}[10^{-3}]$	$2.01^{+0.24}_{-0.23}$	$2.17^{+0.31}_{-0.27}$	$2.33^{+0.43}_{-0.39}$	$2.41^{+0.60}_{-0.63}$
red. χ^2 (1512 dof)	0.9821	1.0227	1.0309	1.0194
$1 \times 10^{-8} \text{ erg s}^{-1} \text{ cm}^{-2}$				
$T_{\text{Dbb}}[\text{keV}]$	$0.98^{+0.02}_{-0.01}$	$0.99^{+0.01}_{-0.02}$	$0.99^{+0.02}_{-0.02}$	$0.99^{+0.03}_{-0.03}$
norm_{Dbb}	$248.1^{+11.5}_{-11.2}$	$253.6^{+13.9}_{-13.4}$	$248.4^{+20.5}_{-19.6}$	$259.0^{+30.2}_{-28.2}$
$kT[\text{keV}]$	$2.04^{+0.01}_{-0.02}$	$2.04^{+0.01}_{-0.02}$	$2.01^{+0.02}_{-0.03}$	$1.97^{+0.03}_{-0.03}$
$\text{norm}_{\text{bb}}[10^{-2}]$	$7.78^{+0.03}_{-0.04}$	$8.14^{+0.04}_{-0.04}$	$8.09^{+0.07}_{-0.07}$	$8.27^{+0.10}_{-0.10}$
$E_{\text{Gau}}[\text{keV}]$	$6.76^{+0.02}_{-0.03}$	$6.76^{+0.03}_{-0.03}$	$6.75^{+0.04}_{-0.04}$	$6.76^{+0.05}_{-0.05}$
$\sigma_{\text{Gau}}[\text{keV}]$	$0.39^{+0.03}_{-0.03}$	$0.39^{+0.04}_{-0.03}$	$0.41^{+0.05}_{-0.05}$	$0.37^{+0.06}_{-0.06}$
$\text{norm}_{\text{Gau}}[10^{-3}]$	$4.45^{+0.42}_{-0.39}$	$4.91^{+0.52}_{-0.48}$	$5.46^{+0.80}_{-0.72}$	$5.27^{+1.03}_{-0.90}$
red. χ^2 (1512 dof)	1.0244	1.0514	1.0582	1.0550

Table 4.7: Best-fit parameters when the simulated Gaussian data was fitted with the continuum model and the relativistic diskline model. The width of the input line is $\sigma=0.4$ keV. Reported are the results for region 1 (no columns excluded), region 2 (one column excluded), region 3 (three columns excluded) and region 4 (five columns excluded) for the different input fluxes. When no error is given the calculation was not possible.

Parameter	Region 1	Region 2	Region 3	Region 4
$1 \times 10^{-9} \text{ erg s}^{-1} \text{ cm}^{-2}$				
$T_{\text{Dbb}}[\text{keV}]$	$0.99^{+0.04}_{-0.04}$	$0.98^{+0.06}_{-0.04}$	$0.97^{+0.01}_{-0.03}$	$0.95^{+0.09}_{-0.08}$
norm_{Dbb}	$24.2^{+8.3}_{-3.5}$	$25.4^{+3.3}_{-3.1}$	$26.2^{+3.2}_{-1.0}$	$27.5^{+7.5}_{-7.9}$
$kT[\text{keV}]$	$1.99^{+0.05}_{-0.05}$	$1.98^{+0.06}_{-0.05}$	$1.92^{+0.06}_{-0.04}$	$1.84^{+0.07}_{-0.04}$
$\text{norm}_{\text{bb}}[10^{-2}]$	$0.75^{+0.02}_{-0.02}$	$0.79^{+0.01}_{-0.02}$	$0.80^{+0.01}_{-0.02}$	$0.80^{+0.02}_{-0.03}$
$E_{\text{Disk}}[\text{keV}]$	$6.57^{+0.16}_{-0.08}$	$6.61^{+0.11}_{-0.10}$	$6.98^{+0.06}_{-0.05}$	$6.99^{+0.10}_{-0.08}$
$R_{\text{in}}[\text{GM}/c^2]$	$8.6^{+97.1}_{-2.6}$	$7.7^{+53.3}_{-1.7}$	$466.7^{+500.1}_{460.7}$	$387.2^{+9578.2}_{-382.2}$
Incl [deg]	$49.9^{+19.7}_{-9.1}$	$42.5^{+21.8}_{-3.6}$	$90.0_{-45.0}$	$89.9^{+0.1}_{-60.0}$
$\text{norm}_{\text{Disk}}[10^{-3}]$	$0.72^{+0.17}_{-0.39}$	$0.63^{+0.18}_{-0.24}$	$0.28^{+0.10}_{-0.09}$	$0.40^{+0.36}_{-0.14}$
red. χ^2 (1511 dof)	1.0486	1.0709	1.0440	1.0502
$4.5 \times 10^{-9} \text{ erg s}^{-1} \text{ cm}^{-2}$				
$T_{\text{Dbb}}[\text{keV}]$	$0.94^{+0.02}_{-0.01}$	$0.94^{+0.02}_{-0.02}$	$0.97^{+0.03}_{-0.03}$	$0.99^{+0.07}_{-0.04}$
norm_{Dbb}	$131.2^{+8.4}_{-7.8}$	$137.2^{+10.4}_{-9.6}$	$121.6^{+14.5}_{-12.0}$	$116.0^{+20.2}_{-17.7}$
$kT[\text{keV}]$	$1.98^{+0.01}_{-0.02}$	$1.98^{+0.02}_{-0.02}$	$1.98^{+0.03}_{-0.02}$	$1.97^{+0.06}_{-0.04}$
$\text{norm}_{\text{bb}}[10^{-2}]$	$3.50^{+0.02}_{-0.02}$	$3.67^{+0.03}_{-0.02}$	$3.65^{+0.04}_{-0.04}$	$3.71^{+0.06}_{-0.11}$
$E_{\text{Disk}}[\text{keV}]$	$6.75^{+0.04}_{-0.04}$	$6.75^{+0.04}_{-0.04}$	$6.76^{+0.06}_{-0.06}$	$6.76^{+0.07}_{-0.08}$
$R_{\text{in}}[\text{GM}/c^2]$	$72.0^{+28.4}_{-21.2}$	$67.6^{+32.5}_{-22.4}$	$62.9^{+52.6}_{28.2}$	$47.0^{+56.5}_{-40.2}$
Incl [deg]	$66.9^{+23.1}_{-13.5}$	$60.0^{+30.0}_{-12.4}$	$58.1^{+31.9}_{-15.6}$	$48.2^{+41.8}_{-11.4}$
$\text{norm}_{\text{Disk}}[10^{-3}]$	$1.86^{+0.19}_{-0.15}$	$2.00^{+0.23}_{-0.24}$	$2.21^{+0.36}_{-0.35}$	$2.34^{+1.33}_{-0.48}$
red. χ^2 (1511 dof)	0.9847	1.0291	1.0302	1.0211
$1 \times 10^{-8} \text{ erg s}^{-1} \text{ cm}^{-2}$				
$T_{\text{Dbb}}[\text{keV}]$	$0.98^{+0.02}_{-0.01}$	$0.99^{+0.01}_{-0.02}$	$1.01^{+0.03}_{-0.03}$	$1.03^{+0.04}_{-0.03}$
norm_{Dbb}	$248.8^{+12.8}_{-11.4}$	$254.2^{+14.4}_{-13.5}$	$229.8^{+25.4}_{-19.9}$	$221.6^{+29.0}_{-27.1}$
$kT[\text{keV}]$	$2.04^{+0.01}_{-0.02}$	$2.04^{+0.02}_{-0.01}$	$2.03^{+0.03}_{-0.03}$	$2.02^{+0.04}_{-0.04}$
$\text{norm}_{\text{bb}}[10^{-2}]$	$7.79^{+0.04}_{-0.04}$	$8.15^{+0.04}_{-0.04}$	$8.02^{+0.12}_{-0.09}$	$8.10^{+0.12}_{-0.14}$
$E_{\text{Disk}}[\text{keV}]$	$6.73^{+0.03}_{-0.03}$	$6.73^{+0.03}_{-0.03}$	$6.68^{+0.05}_{-0.05}$	$6.66^{+0.06}_{-0.06}$
$R_{\text{in}}[\text{GM}/c^2]$	$35.1^{+20.7}_{-10.1}$	$32.7^{+25.4}_{-9.1}$	$18.6^{+17.8}_{-8.0}$	$11.2^{+16.5}_{-4.8}$
Incl [deg]	$48.5^{+7.6}_{-5.3}$	$48.2^{+8.2}_{-5.3}$	$52.9^{+12.1}_{-5.7}$	$50.0^{+9.5}_{-3.2}$
$\text{norm}_{\text{Disk}}[10^{-3}]$	$4.28^{+0.44}_{-0.46}$	$4.74^{+0.52}_{-0.57}$	$6.63^{+1.15}_{-1.34}$	$7.89^{+1.56}_{-1.64}$
red. χ^2 (1511 dof)	1.0376	1.0596	1.0616	1.1067

Table 4.8: Best-fit parameters when the simulated Gaussian data was fitted with the continuum model and a Gaussian line model. The width of the input line is $\sigma=1.0$ keV. Reported are the results for region 1 (no columns excluded), region 2 (one column excluded), region 3 (three columns excluded) and region 4 (five columns excluded) for the different input fluxes. When no error is given the calculation was not possible.

Parameter	Region 1	Region 2	Region 3	Region 4
$1 \times 10^{-9} \text{ erg s}^{-1} \text{ cm}^{-2}$				
$T_{\text{Dbb}}[\text{keV}]$	$0.93^{+0.08}_{-0.07}$	$0.97^{+0.13}_{-0.09}$	$1.00^{+0.28}_{-0.12}$	$1.04^{+0.63}_{-0.19}$
norm_{Dbb}	$29.8^{+9.1}_{-6.8}$	$26.0^{+10.3}_{-9.4}$	$23.1^{+14.1}_{-12.7}$	$21.0^{+23.4}_{-16.1}$
$kT[\text{keV}]$	$1.94^{+0.08}_{-0.05}$	$1.98^{+0.17}_{-0.07}$	$2.00^{+0.45}_{-0.11}$	$1.99^{+0.09}_{-0.17}$
$\text{norm}_{\text{bb}}[10^{-2}]$	$0.73^{+0.03}_{-0.04}$	$0.75^{+0.04}_{-0.07}$	$0.74^{+0.06}_{-0.12}$	$0.72^{+0.09}_{-0.15}$
$E_{\text{Gau}}[\text{keV}]$	$6.75^{+0.07}_{-0.05}$	$6.72^{+0.07}_{-0.08}$	$6.69^{+0.09}_{-0.10}$	$6.62^{+0.14}_{-0.18}$
$\sigma_{\text{Gau}}[\text{keV}]$	$1.00^{+0.09}_{-0.07}$	$1.03^{+0.11}_{-0.09}$	$0.99^{+0.16}_{-0.12}$	$1.04^{+0.41}_{-0.17}$
$\text{norm}_{\text{Gau}}[10^{-2}]$	$0.49^{+0.09}_{-0.07}$	$0.55^{+0.16}_{-0.09}$	$0.54^{+0.27}_{-0.13}$	$0.62^{+0.97}_{-0.20}$
red. χ^2 (1512 dof)	1.0161	0.9910	1.0114	1.0935
$4.5 \times 10^{-9} \text{ erg s}^{-1} \text{ cm}^{-2}$				
$T_{\text{Dbb}}[\text{keV}]$	$0.94^{+0.04}_{-0.03}$	$0.96^{+0.04}_{-0.04}$	$0.95^{+0.06}_{-0.05}$	$0.95^{+0.09}_{-0.07}$
norm_{Dbb}	$123.0^{+16.6}_{-15.9}$	$121.3^{+19.8}_{-18.9}$	$124.3^{+28.1}_{-25.9}$	$127.8^{+40.4}_{-36.6}$
$kT[\text{keV}]$	$1.96^{+0.04}_{-0.02}$	$1.98^{+0.04}_{-0.04}$	$1.95^{+0.05}_{-0.04}$	$1.93^{+0.09}_{-0.05}$
$\text{norm}_{\text{bb}}[10^{-2}]$	$3.33^{+0.06}_{-0.08}$	$3.46^{+0.08}_{-0.10}$	$3.50^{+0.10}_{-0.13}$	$3.62^{+0.14}_{-0.21}$
$E_{\text{Gau}}[\text{keV}]$	$6.78^{+0.02}_{-0.03}$	$6.76^{+0.03}_{-0.03}$	$6.77^{+0.04}_{-0.04}$	$6.75^{+0.05}_{-0.06}$
$\sigma_{\text{Gau}}[\text{keV}]$	$0.98^{+0.04}_{-0.03}$	$0.99^{+0.04}_{-0.02}$	$0.95^{+0.06}_{-0.05}$	$0.94^{+0.08}_{-0.07}$
$\text{norm}_{\text{Gau}}[10^{-2}]$	$2.15^{+0.18}_{-0.15}$	$2.32^{+0.23}_{-0.19}$	$2.21^{+0.29}_{-0.23}$	$2.20^{+0.43}_{-0.31}$
red. χ^2 (1512 dof)	0.9819	0.9678	0.9381	1.0217
$1 \times 10^{-8} \text{ erg s}^{-1} \text{ cm}^{-2}$				
$T_{\text{Dbb}}[\text{keV}]$	$0.95^{+0.03}_{-0.02}$	$0.97^{+0.03}_{-0.03}$	$0.92^{+0.04}_{-0.03}$	$0.90^{+0.05}_{-0.04}$
norm_{Dbb}	$264.5^{+24.8}_{-24.4}$	$257.6^{+29.2}_{-28.7}$	$301.7^{+43.4}_{-41.5}$	$349.0^{+67.6}_{-63.3}$
$kT[\text{keV}]$	$2.01^{+0.03}_{-0.02}$	$2.03^{+0.03}_{-0.03}$	$1.96^{+0.04}_{-0.03}$	$1.91^{+0.05}_{-0.03}$
$\text{norm}_{\text{bb}}[10^{-2}]$	$7.54^{+0.10}_{-0.12}$	$7.83^{+0.13}_{-0.15}$	$8.02^{+0.14}_{-0.17}$	$8.32^{+0.18}_{-0.23}$
$E_{\text{Gau}}[\text{keV}]$	$6.77^{+0.02}_{-0.02}$	$6.76^{+0.02}_{-0.02}$	$6.76^{+0.03}_{-0.03}$	$6.76^{+0.04}_{-0.04}$
$\sigma_{\text{Gau}}[\text{keV}]$	$0.99^{+0.03}_{-0.02}$	$1.00^{+0.03}_{-0.03}$	$0.93^{+0.04}_{-0.04}$	$0.90^{+0.05}_{-0.05}$
$\text{norm}_{\text{Gau}}[10^{-2}]$	$4.63^{+0.29}_{-0.25}$	$4.99^{+0.36}_{-0.31}$	$4.53^{+0.39}_{-0.33}$	$4.46^{+0.51}_{-0.41}$
red. χ^2 (1512 dof)	1.0622	1.0511	1.0725	1.0438

Table 4.9: Best-fit parameters when the simulated Gaussian data was fitted with the continuum model and the relativistic diskline model. The width of the input line is $\sigma=1.0$ keV. Reported are the results for region 1 (no columns excluded), region 2 (one column excluded), region 3 (three columns excluded) and region 4 (five columns excluded) for the different input fluxes. When no error is given the calculation was not possible.

Parameter	Region 1	Region 2	Region 3	Region 4
$1 \times 10^{-9} \text{ erg s}^{-1} \text{ cm}^{-2}$				
$T_{\text{Dbb}}[\text{keV}]$	$0.83^{+0.03}_{-0.03}$	$0.83^{+0.04}_{-0.03}$	$0.82^{+0.06}_{-0.04}$	$0.78^{+0.05}_{-0.05}$
norm_{Dbb}	$45.0^{+7.6}_{-6.2}$	$45.8^{+9.1}_{-7.9}$	$47.8^{+12.2}_{-11.1}$	$61.0^{+22.7}_{-14.5}$
$kT[\text{keV}]$	$1.87^{+0.03}_{-0.02}$	$1.89^{+0.03}_{-0.03}$	$1.87^{+0.05}_{-0.03}$	$1.79^{+0.03}_{-0.03}$
$\text{norm}_{\text{bb}}[10^{-2}]$	$0.78^{+0.01}_{-0.01}$	$0.82^{+0.01}_{-0.02}$	$0.83^{+0.02}_{-0.02}$	$0.85^{+0.03}_{-0.02}$
$E_{\text{Disk}}[\text{keV}]$	$6.61^{+0.04}_{-0.04}$	$6.62^{+0.05}_{-0.05}$	$6.69^{+0.05}_{-0.07}$	$6.73^{+0.07}_{-0.06}$
$R_{\text{in}}[\text{GM}/c^2]$	$7.3^{+1.1}_{-1.3}$	$8.3^{+1.4}_{-2.2}$	$12.4^{+3.7}_{-4.3}$	$15.0^{+7.4}_{-6.4}$
Incl [deg]	$90.0_{-17.6}$	$90.0_{-17.7}$	$90.0_{-14.2}$	$90.0_{-22.4}$
$\text{norm}_{\text{Disk}}[10^{-3}]$	$3.86^{+0.28}_{-0.31}$	$3.84^{+0.36}_{-0.34}$	$3.28^{+0.68}_{-0.38}$	$3.12^{+0.64}_{-0.51}$
red. χ^2 (1511 dof)	1.0377	1.0182	1.0282	1.1048
$4.5 \times 10^{-9} \text{ erg s}^{-1} \text{ cm}^{-2}$				
$T_{\text{Dbb}}[\text{keV}]$	$0.86^{+0.01}_{-0.01}$	$0.85^{+0.02}_{-0.01}$	$0.86^{+0.03}_{-0.01}$	$0.86^{+0.04}_{-0.04}$
norm_{Dbb}	$177.6^{+8.3}_{-9.9}$	$186.8^{+4.5}_{-17.9}$	$181.5^{+4.4}_{-11.5}$	$183.7^{+39.6}_{-28.7}$
$kT[\text{keV}]$	$1.91^{+0.01}_{-0.01}$	$1.90^{+0.02}_{-0.01}$	$1.89^{+0.01}_{-0.01}$	$1.88^{+0.03}_{-0.04}$
$\text{norm}_{\text{bb}}[10^{-2}]$	$3.51^{+0.02}_{-0.02}$	$3.67^{+0.04}_{-0.04}$	$3.68^{+0.05}_{-0.04}$	$3.80^{+0.07}_{-0.07}$
$E_{\text{Disk}}[\text{keV}]$	$6.62^{+0.02}_{-0.02}$	$6.61^{+0.03}_{-0.02}$	$6.63^{+0.04}_{-0.02}$	$6.61^{+0.07}_{-0.05}$
$R_{\text{in}}[\text{GM}/c^2]$	$7.4^{+0.5}_{-0.4}$	$7.3^{+1.2}_{-0.7}$	$8.0^{+1.1}_{-0.7}$	$8.1^{+2.3}_{-2.1}$
Incl [deg]	$90.0_{-4.8}$	$90.0_{-9.2}$	$90.0_{6.6}$	$90.0_{-22.5}$
$\text{norm}_{\text{Disk}}[10^{-3}]$	$17.55^{+0.61}_{-0.82}$	$18.60^{+1.03}_{-1.00}$	$18.33^{+1.50}_{-0.97}$	$18.35^{+1.83}_{-1.91}$
red. χ^2 (1511 dof)	1.1501	1.1068	0.9988	1.0589
$1 \times 10^{-8} \text{ erg s}^{-1} \text{ cm}^{-2}$				
$T_{\text{Dbb}}[\text{keV}]$	$0.86^{+0.01}_{-0.01}$	$0.86^{+0.01}_{-0.02}$	$0.85^{+0.02}_{-0.02}$	$0.84^{+0.03}_{-0.02}$
norm_{Dbb}	$389.3^{+16.6}_{-18.0}$	$396.4^{+23.0}_{-21.1}$	$418.5^{+35.1}_{-33.5}$	$453.6^{+59.4}_{-56.6}$
$kT[\text{keV}]$	$1.95^{+0.01}_{-0.01}$	$1.95^{+0.01}_{-0.01}$	$1.92^{+0.02}_{-0.02}$	$1.89^{+0.02}_{-0.03}$
$\text{norm}_{\text{bb}}[10^{-2}]$	$8.01^{+0.04}_{-0.04}$	$8.38^{+0.05}_{-0.05}$	$8.41^{+0.06}_{-0.03}$	$8.65^{+0.10}_{-0.11}$
$E_{\text{Disk}}[\text{keV}]$	$6.62^{+0.02}_{-0.01}$	$6.63^{+0.02}_{-0.02}$	$6.64^{+0.02}_{-0.03}$	$6.62^{+0.04}_{-0.06}$
$R_{\text{in}}[\text{GM}/c^2]$	$8.5^{+0.4}_{-0.4}$	$8.8^{+0.5}_{-0.6}$	$9.9^{+0.7}_{-0.7}$	$10.1^{+1.3}_{-1.3}$
Incl [deg]	$90.0_{-5.3}$	$90.0_{-5.6}$	$90.0_{-8.0}$	$90.0_{-11.2}$
$\text{norm}_{\text{Disk}}[10^{-3}]$	$34.70^{+1.08}_{-0.77}$	$36.53^{+1.26}_{-1.28}$	$35.84^{+1.49}_{-1.47}$	$36.77^{+2.51}_{-2.37}$
red. χ^2 (1511 dof)	1.3507	1.2883	1.1803	1.1068

Table 4.10: Best-fit parameters when the simulated DISKLINE data was fitted with the continuum model and the relativistic DISKLINE model. Reported are the results for region 1 (no columns excluded), region 2 (one column excluded), region 3 (three columns excluded) and region 4 (five columns excluded) for the different input fluxes. When no error is given the calculation was not possible.

Parameter	Region 1	Region 2	Region 3	Region 4
$1 \times 10^{-9} \text{ erg s}^{-1} \text{ cm}^{-2}$				
$T_{\text{Dbb}}[\text{keV}]$	$0.90^{+0.04}_{-0.03}$	$0.91^{+0.04}_{-0.04}$	$0.94^{+0.05}_{-0.05}$	$0.87^{+0.08}_{-0.06}$
norm_{Dbb}	$33.9^{+5.4}_{-4.3}$	$33.6^{+6.1}_{-5.0}$	$29.1^{+8.8}_{-6.2}$	$41.5^{+14.5}_{-12.4}$
$kT[\text{keV}]$	$1.90^{+0.03}_{-0.03}$	$1.91^{+0.04}_{-0.04}$	$1.91^{+0.06}_{-0.08}$	$1.79^{+0.07}_{-0.04}$
$\text{norm}_{\text{bb}}[10^{-2}]$	$0.77^{+0.01}_{-0.01}$	$0.80^{+0.01}_{-0.01}$	$0.79^{+0.03}_{-0.02}$	$0.82^{+0.02}_{-0.03}$
$E_{\text{Disk}}[\text{keV}]$	$6.74^{+0.06}_{-0.05}$	$6.73^{+0.06}_{-0.07}$	$6.73^{+0.07}_{-0.10}$	$6.72^{+0.08}_{-0.09}$
$R_{\text{in}}[\text{GM}/c^2]$	$6.5^{+7.7}_{-0.5}$	$6.1^{+14.5}_{-0.1}$	$6.0^{+24.2}_{-0.0}$	$21.2^{+16.1}_{-15.2}$
Incl [deg]	$27.5^{+3.4}_{-3.9}$	$28.4^{+4.2}_{-4.2}$	$29.0^{+5.5}_{-4.9}$	$31.1^{+10.4}_{-5.9}$
$\text{norm}_{\text{Disk}}[10^{-3}]$	$0.90^{+0.11}_{-0.16}$	$0.99^{+0.11}_{-0.26}$	$1.16^{+0.16}_{-0.38}$	$0.93^{+0.36}_{-0.19}$
red. χ^2 (1511 dof)	1.0171	0.9703	1.0450	1.1123
$4.5 \times 10^{-9} \text{ erg s}^{-1} \text{ cm}^{-2}$				
$T_{\text{Dbb}}[\text{keV}]$	$0.96^{+0.01}_{-0.02}$	$0.94^{+0.02}_{-0.02}$	$0.99^{+0.03}_{-0.03}$	$0.99^{+0.04}_{-0.02}$
norm_{Dbb}	$124.4^{+8.5}_{-7.6}$	$135.3^{+11.3}_{-10.0}$	$110.9^{+13.4}_{-13.3}$	$118.1^{+20.7}_{-17.6}$
$kT[\text{keV}]$	$1.98^{+0.02}_{-0.02}$	$1.96^{+0.02}_{-0.02}$	$2.00^{+0.03}_{-0.03}$	$1.97^{+0.05}_{-0.05}$
$\text{norm}_{\text{bb}}[10^{-2}]$	$3.46^{+0.02}_{-0.02}$	$3.66^{+0.03}_{-0.02}$	$3.59^{+0.04}_{-0.04}$	$3.67^{+0.04}_{-0.06}$
$E_{\text{Disk}}[\text{keV}]$	$6.68^{+0.06}_{-0.02}$	$6.68^{+0.03}_{-0.02}$	$6.66^{+0.08}_{-0.04}$	$6.71^{+0.07}_{-0.07}$
$R_{\text{in}}[\text{GM}/c^2]$	$7.7^{+2.0}_{-1.7}$	$23.6^{+6.5}_{-5.3}$	$7.8^{+3.9}_{-1.8}$	$6.7^{+15.2}_{-0.7}$
Incl [deg]	$30.4^{+1.5}_{-3.8}$	$30.6^{+1.9}_{-2.1}$	$32.2^{+2.2}_{-4.5}$	$30.2^{+3.4}_{-4.7}$
$\text{norm}_{\text{Disk}}[10^{-3}]$	$4.18^{+0.35}_{-0.31}$	$3.58^{+0.25}_{-0.26}$	$4.82^{+0.50}_{-1.38}$	$5.26^{+0.51}_{-1.13}$
red. χ^2 (1511 dof)	1.0104	1.0694	1.0344	1.1008
$1 \times 10^{-8} \text{ erg s}^{-1} \text{ cm}^{-2}$				
$T_{\text{Dbb}}[\text{keV}]$	$0.98^{+0.02}_{-0.01}$	$0.98^{+0.02}_{-0.01}$	$0.99^{+0.02}_{-0.02}$	$1.02^{+0.03}_{-0.03}$
norm_{Dbb}	$247.0^{+11.0}_{-10.3}$	$259.7^{+13.4}_{-12.9}$	$251.7^{+20.4}_{-17.8}$	$230.1^{+26.9}_{-23.7}$
$kT[\text{keV}]$	$2.04^{+0.01}_{-0.02}$	$2.03^{+0.02}_{-0.01}$	$2.02^{+0.02}_{-0.02}$	$2.02^{+0.04}_{-0.03}$
$\text{norm}_{\text{bb}}[10^{-2}]$	$7.73^{+0.03}_{-0.03}$	$8.11^{+0.04}_{-0.04}$	$8.09^{+0.05}_{-0.06}$	$8.17^{+0.09}_{-0.10}$
$E_{\text{Disk}}[\text{keV}]$	$6.67^{+0.02}_{-0.03}$	$6.68^{+0.02}_{-0.05}$	$6.69^{+0.04}_{-0.07}$	$6.65^{+0.05}_{-0.05}$
$R_{\text{in}}[\text{GM}/c^2]$	$6.0^{+1.3}_{-0.0}$	$6.0^{+4.2}_{-0.0}$	$6.0^{+4.0}_{-0.0}$	$6.0^{+6.9}_{-0.0}$
Incl [deg]	$31.1^{+1.5}_{-1.4}$	$31.0^{+2.0}_{-1.7}$	$30.6^{+3.1}_{-2.6}$	$32.9^{+2.5}_{-3.1}$
$\text{norm}_{\text{Disk}}[10^{-3}]$	$10.02^{+0.31}_{-0.42}$	$10.68^{+0.44}_{-0.62}$	$10.73^{+0.65}_{-0.93}$	$12.17^{+0.93}_{-0.96}$
red. χ^2 (1511 dof)	0.9929	1.0048	1.0471	1.0294

Table 4.11: Best-fit parameters when the simulated DISKLINE data was fitted with the continuum model and a Gaussian line profile. Reported are the results for region 1 (no columns excluded), region 2 (one column excluded), region 3 (three columns excluded) and region 4 (five columns excluded) for the different input fluxes. When no error is given the calculation was not possible.

Parameter	Region 1	Region 2	Region 3	Region 4
$1 \times 10^{-9} \text{ erg s}^{-1} \text{ cm}^{-2}$				
$T_{\text{Dbb}}[\text{keV}]$	$0.85^{+0.03}_{-0.02}$	$0.86^{+0.04}_{-0.03}$	$0.90^{+0.07}_{-0.05}$	$0.86^{+0.09}_{-0.07}$
norm_{Dbb}	$42.2^{+6.1}_{-5.4}$	$41.3^{+7.1}_{-5.8}$	$34.3^{+9.5}_{-8.0}$	$42.1^{+17.0}_{-13.1}$
$kT[\text{keV}]$	$1.85^{+0.03}_{-0.03}$	$1.86^{+0.03}_{-0.03}$	$1.86^{+0.06}_{-0.04}$	$1.79^{+0.06}_{-0.05}$
$\text{norm}_{\text{bb}}[10^{-2}]$	$0.79^{+0.01}_{-0.01}$	$0.82^{+0.01}_{-0.01}$	$0.80^{+0.02}_{-0.02}$	$0.82^{+0.02}_{-0.03}$
$E_{\text{Gau}}[\text{keV}]$	$6.69^{+0.03}_{-0.03}$	$6.68^{+0.04}_{-0.03}$	$6.67^{+0.05}_{-0.06}$	$6.69^{+0.08}_{-0.10}$
$\sigma_{\text{Gau}}[\text{keV}]$	$0.23^{+0.03}_{-0.03}$	$0.25^{+0.04}_{-0.04}$	$0.29^{+0.08}_{-0.06}$	$0.30^{+0.12}_{-0.09}$
$\text{norm}_{\text{Gau}}[10^{-3}]$	$0.60^{+0.01}_{-0.01}$	$0.67^{+0.10}_{-0.10}$	$0.87^{+0.21}_{-0.17}$	$0.91^{+0.33}_{-0.25}$
red. χ^2 (1512 dof)	1.0426	0.9873	1.0523	1.1157
$4.5 \times 10^{-9} \text{ erg s}^{-1} \text{ cm}^{-2}$				
$T_{\text{Dbb}}[\text{keV}]$	$0.91^{+0.01}_{-0.02}$	$0.92^{+0.02}_{-0.02}$	$0.94^{+0.03}_{-0.03}$	$0.92^{+0.04}_{-0.03}$
norm_{Dbb}	$149.7^{+10.1}_{-9.1}$	$145.8^{+11.7}_{-10.4}$	$135.1^{+16.1}_{-14.3}$	$148.6^{+24.4}_{-21.5}$
$kT[\text{keV}]$	$1.93^{+0.01}_{-0.02}$	$1.94^{+0.02}_{-0.01}$	$1.94^{+0.02}_{-0.03}$	$1.90^{+0.03}_{-0.03}$
$\text{norm}_{\text{bb}}[10^{-2}]$	$3.53^{+0.02}_{-0.01}$	$3.69^{+0.02}_{-0.02}$	$3.67^{+0.04}_{-0.03}$	$3.77^{+0.05}_{-0.05}$
$E_{\text{Gau}}[\text{keV}]$	$6.67^{+0.02}_{-0.01}$	$6.67^{+0.02}_{-0.02}$	$6.67^{+0.03}_{-0.02}$	$6.69^{+0.03}_{-0.04}$
$\sigma_{\text{Gau}}[\text{keV}]$	$0.24^{+0.02}_{-0.01}$	$0.25^{+0.02}_{-0.02}$	$0.26^{+0.03}_{-0.03}$	$0.24^{+0.03}_{-0.03}$
$\text{norm}_{\text{Gau}}[10^{-3}]$	$2.90^{+0.18}_{-0.18}$	$3.19^{+0.22}_{-0.23}$	$3.41^{+0.34}_{-0.33}$	$3.54^{+0.46}_{-0.43}$
red. χ^2 (1512 dof)	1.1067	1.1314	1.0657	1.1203
$1 \times 10^{-8} \text{ erg s}^{-1} \text{ cm}^{-2}$				
$T_{\text{Dbb}}[\text{keV}]$	$0.93^{+0.01}_{-0.01}$	$0.93^{+0.01}_{-0.01}$	$0.94^{+0.01}_{-0.02}$	$0.97^{+0.03}_{-0.03}$
norm_{Dbb}	$296.5^{+14.0}_{-11.9}$	$312.6^{+16.0}_{-15.4}$	$302.4^{+24.6}_{-21.2}$	$275.9^{+32.1}_{-29.2}$
$kT[\text{keV}]$	$1.97^{+0.01}_{-0.01}$	$1.97^{+0.01}_{-0.01}$	$1.95^{+0.02}_{-0.01}$	$1.96^{+0.02}_{-0.03}$
$\text{norm}_{\text{bb}}[10^{-2}]$	$7.88^{+0.03}_{-0.03}$	$8.26^{+0.04}_{-0.03}$	$8.25^{+0.05}_{-0.05}$	$8.35^{+0.09}_{-0.06}$
$E_{\text{Gau}}[\text{keV}]$	$6.65^{+0.01}_{-0.01}$	$6.65^{+0.02}_{-0.01}$	$6.65^{+0.02}_{-0.02}$	$6.63^{+0.02}_{-0.03}$
$\sigma_{\text{Gau}}[\text{keV}]$	$0.26^{+0.01}_{-0.01}$	$0.26^{+0.01}_{-0.01}$	$0.27^{+0.02}_{-0.02}$	$0.27^{+0.02}_{-0.02}$
$\text{norm}_{\text{Gau}}[10^{-3}]$	$6.75^{+0.27}_{-0.29}$	$7.28^{+0.34}_{-0.34}$	$7.45^{+0.51}_{-0.54}$	$8.64^{+0.81}_{-0.78}$
red. χ^2 (1512 dof)	1.2185	1.1847	1.1520	1.0820

Table 4.12: Parameters of the PHABS(DISKBB + BBODY + DISKLINE) model as reported by Cackett et al. (2010) (Model 1) and the TBABS(DISKBB + BBODYRAD + GAUSSIAN) model given by Ng et al. (2010) (Model 2). Furthermore, the fit results of both models and both extraction regions are given. The simulation is based on Model 1.

Parameter	Model 1			Model 2		
	Cackett	24col	16-4col	Ng	24col	16-4col
phabs[$10^{22}/\text{cm}^2$]	0.35	0.35	0.35			
tbabs[$10^{22}/\text{cm}^2$]				0.36	0.36	0.36
T_{Dbb} [keV]	0.99	$0.99^{+0.01}_{-0.02}$	$0.97^{+0.01}_{-0.03}$	0.91	$0.98^{+0.02}_{-0.01}$	$0.97^{+0.03}_{-0.03}$
norm _{Dbb}	175	207^{+11}_{-11}	272^{+30}_{-26}	233	209^{+12}_{-11}	274^{+30}_{-28}
kT_{bb} [keV]	1.81	$1.86^{+0.02}_{-0.02}$	$1.80^{+0.04}_{-0.03}$			
norm _{bb} [10^{-2}]	3.13	$3.54^{+0.04}_{-0.04}$	$4.55^{+0.10}_{-0.10}$			
kT_{bbrad} [keV]				1.64	$1.85^{+0.02}_{-0.02}$	$1.80^{+0.04}_{-0.03}$
norm _{bbrad}				33.7	$23.4^{+1.3}_{-1.3}$	$33.6^{+3.3}_{-3.4}$
E_{Disk} [keV]	6.97	$7.00^{+0.09}_{-0.12}$	$7.20^{+0.12}_{-0.18}$			
R_{in} [GM/ c^2]	14.0	$13.9^{+2.3}_{-1.8}$	$10.5^{+2.5}_{-1.3}$			
R_{out} [GM/ c^2]	1000	1000	1000			
Incl [deg]	13.0	$10.4^{+4.4}_{-3.4}$	$7.1^{+4.4}_{-7.1}$			
norm _{Disk} [10^{-2}]	0.16	$0.16^{+0.02}_{-0.02}$	$0.26^{+0.07}_{-0.05}$			
Betor	-3.7	-3.7	-3.7			
E_{Gau} [keV]				6.58	$6.58^{+0.04}_{-0.04}$	$6.57^{+0.07}_{-0.07}$
σ_{Gau} [keV]				0.25	$0.27^{+0.04}_{-0.04}$	$0.34^{+0.09}_{-0.08}$
norm _{Gau} [10^{-3}]				1.57	$1.57^{+0.25}_{-0.24}$	$2.65^{+0.79}_{-0.65}$
χ^2		1503	1600		1511	1600
d.o.f.		1511	1511		1512	1512

Table 4.13: Parameters of the PHABS(DISKBB + BBODY + DISKLINE) model as reported by Cackett et al. (2010) (Model 1) and the TBABS(DISKBB + BBODYRAD + GAUSSIAN) model given by Ng et al. (2010) (Model 2). Furthermore, the fit results of both models and both extraction regions are given. The simulations is based on Model 2.

Parameter	Model 1			Model 2		
	Cackett	24col	16-4col	Ng	24col	16-4col
phabs[$10^{22}/\text{cm}^2$]	0.35	0.35	0.35			
tbabs[$10^{22}/\text{cm}^2$]				0.36	0.36	0.36
T_{Dbb} [keV]	0.99	$0.91^{+0.02}_{-0.01}$	$0.90^{+0.03}_{-0.03}$	0.91	$0.91^{+0.02}_{-0.01}$	$0.92^{+0.03}_{-0.03}$
norm _{Dbb}	175	242^{+15}_{-13}	309^{+36}_{-31}	233	241^{+14}_{-14}	296^{+39}_{-36}
kT_{bb} [keV]	1.81	$1.67^{+0.02}_{-0.01}$	$1.64^{+0.04}_{-0.03}$			
norm _{bb} [10^{-2}]	3.13	$3.14^{+0.03}_{-0.04}$	$4.03^{+0.08}_{-0.10}$			
kT_{bbrad} [keV]				1.64	$1.68^{+0.01}_{-0.02}$	$1.65^{+0.03}_{-0.03}$
norm _{bbrad} [10^{-2}]				33.7	$30.86^{+1.46}_{-1.48}$	$41.9^{+4.0}_{-4.3}$
E_{Disk} [keV]	6.97	$6.93^{+0.07}_{-0.11}$	$6.89^{+0.33}_{-0.20}$			
R_{in} [GM/ c^2]	14.0	$16.6^{+4.5}_{-2.0}$	$16.1^{+11.6}_{-5.7}$			
R_{out} [GM/ c^2]	400	400	400			
Incl [deg]	13.0	$6.1^{+4.1}_{-3.5}$	$11.6^{+7.1}_{-7.3}$			
norm _{Disk} [10^{-2}]	0.16	$0.14^{+0.01}_{-0.02}$	$0.21^{+0.06}_{-0.04}$			
Betor	-3.7	-3.7	-3.7			
E_{Gau} [keV]				6.58	$6.54^{+0.03}_{-0.03}$	$6.54^{+0.07}_{-0.06}$
σ_{Gau} [keV]				0.25	$0.22^{+0.03}_{-0.04}$	$0.34^{+0.12}_{-0.09}$
norm _{Gau} [10^{-3}]				1.57	$1.46^{+0.20}_{-0.18}$	$2.63^{+0.91}_{-0.66}$
χ^2		1461	1473		1461	1471
d.o.f.		1511	1511		1512	1512

Table 4.14: Parameters of the PHABS(BBODY + COMP_{TT} + DISKLINE) model as reported by di Salvo et al. (2009) (Model 1) and the TBABS(DISKBB + BBODYRAD + GAUSSIAN) model given by Ng et al. (2010) (Model 2). Furthermore, the fit results of both models and both extraction regions are given. The simulation is based on Model 1.

Parameter	Model 1			Model 2		
	DiSalvo	13col	15-7col	Ng	13col	15-7col
phabs[$10^{22}/\text{cm}^2$]	1.8	1.8	1.8			
tbabs[$10^{22}/\text{cm}^2$]				1.5	1.5	1.5
T_{Dbb} [keV]				0.95	$0.85^{+0.01}_{-0.00}$	$0.90^{+0.02}_{-0.01}$
norm _{Dbb}				231	406^{+7}_{-6}	331^{+18}_{-18}
kT_{bb} [keV]	0.55	$0.52^{+0.00}_{-0.00}$	$0.50^{+0.02}_{-0.01}$			
norm _{bb} [10^{-2}]	3.10	$2.60^{+0.01}_{-0.01}$	$3.70^{+0.10}_{-0.10}$			
kT_{bbrad} [keV]				1.61	$2.72^{+0.01}_{-0.01}$	$2.78^{+0.03}_{-0.03}$
norm _{bbrad}				79.0	$12.9^{+0.1}_{-0.1}$	$12.2^{+0.5}_{-0.5}$
$T_{0,\text{compTT}}$ [keV]	1.26	$0.001^{+0.003}$	$1.03^{+0.07}_{-0.08}$			
kT_{compTT} [keV]	4.80	$3.51^{+0.01}_{-0.03}$	$14.68^{+14.35}_{-6.59}$			
τ_{compTT}	6.3	$9.4^{+0.2}_{-0.1}$	$4.9^{+0.7}_{-0.3}$			
norm _{compTT}	0.20	$2.66^{+0.04}_{-0.09}$	$0.12^{+0.05}_{-0.04}$			
E_{Disk} [keV]	6.66	$6.65^{+0.01}_{-0.01}$	$6.62^{+0.03}_{-0.03}$			
R_{in} [GM/ c^2]	14.0	$15.7^{+3.6}_{-4.1}$	$14.2^{+7.4}_{-4.5}$			
R_{out} [GM/ c^2]	3300	3300	3300			
Incl [deg]	39.0	$38.6^{+1.8}_{-1.5}$	$54.3^{+11.8}_{-6.2}$			
norm _{Disk} [10^{-2}]	0.36	$0.32^{+0.01}_{-0.02}$	$0.61^{+0.07}_{-0.07}$			
Betor	-2.27	-2.27	-2.27			
E_{Gau} [keV]				6.56	$6.65^{+0.02}_{-0.00}$	6.57
σ_{Gau} [keV]				0.44	$0.25^{+0.02}_{-0.01}$	$0.38^{+0.05}_{-0.05}$
norm _{Gau} [10^{-3}]				6.10	$2.58^{+0.12}_{-0.12}$	$4.61^{+0.69}_{-0.61}$
χ^2		1514	1557		1996	1780
d.o.f.		1509	1509		1512	1513

Table 4.15: Parameters of the PHABS(BBODY + COMPTT + DISKLINE) model as reported by di Salvo et al. (2009) (Model 1) and the TBABS(DISKBB + BBODYRAD + GAUSSIAN) model given by Ng et al. (2010) (Model 2). Furthermore, the fit results of both models and both extraction regions are given. The simulation is based on Model 2.

Parameter	Model 1			Model 2		
	DiSalvo	13col	15-7col	Ng	13col	15-7col
phabs[$10^{22}/\text{cm}^2$]	1.8	1.8	1.8			
tbabs[$10^{22}/\text{cm}^2$]				1.5	1.5	1.5
T_{Dbb} [keV]				0.95	$0.93^{+0.00}_{-0.00}$	$1.03^{+0.05}_{-0.04}$
norm_{Dbb}				231	304^{+9}_{-10}	208^{+30}_{-30}
kT_{bb} [keV]	0.55	$0.45^{+0.01}_{-0.01}$	$0.47^{+0.02}_{-0.04}$			
norm_{bb} [10^{-2}]	3.10	$3.30^{+0.03}_{-0.03}$	$3.39^{+0.23}_{-0.19}$			
kT_{bbrad} [keV]				1.61	$1.67^{+0.00}_{-0.01}$	$1.67^{+0.03}_{-0.02}$
$\text{norm}_{\text{bbrad}}$				79.0	$70.2^{+1.1}_{-1.1}$	$66.6^{+6.1}_{-7.1}$
$T_{0,\text{compTT}}$ [keV]	1.26	$0.81^{+0.03}_{-0.01}$	$0.88^{+0.24}_{-0.08}$			
kT_{compTT} [keV]	4.80	$2.00^{+0.01}$	$2.00^{+0.83}$			
τ_{compTT}	6.3	$8.3^{+0.0}_{-0.1}$	$7.8^{+0.1}_{-3.6}$			
$\text{norm}_{\text{compTT}}$	0.20	$0.81^{+0.00}_{-0.02}$	$0.83^{+0.05}_{-0.44}$			
E_{Disk} [keV]	6.66	$6.49^{+0.01}_{-0.01}$	$6.48^{+0.04}_{-0.03}$			
R_{in} [GM/ c^2]	14.0	$6.3^{+0.4}$	$17.7^{+4.4}_{-3.7}$			
R_{out} [GM/ c^2]	3300	3300	3300			
Incl [deg]	39.0	$90.0_{-7.4}$	$90.0_{-15.2}$			
$\text{norm}_{\text{Disk}}$ [10^{-2}]	0.36	$1.02^{+0.03}_{-0.03}$	$0.90^{+0.09}_{-0.07}$			
Betor	-2.27	-2.27	-2.27			
E_{Gau} [keV]				6.56	$6.55^{+0.01}_{-0.02}$	$6.49^{+0.03}_{-0.04}$
σ_{Gau} [keV]				0.44	$0.43^{+0.02}_{-0.01}$	$0.54^{+0.05}_{-0.05}$
norm_{Gau} [10^{-3}]				6.10	$5.32^{+0.23}_{-0.22}$	$9.01^{+1.26}_{-1.06}$
χ^2		1788	1581		1583	1566
d.o.f.		1509	1509		1512	1512

Table 4.16: Parameters of the vPHABS(DISKBB + BBODYRAD + COMPTT + DISKLINE) model as reported by Pandel et al. (2008) (Model 1) and the TBABS(DISKBB + BBODYRAD + GAUSSIAN) model given by Ng et al. (2010) (Model 2). Furthermore, the fit results of both models and both extraction regions are given. The simulation is based on Model 1.

Parameter	Model 1			Model 2		
	Pandel	15col	15-1col	Ng	15col	15-1col
vphabs						
nH[$10^{22}/\text{cm}^2$]	0.383	0.383	0.383			
O	1.27	1.27	1.27			
Ne	1.2	1.2	1.2			
Si	2.0	2.0	2.0			
Fe	1.47	1.47	1.47			
tbabs[$10^{22}/\text{cm}^2$]				0.238	0.238	0.238
T_{Dbb} [keV]	0.78	$0.78^{+0.01}_{-0.01}$	$0.77^{+0.02}_{-0.02}$	0.8	$0.81^{+0.00}_{-0.01}$	$0.82^{+0.00}_{-0.00}$
norm _{Dbb}	200	297^{+20}_{-24}	312^{+32}_{-25}	177	227^{+0}_{-3}	233^{+1}_{-1}
kT_{bb} [keV]						
norm _{bb} [10^{-2}]						
kT_{bbrad} [keV]	0.177	0.242	0.242	1.86	$1.91^{+0.00}_{-0.00}$	$1.91^{+0.04}_{-0.03}$
norm _{bbrad}	29000	10410	10410	8.2	$5.2^{+0.0}_{-0.0}$	$5.5^{+0.1}_{-0.1}$
$T_{0,\text{compTT}}$ [keV]	1.45	$1.42^{+0.04}_{-0.04}$	$1.40^{+0.17}_{-0.15}$			
kT_{compTT} [keV]	9.0	$6.0^{+140.0}_{-2.1}$	$6.1^{+173.9}_{-2.7}$			
τ_{compTT}	1.3	$2.3^{+27.3}_{-1.2}$	$2.3^{+8.4}_{-1.2}$			
norm _{compTT}	0.009	$0.020^{+0.032}_{-0.011}$	$0.021^{+0.132}_{-0.015}$			
E_{Disk} [keV]	7.06	$7.05^{+0.04}_{-0.04}$	$7.05^{+0.04}_{-0.04}$			
R_{in} [GM/ c^2]	13.3	$8.4^{+7.2}_{-2.4}$	$13.8^{+5.1}_{-7.8}$			
R_{out} [GM/ c^2]	690	690	690			
Incl [deg]	64.0	$60.3^{+18.2}_{-4.8}$	$71.5^{+18.5}_{-15.2}$			
norm _{Disk} [10^{-2}]	0.091	$0.15^{+0.02}_{-0.02}$	$0.16^{+0.02}_{-0.03}$			
Betor	-2.32	-2.32	-2.32			
E_{Gau} [keV]				6.97	$6.97^{+0.00}_{-0.38}$	$6.97^{+0.00}_{-0.38}$
σ_{Gau} [keV]				0.6	$0.70^{+0.04}_{-0.04}$	$0.68^{+0.04}_{-0.04}$
norm _{Gau} [10^{-3}]				0.3	$1.11^{+0.06}_{-0.05}$	$1.21^{+0.06}_{-0.07}$
χ^2		1553	1475		1633	1527
d.o.f.		1509	1509		1512	1512

Table 4.17: Parameters of the vPHABS(DISKBB + BBODYRAD + COMPTT + DISKLINE) model as reported by Pandel et al. (2008) (Model 1) and the TBABS(DISKBB + BBODYRAD + GAUSSIAN) model given by Ng et al. (2010) (Model 2). Furthermore, the fit results of both models and both extraction regions are given. The simulation is based on Model 2.

Parameter	Model 1			Model 2		
	Pandel	15col	15-1col	Ng	15col	15-1col
vphabs						
nH[$10^{22}/\text{cm}^2$]	0.383	0.383	0.383			
O	1.27	1.27	1.27			
Ne	1.2	1.2	1.2			
Si	2.0	2.0	2.0			
Fe	1.47	1.47	1.47			
tbabs[$10^{22}/\text{cm}^2$]				0.238	0.238	0.238
T_{Dbb} [keV]	0.78	$0.78^{+0.01}_{-0.02}$	$0.78^{+0.02}_{-0.02}$	0.8	$0.79^{+0.01}_{-0.00}$	$0.79^{+0.02}_{-0.00}$
norm _{Dbb}	200	219^{+20}_{-14}	230^{+28}_{-21}	177	185^{+7}_{-8}	191^{+9}_{-12}
kT_{bb} [keV]						
norm _{bb} [10^{-2}]						
kT_{bbrad} [keV]	0.177	0.200	0.201	1.86	$1.86^{+0.01}_{-0.01}$	$1.86^{+0.02}_{-0.01}$
norm _{bbrad}	29000	41835	42067	8.2	$8.0^{+0.2}_{-0.4}$	$8.4^{+0.2}_{-0.4}$
$T_{0,\text{compTT}}$ [keV]	1.45	$1.69^{+0.06}_{-0.15}$	$1.67^{+0.20}_{-0.17}$			
kT_{compTT} [keV]	9.0	$8.5^{+16.5}_{-0.3}$	$8.6^{+44.0}_{-0.3}$			
τ_{compTT}	1.3	$0.5^{+0.73}_{-0.5}$	$0.6^{+7.1}_{-0.4}$			
norm _{compTT}	0.009	$0.017^{+0.051}_{-0.001}$	$0.017^{+2.883}_{-0.000}$			
E_{Disk} [keV]	7.06	$7.04^{+0.17}_{-0.16}$	$6.97^{+0.22}_{-0.14}$			
R_{in} [GM/ c^2]	13.3	$6.0^{+10.4}$	$6.0^{+689.6}$			
R_{out} [GM/ c^2]	690	690	690			
Incl [deg]	64.0	$58.3^{+31.7}_{-9.0}$	$63.1^{+26.9}_{-46.7}$			
norm _{Disk} [10^{-2}]	0.091	$0.041^{+0.034}_{-0.063}$	$0.047^{+0.043}_{-0.041}$			
Betor	-2.32	-2.32	-2.32			
E_{Gau} [keV]				6.97	$7.12^{+0.22}_{-0.32}$	$6.99^{+0.24}_{-0.41}$
σ_{Gau} [keV]				0.6	$0.63^{+0.51}_{-0.30}$	$0.56^{+0.67}_{-0.31}$
norm _{Gau} [10^{-3}]				0.30	$0.27^{+0.13}_{-0.14}$	$0.25^{+0.58}_{-0.14}$
χ^2		1511	1454		1512	1527
d.o.f.		1509	1509		1512	1512

CHAPTER 5

EPIC-PN BACKGROUND TEMPLATE FOR TIMING MODE OBSERVATIONS

In imaging modes of detectors based on CCDs it is common to define a region on the detector from which the observational background spectrum is extracted. It is important to choose a region which is not contaminated by the observed or by any other source. However, this possibility is not given for observations performed in the fast read-out mode of the EPIC-PN, the Timing Mode (TM).

In the following Chapter first the problem of the background extraction will be discussed and the different sources of background will be explained. Furthermore, an alternative method to obtain a background spectrum for TM observations will be introduced, namely Blank Field (BF) observations. This method was developed in the frame of this work in cooperation with Matteo Guainazzi of the *XMM-Newton* Science Data Center in Madrid.

Finally, the testing and classification of the blank field candidates will be presented as well as the first results of applying the obtained blank field spectra on a sample of observations.

5.1 Motivation and Goal

Typically only bright sources are observed in Timing Mode, for which the background should be negligible. However, there are some kind of sources for which a proper background spectrum is important. On the one hand, there are highly obscured sources in which nearly all source photons are absorbed below around 2 keV and therefore background dominated in this energy region. On the other hand, also soft sources with very low flux above approximately 5 keV are observed which have, due to the low flux, a significant background contribution in the high energy part of the spectrum.

Since the Timing Mode of the EPIC-PN does not offer a region without any source contamination, as it can be seen on the left side of Figure 5.1, the only way

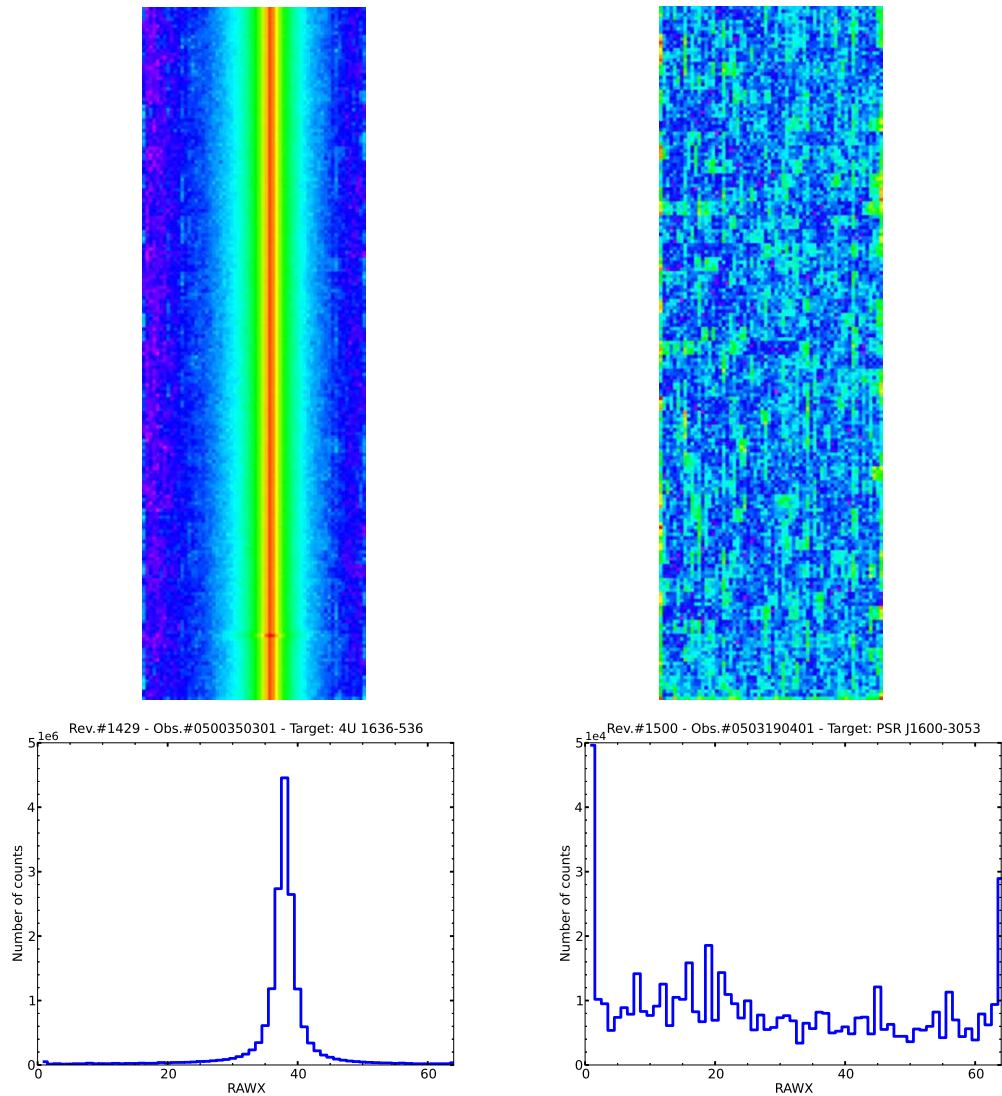


Figure 5.1: *Upper panel:* Shown are images of EPIC-PN Timing Mode observations. On the left side an observation with a source in the central region can be seen whereas on the right side a blank field candidate is given in which no apparent source contribution is present. *Lower panel:* The corresponding *RawX* profiles are shown in which all counts in one detector column are summed up.

to obtain an uncontaminated background spectrum is to extract it from a so-called blank field observation in which no significant source is present. Such observations are usually not performed on purpose, but can occur if the source of interest is for example in a quiescent state. Therefore, no significant amount of source photons can be observed as shown on the right side of Figure 5.1. The observed events are homogeneously distributed which is a clear evidence that no source is present.

However, this simple test is not sufficient to define an observation as uncontaminated. Several tests are necessary to proof if a significant source contribution is present or not.

The goal of this work is to study the background for Timing Mode observations and eventually offer the users community a possibility to obtain a background spectrum which is not contaminated by any kind of source. This could be achieved either by a background spectrum or an event list, however, both are based on blank field observations. To account for different observational conditions a template is provided from which the user can extract a background by themselves.

5.2 Sources of background

First of all, the different sources which contribute to the background of the EPIC-PN will be discussed. The following discussion is based on the work of the background analysis working group of *XMM-Newton*¹, whereas an overview of the background measurements with the EPIC detectors is given by Lumb et al. (2002).

5.2.1 Photons

Real-life observations always include astrophysical background photons which will be detected in addition to the photons of the source of interest. The background photons originate from close-by stars or diffuse X-ray emission fed by distant active galactic nuclei, the galactic disk or the galactic halo. Other sources of background photons are reflections on the mirrors from outside the field of view or the effect of Solar Wind Charge Exchange (SWCX, e.g. Snowden et al. 2004; Carter & Sembay 2008; Carter et al. 2011).

Since the background spectrum induced by photons has a thermal origin, the spectrum can be modeled phenomenologically by a blackbody to account for energies below 1 keV. A power-law describes the spectrum at high energies, as it can be seen on the left side of Figure 5.2 which suggests a non-thermal origin. However, this background component varies along the sky and is different from observation to observation.

¹http://xmm2.esac.esa.int/external/xmm_sw_cal/background/index.shtml

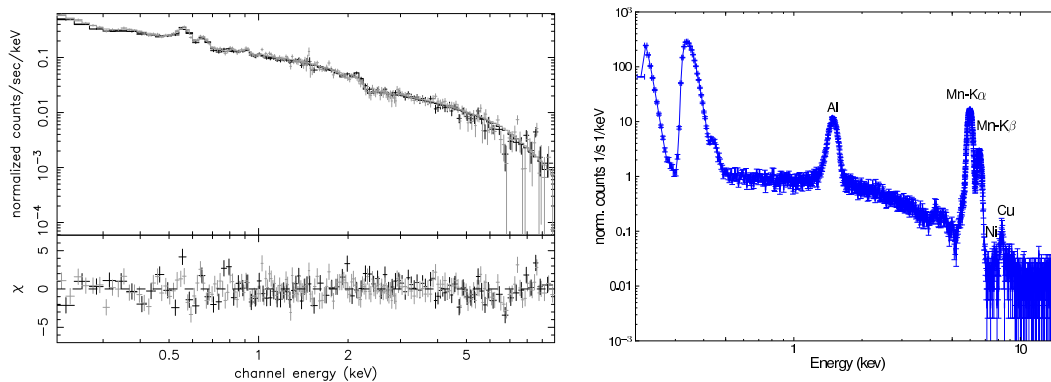


Figure 5.2: *Left panel:* Shown is the best fit model and residuals of the spectrum of the diffuse X-ray emission component of the background, Lumb et al. (2002). *Right panel:* Internal background spectrum with a ^{55}Fe calibration source included (CalClosed observation with the ID 0119700301). In addition to the fluorescence lines induced by the detector material, like the Al-K α at ~ 1.5 keV, Ni-K α at ~ 7.5 keV and the Cu-K α at ~ 8.0 keV, the Mn-K β line at about 6.4 keV originating from the calibration source is present.

5.2.2 Internal background

The different components of internal background were studied by Freyberg et al. (2004). They found that a significant part of internal background originates from fluorescence lines which are produced in the detector material, namely aluminum, copper, nickel and molybdenum.

On the right panel of Figure 5.2 a spectrum is shown obtained from a TM observation performed with the *CalClosed* position of the filter wheel. In this position the detector is exposed to an ^{55}Fe calibration source which results in a Mn-K β line in the spectrum at about 6.4 keV. This spectral line overlaps the spectrum of the internal background, however, the most prominent features are still visible and above 7 keV the spectrum is not affected by the calibration source.

Freyberg et al. (2004) found that the internal background of the EPIC-PN has a rate of around $0.1 \text{ cts s}^{-1} \text{ keV}^{-1}$ in the energy range of 2 keV–7 keV, whereas the most prominent features are the Al-K α (at ~ 1.5 keV), Ni-K α (at ~ 7.5 keV) and the Cu-K α (at ~ 8.0 keV) lines. Furthermore, at the low energy end of the spectrum the noise peak is dominating the spectrum, this is caused by summing up the charge of ten pixels (see Section 1.3.3).

In addition, soft protons originating from solar flares can interact with the detector and produce a continuum spectrum which can be modeled with a broken power-law. However, the resulting spectral shape changes from observation to observation, since the flares strongly depend on the solar activity.

5.3 Blank Field Inspection

To perform a proper blank field inspection, the different components which contribute to the background have to be known. Otherwise, spectral features cannot be assigned to the right physical origin. Considering this, blank field observations can be accurately examined. Therefore, first a sample of observations has to be obtained which can be deeper investigated.

5.3.1 The Blank Field Observation Sample

As a starting point, the *XMM-Newton* Science Archive² (XSA) was checked for all public available EPIC-PN observations performed in Timing Mode. As of the 13th November 2013 there had been 378 observations. The data were downloaded in ODF (Observation Data Files) format and processed using the standard SAS tool EPPROC³ and EPFAST⁴ to produce a CTI (Charge Transfer Inefficiency) corrected event list.

To obtain a first, rough classification of the observations, a *RawX* profile was created for each observation. All events in one detector column were summed up to produce a histogram as it is shown in the bottom of Figure 5.1. If a source is present, a significant peak will be visible in the profile (see left side of Figure 5.1). Otherwise, the profile will be flat as shown on the right side of Figure 5.1. After this first investigation, which basically should eliminate the observations with a significant source, 60 observations remained in the sample of blank field candidates.

The *RawX* profiles give just an approximation of the quality of the blank field observation. There is a need for a consistent and impartial selection criterion. Therefore, the CCD was divided into three regions:

- the LowX part (RawX 3-22)
- the MidX part (RawX 23-42)
- the HighX part (RawX 43-62)

Subsequently, spectra were extracted from each previous defined detector part for each observation. The associated response and auxiliary response files were produced following the standard method described in the *XMM-Newton* user handbook. In the call of RMFGEN and ARFGEN the `detmaptype` parameter was set to FLAT to account for the fact that the counts are distributed homogeneously. Especially for ARFGEN the `EXTENDEDSOURCE` parameter was set to YES.

To provide a comparison between the blank field candidates and an ideal blank field observation without any source contamination and a plain illumination, the

²<http://xmm.esac.esa.int/xsa/index.shtml>

³<http://xmm.esac.esa.int/sas/current/doc/epproc/index.html>

⁴<http://xmm.esac.esa.int/sas/current/doc/epfast/index.html>

Table 5.1: Expected count ratios for different detector part combinations based on the corresponding effective areas of the detector parts.

Name	Region	Exp. Ratio
q ₁	LowX/MidX	0.996617
q ₂	HighX/MidX	0.967581
q ₃	LowX/HighX	1.030009

expected count ratios q_i were calculated using the effective areas for different combinations of the detector parts which are shown in Table 5.1. Furthermore, the counts in each detector part were summed up and the count ratios p_1 , p_2 and p_3 were calculated according to the definition of Table 5.1.

In every defined region more than ten counts were measured, so the Poissonian statistic could be used, especially to determine the error. However, additionally the uncertainties of the effective area, other systematic effects of the detector had to be taken into account. Finally, a selection criterion, called Method 1, was defined as:

$$|q_i - p_i| < 5 \times \sigma_{p_i} \quad (5.1)$$

with σ_{p_i} as the Poissonian error of the measured count ratio.

To provide a countercheck, an alternative selection method, Method 2, was defined using the same definitions of the quotients q_1 , q_2 , q_3 and p_1 , p_2 , p_3 . Unlike Method 1, this time a standard deviation was calculated for the entire sample:

$$\sigma^2 = \frac{1}{n} \sum_{obs=1}^n (q_{j,obs} - p_{j,obs})^2 \quad (5.2)$$

The calculation is performed in a loop in which the standard deviation is calculated and all observations with a ratio p_i which is outside a $q_i \pm 1\sigma$ range are marked as not blank. If the standard deviation of the complete sample is below 0.05, the loop breaks and the remaining observations are marked as blank.

In the end, two sets of samples were defined, namely, the strict sample for which the criterion is fulfilled for all three quotients, whereas for the non strict sample the criterion has to be fulfilled only for the quotients q_1 and q_2 .

Method 1 yields a strict sample of ten observations and a non strict sample of 30 observations. On the other hand, Method 2 leads to a strict sample of 16 observations and a non strict sample of also 30 observations.

5.3.2 Sample Characteristics

Thereafter, the sample of blank field candidates have to be characterized and reviewed. In particular for the presence of a source contamination or any other

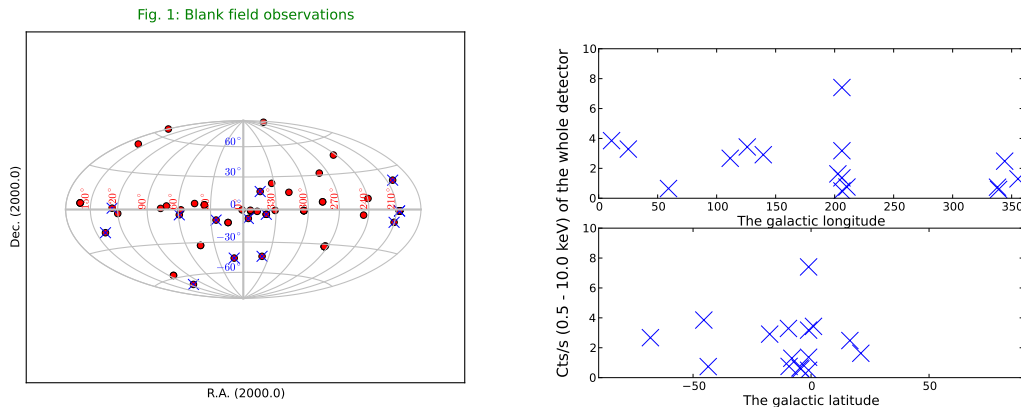


Figure 5.3: *Left panel:* The observations which show no significant source in the *RawX* profile are marked in red. Additionally, the observations of the strict sample are marked with blue crosses. *Right panel:* The count rates of the strict sample observations are plotted against the galactic latitude and longitude.

systematic effect. If not specified, the given results refer to the samples obtained by Method 2, since it provides more observations in the strict sample.

Coordinates

At first, the locations of the observations were plotted in galactic coordinates to check if a clustering of the blank field candidates is present. As it can be seen on the left side of Figure 5.3 in which the non strict sample is plotted in red points and the strict sample observations are marked in blue crosses, no significant clustering of the observations was found. Naturally, there are more observations with low galactic latitude, since the objects of interest which are observed in Timing Mode are in most cases close to the galactic plane. Furthermore, it can be seen on the right side of Figure 5.3 that the count rate differs in a range from below 1 cts/s up to around 8 cts/s which indicates that the blank field candidates cover different background conditions, which is not surprising in view of the sources of background described in Section 5.2.

PI over *RawX*

In a next step a PI⁵ over *RawX* plot was produced for each blank field candidate. This kind of plot illustrates the contribution of a certain energy in each detector column as shown before in Figure 4.3. An example when a source is present is shown on the left side of Figure 5.4. A strong vertical line, which originates from

⁵Pulse Invariant, a characteristic of the energy which is given in units of eV

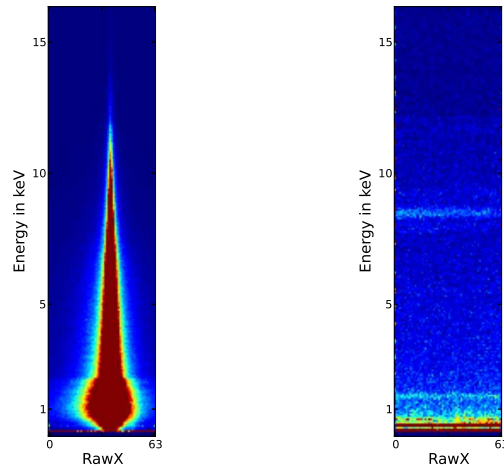


Figure 5.4: *Left panel:* Shown is the PI over *RawX* plot of an observation with a significant source in the central region of the detector. *Right panel:* For comparison, an example is given of a PI over *RawX* plot of an observation in which no source is present. The copper line at about 8 keV can be seen.

the source, is dominating the plot and it is concentrated in the central region of the detector. On the right side of Figure 5.4 the counterexample is shown where no source is present. The counts are distributed homogeneously and several horizontal lines are present which originate from the surrounding detector material and are therefore not depending on the raw X coordinate. The most prominent line feature is located around 8 keV which is the copper line (compare for example with Freyberg et al. 2004). No significant source contamination was found in the observations of the strict sample.

Light curves

Transient sources or bursts could contaminate the blank field temporarily. Therefore, light curves were extracted from the complete energy range. However, the investigation of the light curves gave no evidence for any kind of temporal feature.

Furthermore, light curves above 10 keV were produced to check for the presence of flaring background. Some of them showed presence of a weak flaring particle background, however, the spectrum was not contaminated significantly.

As a last step the light curves were folded with different typical time periods to check for periodic signals which would be a hint for a source. Since no periodicity was found in any source, no blank field candidate was rejected due to the study of the light curves.

MOS Data

An independent way to study the source contamination is provided by the two EPIC-MOS cameras. However, not in all observations the EPIC-MOS cameras were switched on or were operated in a read out mode in which the region of the CCD 4 of the EPIC-PN is accessible.

Following the steps suggested in the SAS thread on the ESA webpage⁶ a source detection was performed using the EDETECT_CHAIN tool which is provided in the SAS analysis package. An example of a significant source contamination can be seen on the left side of the upper panel of Figure 5.5. The MOS 1 was operated in Full Frame mode and several point sources fall in the field of view of the PN CCD 4 which is indicated by the green rectangle. For comparison, an example of an uncontaminated observation is shown on the right side of Figure 5.5. Since source contamination was found in most of the MOS data, an accumulated MOS spectrum was produced for each observation which includes all sources in the field of view of the EPIC-PN CCD 4 to deal with this. Subsequently, simulations of EPIC-PN spectra were performed using XSPEC based on the best-fit models of the achieved MOS spectra. Afterwards, these spectra were subtracted from the corresponding blank field spectra. As can be seen in Figure 5.5 in which a representative example is shown, the blank field spectra are not significantly modified by the contaminating sources. Hence, it can be stated that the blank fields are contaminated to a negligible degree and could be used without any restrictions. Nevertheless, to provide a proper blank field, the contamination-subtracted spectra are used in the following.

5.3.3 Background properties

A study was performed using the blank field sample which was reviewed for any source contamination, to collect all parameters which can be used to obtain a suitable blank field for a given observation. As mentioned before, the background conditions are not constant among different observations, since the telescope is pointing to different regions of the sky and the sun can be in a different state of activity.

The following parameters were chosen to provide an independent measure of the background observations to fit the conditions during a given observation. Therefore, a hard color was defined by integrating the counts in the 4 keV–8 keV range and a soft color by integrating the counts in the 1.5 keV–2.5 keV range. The ratio of these colors can be used to classify the spectral shape.

Galactic coordinates

At first a dependence of that hardness ratio on the position of the observation in the sky was studied. As it can be seen in Figure 5.6, no dependence was found

⁶http://xmm.esac.esa.int/sas/current/documentation/threads/src_find_thread.shtml

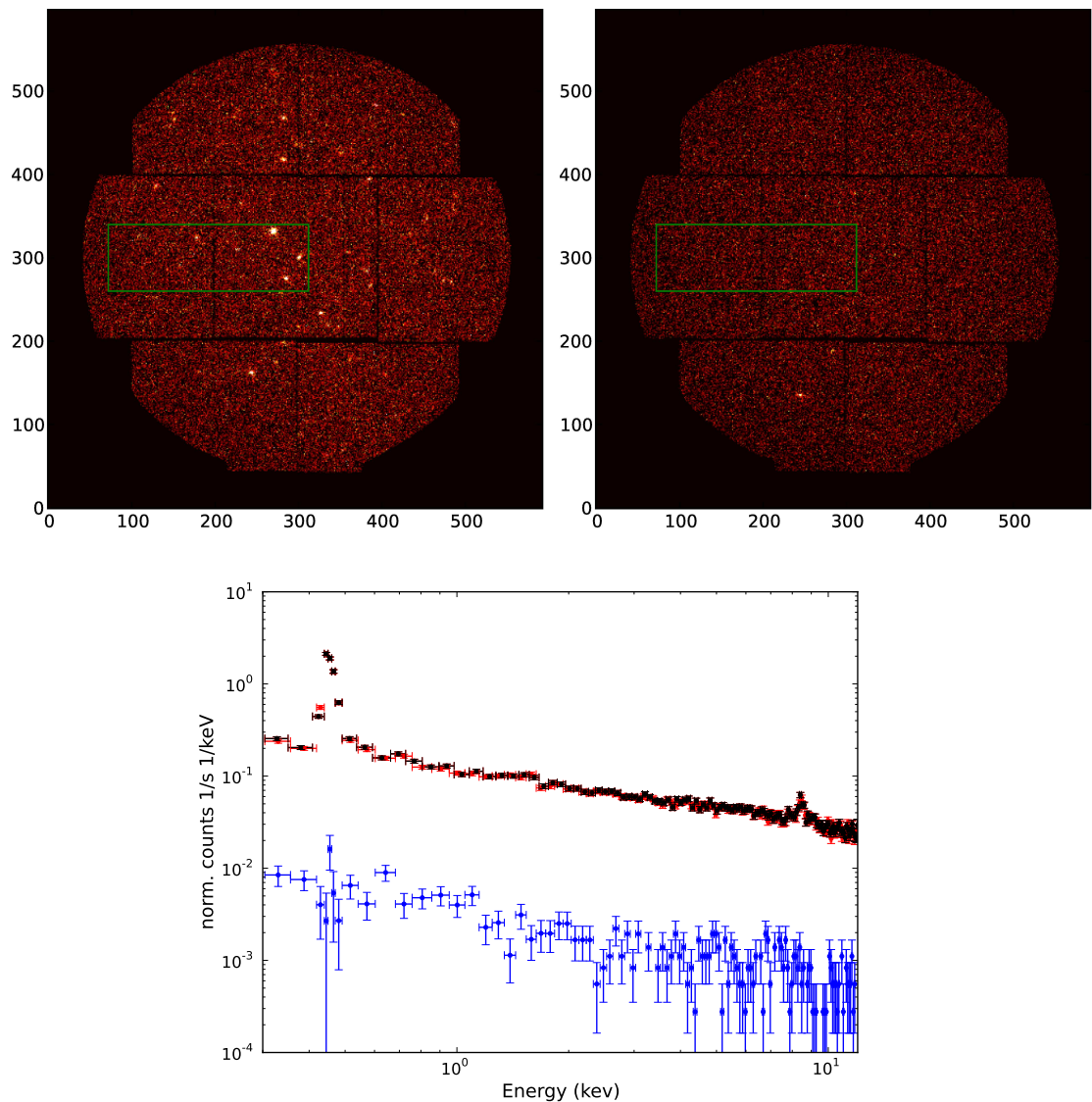


Figure 5.5: *Upper panel:* MOS images with and without source contamination in the field of view of the CCD 4 of the EPIC-PN (green rectangle). *Lower panel:* Spectrum of observation # 0111100301 (black) and the faked (simulated) spectrum (blue) based on the MOS model. Also plotted is the subtracted spectrum (red). The subtracted spectrum is nearly identical with the original spectrum.

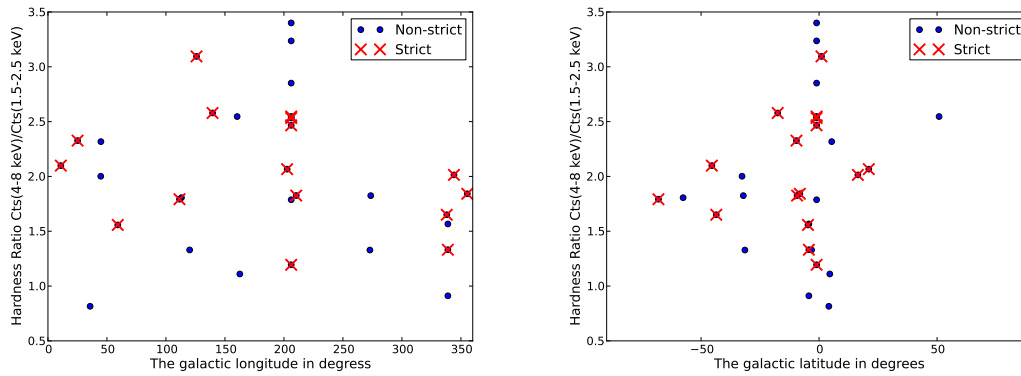


Figure 5.6: *Left panel:* Shown is the hardness ratio (definition see text) over the galactic longitude of the blank field observation. *Right panel:* The hardness ratio is plotted over the galactic latitude. No error bars are shown since they are within the size of the markers.

neither on the galactic longitude nor on the galactic latitude of the blank field observation.

Date of observation

Subsequently, a systematic change of the spectral shape depending on the date of the observation was checked. The plot shown on the left side of Figure 5.7 implies no evidence for a significant change over mission time.

RGS background count rate

Another possibility to classify the background is to use the background count rate of the RGS instrument (Reflection Grating Spectrometer, den Herder et al. 2001) on board of *XMM-Newton*.

The count rate can be obtained from the RGS CCD 9 as described by Rosario Gonzalez-Riestra in the XMM-SOC-CAL-TN-0058⁷ documentation paper.

On the right side of Figure 5.7 it can be seen that the hardness ratio tends to increase with a higher count rate of the RGS background. This assumption is emphasized by the plots shown in Figure 5.8 in which on the left side all spectra of the strict sample are plotted with colors indicating the RGS background count rate. As it can be seen, the overall shape is similar, whereas the strength of the line features are changing. The hardening of the spectra is apparent by summing up spectra which are in the same RGS background count rate ranges shown on the right side of Figure 5.8.

⁷http://xmm2.esac.esa.int/external/xmm_sw_cal/calib/documentation/index.shtml#EPIC

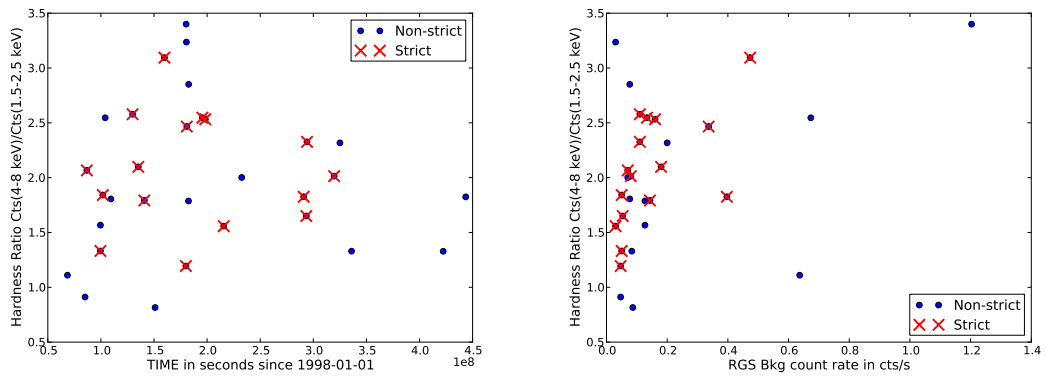


Figure 5.7: *Left panel:* Shown is the hardness ratio over the date of observation of the blank field observation. *Right panel:* The hardness ratio is plotted over the RGS background count rate. No error bars are shown since they are within the size of the markers.

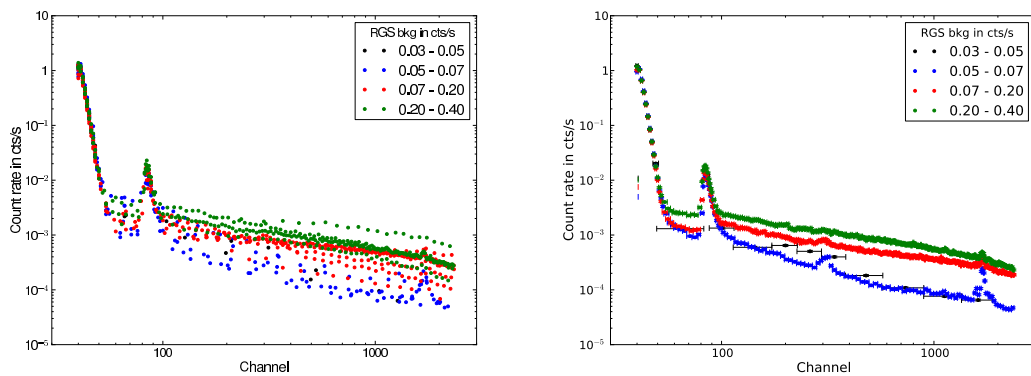


Figure 5.8: *Left panel:* All spectra are plotted depending on different RGS background count rates which are marked in different colors. In some spectra the prominent background features like the Cu K_{α} line around 8.0 keV and the Al K_{α} line around 1.48 keV can be seen. *Right panel:* The summed spectra of the different RGS background count rate levels are shown.

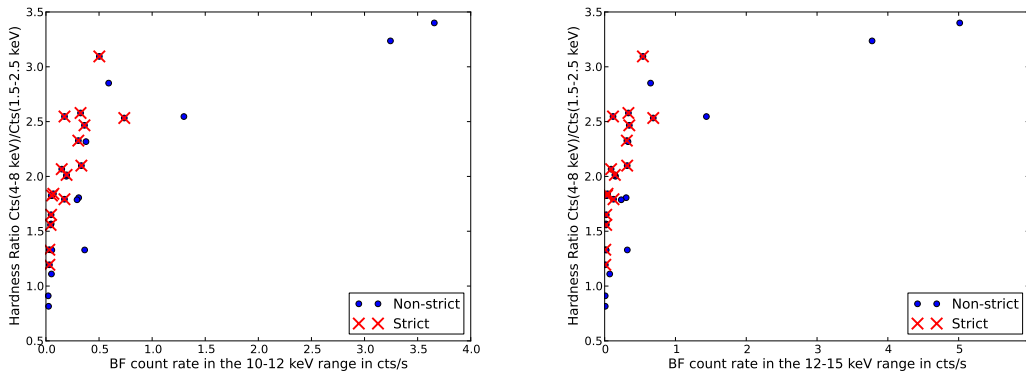


Figure 5.9: *Left panel:* Shown is the hardness ratio over the count rate in the 10 keV–12 keV energy range. *Right panel:* The hardness ratio is plotted over the count rate in the 12 keV–15 keV range.

A possible explanation of this finding is that the RGS background is dominated by soft protons which produces a power-law spectrum as described in Section 5.2.2. The more soft protons are present the harder is the spectrum of the blank field.

Count rate in high energy bands

Finally, the dependence of the hardness ratio on the count rate in the high energy bands of 10 keV–12 keV and 12 keV–15 keV is studied. These energy ranges are a measure of the flux and can be also used to adjust to a given observation, since in most cases the source contribution in the 10 keV–12 keV range is low. However, if there is still a source contamination, as an alternative the 12 keV–15 keV range can be used.

As it can be seen in Figure 5.9, there is a clear dependence of the hardness ratio on the count rates in the high energy bands. Therefore, these parameters can be used to obtain a suitable blank field for a given observation.

Filter

The observed sources could also have a significant contribution in other wavelengths, like infrared or optical, which can produce events on the CCD by loading, which occurs if the optical flux of the source is high and energy is deposited in the pixels by optical photons. To prevent this effect, three different types of filters (*Thin*, *Medium*, *Thick*) can be placed in front of the detector. Indeed, it is essential to know which filter was used to obtain the blank field spectrum to apply a correct background spectrum to the real observation. However, in the non strict samples of both selection methods no observation is included which uses the *Thick*-filter. For testing purposes two *Thick*-filter observations were added to the strict sample

Table 5.2: Observation information of the highly obscured test sample reported in the EPIC-PN Fast Mode Calibration Status Document CAL-TN-0083. The n_{H} is given in 10^{22} cm^{-2} .

Label	OBSID	Source	Filter	n_{H}
T1	0036140201	XB 1323-619	Thin	2.7755
T2	0149550401	SAX J2103.5+4545	Thick	0.60522
T3	0402330501	X 1624-490	Medium	8.84071
T4	0410580401	IGR J17497-2821	Thick	2.80503
T5	0510010101	XTE J1856+053	Medium	3.23401
T6	0554110201	H 1743-322	Thick	1.45771
T7	0555410101	4U 1907+09	Thin	1.88355
T8	0610000701	XTE J1652-453	Thin	4.28975

which both show no significant source contamination in the PI over *RawX* plot.

5.3.4 Normalization of the blank field

After a suitable blank field observation is found, the obtained background spectrum has to be normalized to adapt to the conditions of the observations. Therefore, for both, the source spectrum and the blank field spectrum, the count rate in the high energy ranges, namely 10 keV–12 keV and 12 keV–15 keV, were calculated. Afterwards, the blank field spectrum was multiplied with the ratio of the count ratios. If there was a significant source contribution in the 10 keV–12 keV range, the count rate in the 12 keV–15 keV range had to be used for normalization.

5.4 Testing

A sophisticated background spectrum for Timing Mode observations is essential especially for weak and highly obscured sources. In this thesis work the results were studied when subtracting a background spectrum obtained by blank field observations from the spectra of eight highly obscured sources, which were addressed in the EPIC-PN Fast Mode Calibration Status Document⁸. The studied sources are summarized in Table 5.2. A soft excess was found in the spectral fitting of these sources, which could originate from background contamination.

The goal of the testing is to give a first impression in which way a background spectrum can be obtained from blank field observations and how it can be applied on a given observation. Another sample of weak sources was investigated by Matteo Guainazzi at the ESAC in Madrid.

⁸<http://xmm2.esac.esa.int/docs/documents/CAL-TN-0083.pdf>

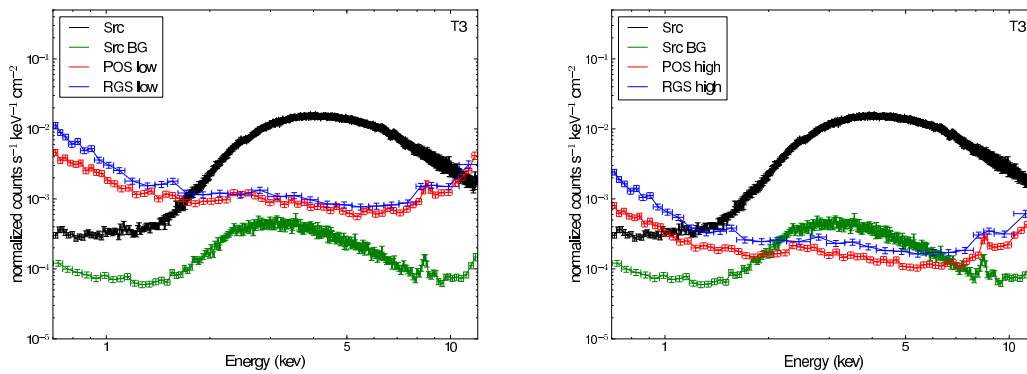


Figure 5.10: *Left side:* Shown are the spectra of test observation T3 in black and the corresponding background extracted from the outer parts of the CCD in green, as well as the spectrum of the closest blank field in position in red and in blue the background spectrum obtained from the blank field with a comparable RGS background count rate. Both blank field spectra are normalized to the 10 keV–12 keV band. *Right side:* The same spectra as before but normalized to the 12 keV–15 keV band.

5.4.1 Single Blank Field

At first, a single blank field was chosen. On the one hand the closest in position in galactic coordinates (POS) to each observation of the test sample was used. On the other hand a blank field observation was selected which was observed during a comparable RGS background count rate as the given observation (RGS).

However, for six observations in the test sample neither a close-by blank field nor a blank field with comparable RGS background count rate with the right filter could be found. The remaining two observations were tested using a blank field within a range of $\pm 15^\circ$ in both the right ascension and the declination of the test object. On the left side of Figure 5.10, the results are shown for test observation T3 when the blank field spectrum is normalized to the 10 keV–12 keV range. The source spectrum, given in black, shows a high absorption below 2 keV. Furthermore, the background spectrum obtained from the border area of the CCD is plotted in green. As it can be seen, the observational background spectrum is contaminated by the source, which manifests itself in an identical general shape of the spectra. The observation background matches the source spectrum at low energies, but if this background is applied also source photons would be subtracted.

It is apparent that the blank field spectra differ significantly from the observational background. The spectral shape follows roughly a power law with an increase above 10 keV whereas also the copper line around 8 keV can be seen. However, both blank field spectra overestimate the background dramatically, which leads to the statement that the source contribution is high in the 10 keV–12 keV range. There-

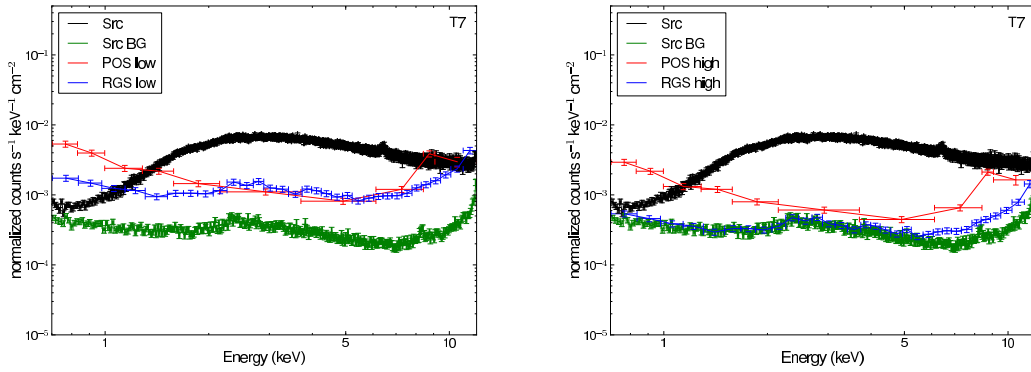


Figure 5.11: *Left side:* Shown are the spectra of test observation T7 in black and the corresponding background extracted from the outer parts of the CCD in green, as well as the spectrum of the closest blank field in position in red and in blue the background spectrum obtained from the blank field with a comparable RGS background count rate. Both blank field spectra are normalized to the 10 keV–12 keV band. *Right side:* The same spectra as before but normalized to the 12 keV–15 keV band.

fore, both blank field spectra were also normalized to the 12 keV–15 keV energy range as shown on the right side of Figure 5.10. The POS and the RGS blank fields are still too high whereas the POS blank field matches almost the source spectrum at low energies.

On the other hand, as shown on the left side of Figure 5.11 for test observation T7, the POS blank field overestimates again the background and exhibits a different spectral shape at low energies compared to the RGS blank field. The RGS blank field shows a similar spectral shape as the observational background, but with a higher intensity for the normalization to the 10 keV–12 keV band. Using the normalization in the 12 keV–15 keV band decreases the intensity and it matches almost perfectly the observational background at low energies. This leads to the assumption that the observational background of T7 shows no source contamination and is therefore usable. However, the POS blank field spectrum shows also an overestimation of the background when normalized to the 12 keV–15 keV band.

In summary, it can be stated that selecting a single blank field to extract a background spectrum promises a more suitable result when using a blank field with a comparable RGS background count rate than a close-by blank field. Nevertheless, the RGS blank field seems to be a proper background spectrum for test observation T7. There is a need for a more generic selection method, as it was not possible to find a suitable blank field for test observation T3.

5.4.2 Merged Blank Field Event List

Subsequently, since the selection of blank field observations on the basis of RGS background count rate and position gave no satisfying results, all blank field observations of the strict sample of Method 2 were merged to a single event file to provide a better statistic and to test another way to obtain a background spectrum. Furthermore, the event file was modified to allow to select the data with respect to the filter type. As before, the count rate CR_{src} of the source spectrum is calculated in the 10 keV–12 keV range. In contrast to the previous selection, the blank field spectra are extracted from parts of the event list in which the count rate of the blank field CR_{bf} is in an interval of:

$$CR_{\text{src}}/2 < CR_{\text{bf}} < 2 \times CR_{\text{src}}. \quad (5.3)$$

Using smaller count rate intervals decreases the number of events and therefore the statistics.

As it can be seen in Figure 5.12, the blank field spectra extracted from the merged event list differ significantly from the observational background spectra which show, except for T7, a source contamination. Furthermore, the blank field spectra for T1 and T7 overestimate the background when normalized to the 10 keV–12 keV band. For these cases the normalization to the 12 keV–15 keV band which is shown on the right side of Figure 5.12, is more suitable. Although the intensity of the blank field spectrum is higher than the observational background in T7, the spectral shape is almost identical, which emphasizes the previous finding that the background is not contaminated by the source.

5.4.3 Time-dependent Merged Blank Field Event List

To improve the extraction of a background spectrum from the merged blank field event list, each observation is divided in intervals of 5000 s and the calculation of the count rate in the 10 keV–12 keV energy band is performed in each interval. The final blank field spectrum is produced by summing up the blank field spectra corresponding to the individual intervals which are weighted with their relative contribution to the background which is given for each interval as:

$$m = C_{10-12,\text{bf}}/C_{10-12,\text{src}} \quad (5.4)$$

with $C_{10-12,\text{bf}}$ as the counts in the 10 keV–12 keV range for the blank field and $C_{10-12,\text{src}}$ as the counts for the source spectrum in the 10 keV–12 keV range, respectively.

However, it has been found that the count rate intervals defined in Equation 5.3 are too small for the time-dependent extraction, since there are time intervals with very low count rates for which no corresponding blank field observation could be found. To provide a generic method for all kind of observations, the count rate intervals are redefined to be:

$$CR_{\text{src}}/3 < CR_{\text{bf}} < 3 \times CR_{\text{src}} \quad (5.5)$$

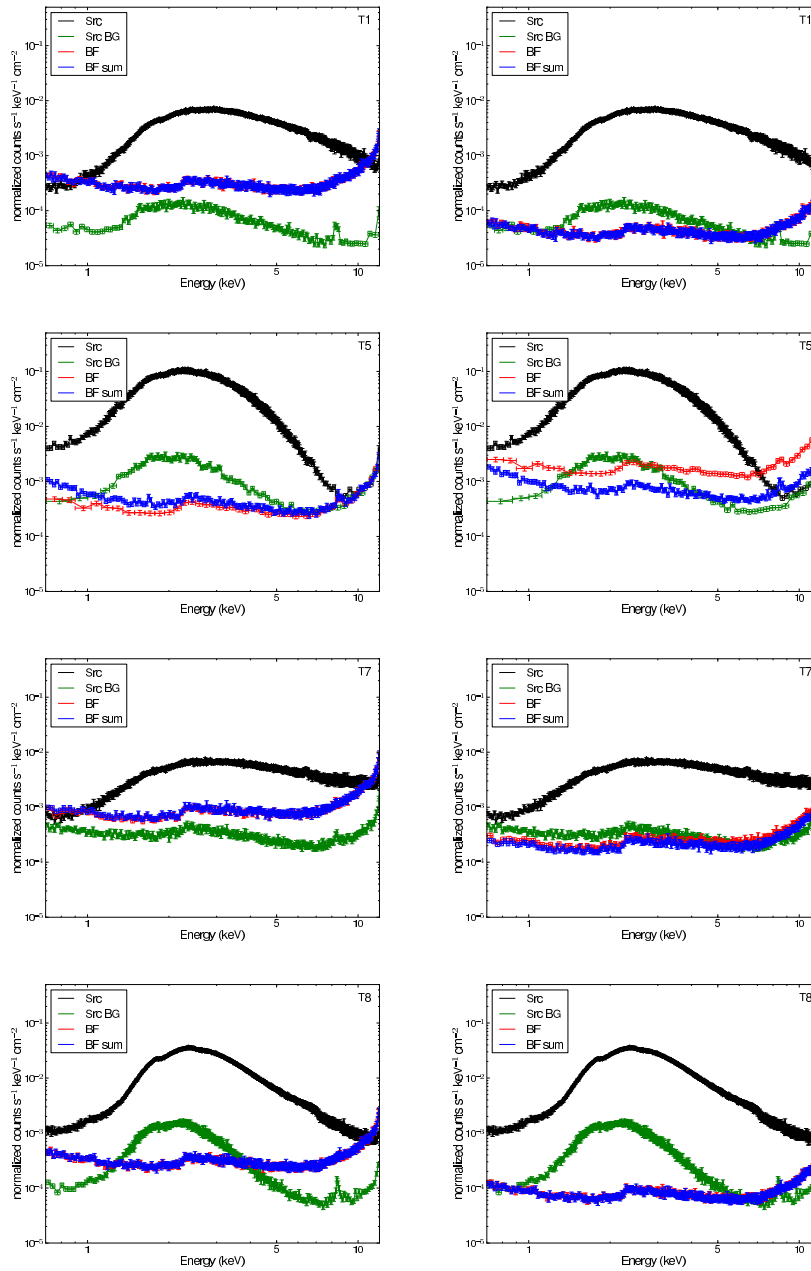


Figure 5.12: Shown are the spectra of the test observations T1, T5, T7 and T8 when the blank field spectra are normalized to the 10 keV–12 keV band (left side) and the 12 keV–15 keV band (right side). The source spectra are given in black, whereas the corresponding observational background spectra are shown in green. Furthermore, the blank field spectra extracted from the merged event list are given in red and the time-dependent blank field spectra are shown in blue.

In Figure 5.12 the resulting blank field spectra are given in blue. As it can be seen, the summed spectra are almost identical to the time-independent blank field spectra with the exception of test observation T5. However, the observation is less than 10 ks and therefore the time-dependent spectra consists of only one blank field spectrum.

As before, also the time-dependent blank field spectra for T1 and T5 overestimate the background which is adjusted by the normalization to the 12 keV–15 keV band.

5.4.4 Apply different background spectra

To study the influence of the different background spectra on the spectral fit of the test observations, the corresponding spectra are characterized by a generic model, namely an absorbed combination of a disk blackbody and a power-law (TBABS(DISKBB + POWERLAW)), whereas the column density is fixed to the value given in the calibration document.

In Figure 5.13 both, the spectra and the residuals are shown when no background spectrum is used as well as when the background extracted from the border area of the CCD is applied. Furthermore, shown are also the results when the single spectrum obtained from the merged blank field list and the time-dependent summed spectra are applied to the source spectrum. The soft excess below 2 keV is prominent, which cannot be reduced by the use of the background extracted from the border area of the CCD for all test objects. Especially for T5 and T7, the time-independent background spectrum extracted from the merged blank field event list reduces the excess significantly when normalized to the 12 keV–15 keV band, however, the excess does not vanish completely.

Furthermore, it can be seen that the time-dependent background extraction does not improve the fit compared to the time-independent one.

5.5 Conclusions and Outlook

In this Chapter it was shown that there is a need for an observation independent preparation of a background spectrum for observations performed in Timing Mode of the EPIC-PN. Since only CCD 4 is working in this mode, the PSF fills the complete detector and therefore no source-free region can be defined. As an alternative method the use of existing blank field observations was introduced.

However, several studies had to be performed before a blank field could confirmed to be without any source contribution. Therefore, two methods were used to select the blank fields from the candidate sample which resulted in a sample of 16 observations. Different characteristics of this sample were presented which gave no evidence for a significant source contamination. Consequently, this sample of blank fields was found to be suitable for obtaining a background spectrum.

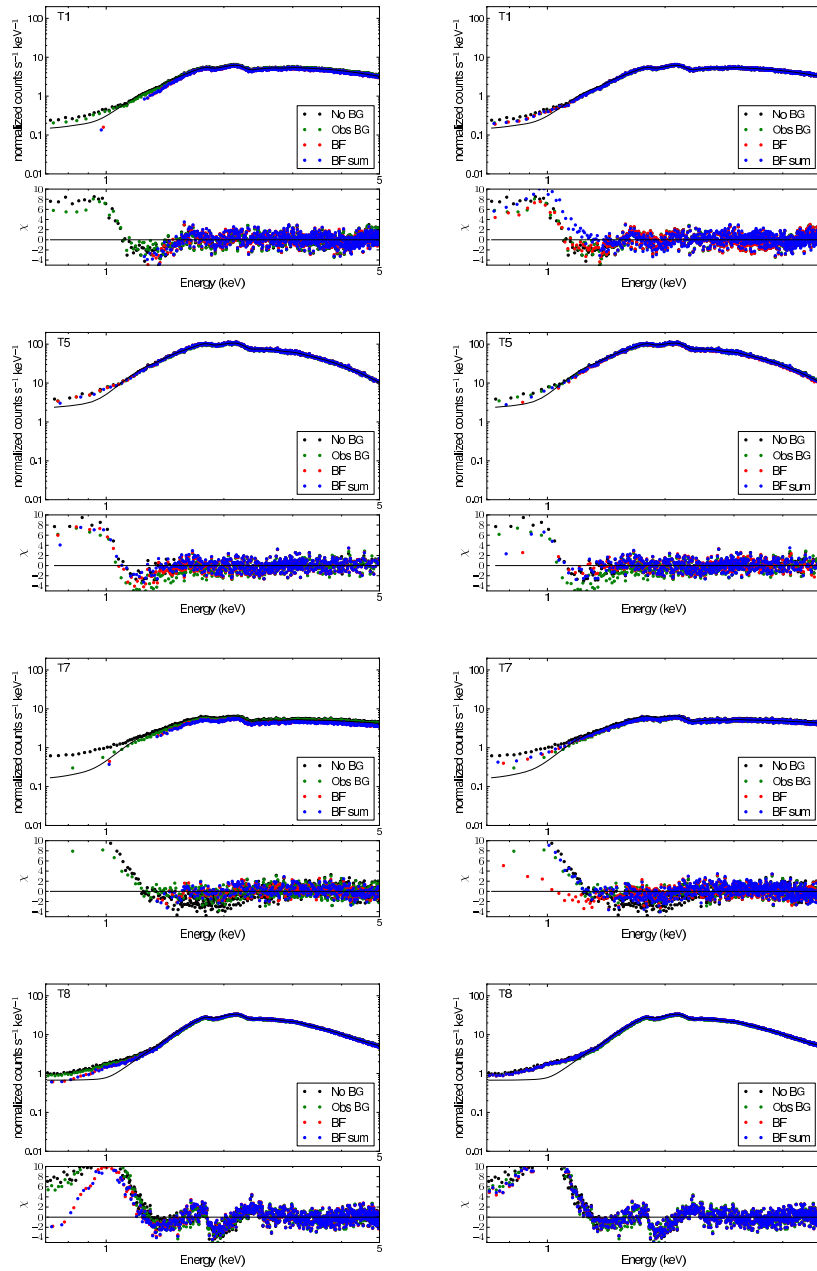


Figure 5.13: Fit results for test observations T1, T5, T7 and T8. The spectra are modeled by an absorbed combination of a disk blackbody and a power-law (TBABS(DISKBB + POWERLAW)). The original spectra are given in black and those with the background extracted from the border of the CCD are shown in green. Furthermore, the blank field spectra extracted from the merged event list are given in red and the time-dependent blank field spectra are shown in blue. The BFs are normalized to the 10 keV–12 keV band (left side) and to the 12 keV–15 keV band (right side).

Furthermore, different possibilities were presented to extract an adequate background spectrum from the blank field sample. To take into account the conditions of the observation, the blank field spectra were normalized to the count rate of the source spectrum in the 10 keV–12 keV range and alternatively in the 12 keV–15 keV range. It was shown that it is not possible to find a suitable background spectrum by neither selecting the closest blank field observation nor by using a blank field with comparable RGS background count rate. Due to that all blank field observations were merged to a single event list and a background spectrum is extracted from parts of it which show a count rate that lies in a defined region around the count rate of the source in the 10 keV–12 keV range.

It was attempted to refine this technique by sub-dividing the background light curve in time intervals for which individual background spectra were extracted which were finally summed up. However, the used length of the time intervals and the used normalization provided no improvement compared to the time-independent background extraction.

Since the goal of this work was to provide a possibility to extract a background spectrum from blank field observations, further study to define a proper normalization method was taken over by the SOC at the ESAC in Madrid. Potential improvements are the redefining of the length of the time-intervals to smaller values and the restriction of the count rate intervals from which the spectrum is extracted from. However, this requires a larger sample of blank fields that cover a variety of different background conditions and therefore different count rates. A dedicated observation campaign with the intention to produce blank fields would be a profitable task.

The final goal is to implement a script in the analysis software SAS which can be used to extract a background spectrum that is suitable for the given observation.

CHAPTER 6

SUMMARY AND OUTLOOK

6.1 Summary and Conclusions

The focus of this thesis was set on three problems related to the analysis of low-mass X-ray binary systems and observations performed in Timing Mode of the EPIC-PN camera aboard *XMM-Newton*.

Firstly, the nature of the spectrum and especially of the fluorescence iron K_{α} line was discussed for the source 4U 1735–44. Observations performed by the X-ray satellites *BeppoSAX* and *XMM-Newton* were analysed. The analysis revealed that the spectrum can be modeled using an absorbed combination of a disk blackbody and a Comptonization model, in the case of *BeppoSAX*, or a single blackbody, for the *XMM-Newton* data. The line feature could be modeled either with a reflection model or equally well with a GAUSSIAN or a relativistic DISKLINE model. The inner radius of the DISKLINE model was determined to be more than 15 Schwarzschild radii which led to the conclusion that the line is not produced close to the neutron star. Taking pile-up into account, showed that the parameters of the line did not change significantly. As a possible geometry, a plasma region of low-energy electrons close to the neutron star around the accretion disk was proposed. This Comptonization region is fed by the accretion disk itself as well as from the equatorial plane of the neutron star. This model can be seen as a combination of the competitive Western and the Eastern models.

In the second part, simulations were performed to study in detail the effect of pile-up on observations carried out in the Timing Mode of the EPIC-PN camera aboard *XMM-Newton*. This study was driven by the results of the analysis and work of Ng et al. (2010), who stated that the relativistic line profiles are caused by pile-up effects. As input for the simulations, generic models, made of a continuum and lines with different widths, were initially used. For the simulations with the generic models it was shown that pile-up effects do indeed have an influence on the spectral shape, which is manifested as the expected hardening of the spectrum. Furthermore, the simulations revealed that no pile-up effects are present for a

pile-up fraction below 3%. However, no distortion of the line profile could be found in any of the studied simulation setups. On the contrary, it was shown that the exclusion of central columns from the extraction region to reduce pile-up, resulted in worse statistics and therefore a line with a relativistic origin can be also modeled by a Gaussian. Moreover, simulations were performed based on published analysis results of the low-mass X-ray binaries Serpens X-1 (Cackett et al. 2010), 4U 1705–44 (di Salvo et al. 2009) and 4U 1636–36 (Pandel et al. 2008), who stated a relativistic origin of the line. These observations were also analysed by Ng et al. (2010) and therefore a comparison was made. The findings of these simulations emphasized the results of the generic simulations. The relativistic origin of the line was reproduced even when the absence of pile-up was assured. However, when columns were excluded, a Gaussian line profile was also able to fit the data. Finally, the simulations were performed the other way round with a Gaussian line as input, according to the results given by Ng et al. (2010). The study gave no evidence that the Gaussian line can be distorted by pile-up effects to a line which seems to have a relativistic origin. Therefore, it can be stated that the results on relativistic lines are solid, since the width and the shape of the line are not strongly influenced by pile-up.

The last part of the thesis dealt with the problem of background extraction for observations performed in Timing Mode of the EPIC-PN aboard *XMM-Newton*. A possible solution for a suitable background was presented in this thesis. All observations performed in Timing Mode were scanned to provide a sample of blank field observations. This sample were reviewed to assure the absence of any source contamination and the resulting observations were merged to a single event file. First tests showed that the most promising method to get a proper background spectrum is to extract the background from parts of the merged event list with a comparable count rate as the observation in a high energy range. This method was refined to a time-dependent extraction in which the observation is divided into time intervals of 5000 seconds to take into account the time variability of the background.

Altogether, it was shown that there are different aspects which have to be taken into account in a meaningful analysis of low-mass X-ray binaries and X-ray observations in general. Instrumental effects, as well as the physics of the observed sources, have to be understood and investigated in detail to draw conclusions on the astrophysical nature of the source.

6.2 Outlook

In this thesis it was shown, that pile-up will always be a challenge for detectors based on CCDs. The development of faster read-out technologies and detailed studies of the effects caused by pile-up can help to decrease the influence of pile-up. Simulations always offer an independent way to understand and check for these effects. However, forthcoming missions, for example a *LOFT*-like mission, which

is not based on CCDs, would have the capacity to give an answer to the question about the nature of low-mass X-ray binaries. A clear determination will be made between Gaussian line features and those with a relativistic origin.

The testing of the merged blank field event list will be concluded at the ESAC in Madrid. In the next version of the SAS analysis package a thread including a script will be published to offer the user community a possibility to extract a suitable background spectrum to their observation.

BIBLIOGRAPHY

- Anders, E. & Grevesse, N. 1989, *Geochim. Cosmochim. Acta*, 53, 197
- Arnaud, K. A. 1996, in *Astronomical Society of the Pacific Conference Series*, Vol. 101, *Astronomical Data Analysis Software and Systems V*, ed. G. H. Barnes & J. Jacoby, 17
- Arnaud K.A., George I.M., T. A. 2009, OGIP Memo OGIP/92-007
- Aschenbach, B. 1985, *Reports on Progress in Physics*, 48, 579
- Balucinska-Church, M. & McCammon, D. 1992, *ApJ*, 400, 699
- Barr, P., White, N. E., & Page, C. G. 1985, *MNRAS*, 216, 65
- Barret, D., den Herder, J. W., Piro, L., et al. 2013, *ArXiv e-prints*, 1308.6784
- Boella, G., Butler, R. C., Perola, G. C., et al. 1997a, *A&AS*, 122, 299
- Boella, G., Chiappetti, L., Conti, G., et al. 1997b, *A&AS*, 122, 327
- Bozzo, E., Stella, L., van der Klis, M., et al. 2014, in *European Physical Journal Web of Conferences*, Vol. 64, *European Physical Journal Web of Conferences*, 9002
- Cackett, E. M., Miller, J. M., Ballantyne, D. R., et al. 2010, *ApJ*, 720, 205
- Cackett, E. M., Miller, J. M., Homan, J., et al. 2009, *ApJ*, 690, 1847
- Cackett, E. M., Miller, J. M., Reis, R., Fabian, A. C., & Barret, D. 2012, in *American Institute of Physics Conference Series*, Vol. 1427, *American Institute of Physics Conference Series*, ed. R. Petre, K. Mitsuda, & L. Angelini, 304–305
- Carter, J. A. & Sembay, S. 2008, *A&A*, 489, 837
- Carter, J. A., Sembay, S., & Read, A. M. 2011, *A&A*, 527,
- Casares, J., Cornelisse, R., Steeghs, D., et al. 2006, *MNRAS*, 373, 1235

- Church, M. J. & Balucinska-Church, M. 1995, *A&A*, 300, 441
- Church, M. J. & Balucinska-Church, M. 2004, *MNRAS*, 348, 955
- Conti, G., Mattaini, E., Santambrogio, E., et al. 1994, in Presented at the Society of Photo-Optical Instrumentation Engineers (SPIE) Conference, Vol. 2279, Society of Photo-Optical Instrumentation Engineers (SPIE) Conference Series, ed. R. B. Hoover & A. B. Walker, 101–109
- Corbet, R. H. D., Thorstensen, J. R., Charles, P. A., et al. 1986, *MNRAS*, 222, 15
- D’Ài, A., di Salvo, T., Ballantyne, D., et al. 2010, *A&A*, 516, L36
- den Herder, J. W., Brinkman, A. C., Kahn, S. M., et al. 2001, *A&A*, 365,
- Dennerl, K., Briel, U. G., Haberl, F., et al. 1999, in Presented at the Society of Photo-Optical Instrumentation Engineers (SPIE) Conference, Vol. 3765, Society of Photo-Optical Instrumentation Engineers (SPIE) Conference Series, ed. O. H. Siegmund & K. A. Flanagan, 232–243
- di Salvo, T., D’Ài, A., Iaria, R., et al. 2009, *MNRAS*, 398, 2022
- Di Salvo, T. & Stella, L. 2002, arXiv:astro-ph/0207219
- Elsner, R. F., Weisskopf, M. C., Darbro, W., et al. 1986, *ApJ*, 308, 655
- Fabbiano, G., Kim, D. W., & Trinchieri, G. 1992, *ApJS*, 80, 531
- Fabian, A. C. 2008, *Astronomische Nachrichten*, 329, 155
- Fabian, A. C., Iwasawa, K., Reynolds, C. S., & Young, A. J. 2000, *PASP*, 112, 1145
- Fabian, A. C., Rees, M. J., Stella, L., & White, N. E. 1989, *MNRAS*, 238, 729
- Ferreira, D. D. M., Jakobsen, A. C., Christensen, F. E., et al. 2012, in Society of Photo-Optical Instrumentation Engineers (SPIE) Conference Series, Vol. 8443, Society of Photo-Optical Instrumentation Engineers (SPIE) Conference Series
- Ford, E., Van DER Klis, M., van Paradijs, J., et al. 1998, *Astrophysical Journal*, 508, L155
- Forman, W., Jones, C., Cominsky, L., et al. 1978, *ApJS*, 38, 357
- Freyberg, M. J., Briel, U. G., Dennerl, K., et al. 2004, in Presented at the Society of Photo-Optical Instrumentation Engineers (SPIE) Conference, Vol. 5165, Society of Photo-Optical Instrumentation Engineers (SPIE) Conference Series, ed. K. A. Flanagan & O. H. W. Siegmund, 112–122
- Frontera, F., Costa, E., Dal Fiume, D., et al. 1995, in International Cosmic Ray Conference, Vol. 2, International Cosmic Ray Conference, 41

- Galloway, D., Muno, M., Hartman, J., Psaltis, D., & Chakrabarty, D. 2008, *Astrophysical Journal Supplement Series*, 179, 360
- Giacconi, R., Branduardi, G., Briel, U., et al. 1979, *ApJ*, 230, 540
- Giacconi, R., Gursky, H., Paolini, F. R., & Rossi, B. B. 1962, *Physical Review Letters*, 9, 439
- Giacconi, R., Gursky, H., & van Speybroeck, L. P. 1968, *ARA&A*, 6, 373
- Giacconi, R., Gursky, H., & Waters, J. R. 1964, *Nature*, 204, 981
- Giacconi, R., Reidy, W. P., Vaiana, G. S., van Speybroeck, L. P., & Zehnpfennig, T. F. 1969, *Space Sci. Rev.*, 9, 3
- Giarrusso, S., Santangelo, A. E., Fazio, G., et al. 1995, in Presented at the Society of Photo-Optical Instrumentation Engineers (SPIE) Conference, Vol. 2517, Society of Photo-Optical Instrumentation Engineers (SPIE) Conference Series, ed. S. Fineschi, 234–248
- Gondoin, P., Aschenbach, B. R., Beijersbergen, M. W., et al. 1998a, in Presented at the Society of Photo-Optical Instrumentation Engineers (SPIE) Conference, Vol. 3444, Society of Photo-Optical Instrumentation Engineers (SPIE) Conference Series, ed. R. B. Hoover & A. B. Walker, 278–289
- Gondoin, P., Aschenbach, B. R., Beijersbergen, M. W., et al. 1998b, in Presented at the Society of Photo-Optical Instrumentation Engineers (SPIE) Conference, Vol. 3444, Society of Photo-Optical Instrumentation Engineers (SPIE) Conference Series, ed. R. B. Hoover & A. B. Walker, 290–301
- Gould, H., Tobochnik, J., & Christian, W. 2006, *An introduction to computer simulation methods: Applications to Physical Systems* (third edition) (San Francisco: Addison-Wesley)
- Hasinger, G. & van der Klis, M. 1989, *A&A*, 225, 79
- Hurkett, C. P., Vaughan, S., Osborne, J. P., et al. 2008, *ApJ*, 679, 587
- Jager, R., Heise, J., in 't Zand, J. J. M., & Brinkman, A. C. 1993, *Advances in Space Research*, 13, 315
- Jagoda, N., Austin, G., Mickiewicz, S., & Goddard, R. 1972, *IEEE Transactions on Nuclear Science*, 19, 579
- Jahoda, K., Swank, J. H., Giles, A. B., et al. 1996, in Presented at the Society of Photo-Optical Instrumentation Engineers (SPIE) Conference, Vol. 2808, Society of Photo-Optical Instrumentation Engineers (SPIE) Conference Series, ed. O. H. Siegmund & M. A. Gummin, 59–70
- Jansen, F., Lumb, D., Altieri, B., et al. 2001, *A&A*, 365,

- Jonker, P. G., Wijnands, R., van der Klis, M., et al. 1998, *ApJ*, 499, L191
- Kimmel, N., Hiraga, J. S., Hartmann, R., Meidinger, N., & Strüder, L. 2006, *Nuclear Instruments and Methods in Physics Research Section A: Accelerators, Spectrometers, Detectors and Associated Equipment*, 568, 128
- Knoll, G. F. 2000, *Radiation detection and measurement*, 3rd edn. (New York, NY: Wiley)
- Knoll, G. F. 2010, *Radiation Detection and Measurement* (John Wiley & Sons)
- Kubota, A., Tanaka, Y., Makishima, K., et al. 1998, *PASJ*, 50, 667
- Kuster, M., Benloch, S., Kendziorra, E., & Briel, U. G. 1999, in *Presented at the Society of Photo-Optical Instrumentation Engineers (SPIE) Conference*, Vol. 3765, *Society of Photo-Optical Instrumentation Engineers (SPIE) Conference Series*, ed. O. H. Siegmund & K. A. Flanagan, 673–682
- Lattimer, J. M. & Prakash, M. 2007, *Phys. Rep.*, 442, 109
- Levine, A. M., Bradt, H., Cui, W., et al. 1996, *ApJ*, 469, L33
- Lewin, W. H. G. & van der Klis, M. B., eds. 2006, *Compact stellar X-ray sources*, *Cambridge astrophysics series ; 39* (Cambridge: Cambridge University Press)
- Lightman, A. P. & White, T. R. 1988, *ApJ*, 335, 57
- Longair, M. S. 2011, *High energy astrophysics*, 3rd edn. (Cambridge UK: Cambridge Univ. Press)
- Lumb, D. H., Warwick, R. S., Page, M., & De Luca, A. 2002, *A&A*, 389, 93
- Makino, F. 1987, *Astrophys. Lett.*, 25, 223
- Makishima, K., Maejima, Y., Mitsuda, K., et al. 1986, *ApJ*, 308, 635
- Manzo, G., Giarrusso, S., Santangelo, A., et al. 1997, *A&AS*, 122, 341
- Matsuoka, M. & Asai, K. 2013, *PASJ*, 65, 26
- Méndez, M., van der Klis, M., Ford, E. C., Wijnands, R., & van Paradijs, J. 1999, *ApJ*, 511,
- Miller, J. M., D’Ai, A., Bautz, M. W., et al. 2010, *ApJ*, 724, 1441
- Miller, M. C., Lamb, F. K., & Psaltis, D. 1998, *ApJ*, 508, 791
- Mitsuda, K., Bautz, M., Inoue, H., et al. 2007, *PASJ*, 59, 1
- Mitsuda, K., Inoue, H., Koyama, K., et al. 1984, *PASJ*, 36, 741
- Mitsuda, K., Inoue, H., Nakamura, N., & Tanaka, Y. 1989, *PASJ*, 41, 97

- Morrison, R. & McCammon, D. 1983, *ApJ*, 270, 119
- Mück, B. 2009, Diploma thesis, Eberhard Karls Universität Tübingen
- Mück, B., Piraino, S., & Santangelo, A. 2013, *A&A*, 555, 17
- Nandra, K., Barret, D., Barcons, X., et al. 2013, *ArXiv e-prints*, 1306.2307
- Ng, C., Díaz Trigo, M., Cadolle Bel, M., & Migliari, S. 2010, *A&A*, 522, L96
- Pandel, D., Kaaret, P., & Corbel, S. 2008, *ApJ*, 688, 1288
- Parmar, A. N., Martin, D. D. E., Bavdaz, M., et al. 1997, *A&AS*, 122, 309
- Peacock, A., Andresen, R. D., Manzo, G., et al. 1981, *Space Sci. Rev.*, 30, 525
- Piraino, S., Santangelo, A., Kaaret, P., et al. 2012, *A&A*, 542, 27
- Predehl, P., Böhringer, H., Brunner, H., et al. 2010, *X-ray Astronomy 2009; Present Status, Multi-Wavelength Approach and Future Perspectives*, 1248, 543
- Rau, A., Meidinger, N., Nandra, K., et al. 2013, *ArXiv e-prints*, 1308.6785
- Ross, R. R. & Fabian, A. C. 2005, *MNRAS*, 358, 211
- Sakurai, S., Yamada, S., Torii, S., et al. 2012, *PASJ*, 64, 72
- Santangelo, A. & Madonia, R. 2014, *Astroparticle Physics*, 53, 130
- Schmid, C., Martin, M., Wilms, J., et al. 2010, *X-ray Astronomy 2009; Present Status, Multi-Wavelength Approach and Future Perspectives*, 1248, 591
- Seon, K., Min, K., Yoshida, K., et al. 1997, *Astrophysical Journal*, 479, 398
- Seward, F. D. & Charles, P. A. 1995, *Exploring the X-Ray Universe*: Cambridge University Press
- Shimura, T. & Takahara, F. 1995, *ApJ*, 445, 780
- Snowden, S. L., Collier, M. R., & Kuntz, K. D. 2004, *ApJ*, 610, 1182
- Strüder, L., Briel, U., Dennerl, K., et al. 2001, *A&A*, 365, L18
- Tanaka, Y., Inoue, H., & Holt, S. S. 1994, *PASJ*, 46, 37
- Tanaka, Y., Nandra, K., Fabian, A. C., et al. 1995, *Nature*, 375, 659
- Torrejón, J. M., Schulz, N. S., Nowak, M. A., & Kallman, T. R. 2010, *ApJ*, 715, 947
- Truemper, J. 1982, *Advances in Space Research*, 2, 241
- Turner, M. J. L., Abbey, A., Arnaud, M., et al. 2001, *A&A*, 365, L27

- van der Klis, M. 2006, Rapid X-ray Variability in Compact stellar X-ray sources, ed. M. Lewin, W. H. G. & van der Klis, 39–112
- van der Klis, M., Swank, J. H., Zhang, W., et al. 1996, *ApJ*, 469,
- van Paradijs, J., Penninx, W., Lewin, W. H. G., Sztajno, M., & Truemper, J. 1988, *A&A*, 192, 147
- Weisskopf, M. C., Brinkman, B., Canizares, C., et al. 2002, *PASP*, 114, 1
- White, N. E. & Peacock, A. 1988, *Mem. Soc. Astron. Italiana*, 59, 7
- White, N. E., Peacock, A., Hasinger, G., et al. 1986, *MNRAS*, 218, 129
- White, T. R., Lightman, A. P., & Zdziarski, A. A. 1988, in *American Institute of Physics Conference Series*, Vol. 170, Nuclear Spectroscopy of Astrophysical Sources, ed. N. Gehrels & G. H. Share, 345–349
- Wijnands, R., van der Klis, M., Mendez, M., et al. 1998, *ApJ*, 495, L39
- Wijnands, R. A. D., van der Klis, M., van Paradijs, J., et al. 1996, *IAU Circ.*, 6447, 1
- Yan, M., Sadeghpour, H. R., & Dalgarno, A. 1998, *ApJ*, 496, 1044
- Zdziarski, A. A., Johnson, W. N., & Magdziarz, P. 1996, *MNRAS*, 283, 193
- Zycki, P. T., Done, C., & Smith, D. A. 1999, *MNRAS*, 309, 561

ACKNOWLEDGEMENTS

An dieser Stelle möchte ich mich bei allen bedanken, die zum Gelingen dieser Arbeit beigetragen haben.

Vielen Dank an

Prof. Dr. Andrea Santangelo für die Vergabe des Themas, die Betreuung dieser Arbeit und die Unterstützung in den letzten 7 Jahren am Institut.

Dr. Chris Tenzer für die Unterstützung bei den "Hardware"-bezogenen Themen sowie für die angenehmen Dienstreisen.

Dr. Santina Piraino für die Tipps und Hilfen bei der Datenanalyse.

Marc Pfeifer, Sebastian Diebold für die Tennisspiele und vieles mehr.

Thorsten Nagel, Stephan Hartmann als Ansprechpartner für jede Art von L^AT_EX-Fragen und als jahrelange Mitstreiter des Kinder-Uni Forschertages.

Patrick Kavanagh für die Verbesserung meines Englischs und für eine angenehme Büroatmosphäre.

Christian Schmid für die Kooperation und Hilfe bei den Simulationen.

Matteo Guainazzi für die gute Zusammenarbeit.

"die alte Garde" mit Michi, Jens und Davide.

die **Espressorunde** die immer ein angenehmer Ort für eine Ablenkung war.

meine Mutter, die mich das ganze Studium lang unterstützt hat.

meinen Vater, der mich ebenfalls das ganze Studium lang unterstützt hat und dem es leider nicht vergönnt war, das Ende meines Studiums mitzuerleben.

meine Frau Judith, die sehr viel Geduld mit mir und meiner Arbeit hatte und ohne die ich es nie soweit gebracht hätte.

CURRICULUM VITAE

- 27.05.1983 geboren in Tübingen
- 09.1990 – 07.1994 Grundschule Dusslingen
- 09.1994 – 06.2003 Karl-von-Frisch Gymnasium, Dusslingen
- 06.2003 Abitur
- 10.2003 – 06.2009 Eberhard Karls Universität Tübingen
Studiengang: Diplom Physik
- 04.2007 – 06.2009 Studentische Hilfskraft,
Institut für Astronomie und Astrophysik (IAAT),
Eberhard Karls Universität Tübingen
- 03.2008 – 06.2009 Diplomarbeit unter Anleitung
von Herrn Prof. Dr. A. Santangelo:
'Compact objects with neutron stars observed with Simbol-X'
- 06.2009 Diplom
- 09.2009 – 12.2009 Wissenschaftliche Hilfskraft, IAAT
- 01.2010 – 07.2014 Wissenschaftlicher Mitarbeiter, IAAT
- 09.2009 – 06.2014 Anfertigung der Dissertation mit dem Titel
"Low-mass X-ray binary studies with XMM-Newton"
an der Eberhard Karls Universität Tübingen,
IAAT, Abteilung Hochenergie-Astrophysik
unter der Anleitung von Herrn Prof. Dr. A. Santangelo

Meine wichtigsten akademischen Lehrer waren die folgenden Professoren und Dozenten:

Astronomie und Astrophysik: W. Kley, T. Nagel, J. Peitz, A. Santangelo, K. Werner

Chemie: J. Strähle

Experimentalphysik: H. Clement, J. Jochum, R. Kleiner, D. Wharam

Mathematik: W. Knapp, F. Loose, M. Wolff

Theoretische Physik: A. Fässler, T. Gutsche, M. Liu, H. Müther, N. Schopohl

